

NASA Contractor Report 3573

NASA
CR
3573
c.1

TECH LIBRARY KAFB, NM
0062167

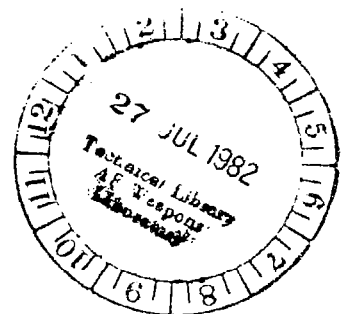
Calculation of Three-Dimensional, Inviscid Supersonic, Steady Flows

Gino Moretti

THIS COPY RETURN TO
AFSC TECHNICAL LIBRARY
HOLLAND AFB, TEXAS

GRANT NSG-1248
JUNE 1982

NASA





NASA Contractor Report 3573

Calculation of Three-Dimensional, Inviscid Supersonic, Steady Flows

Gino Moretti

*Polytechnic Institute of New York
Farmingdale, New York*

Prepared for
Langley Research Center
under Grant NSG-1248



National Aeronautics
and Space Administration

**Scientific and Technical
Information Office**

1982

CONTENTS

	<u>Page</u>
1. Introduction	1
2. Frames of reference	2
3. Derivatives related to the mappings	4
4. Important unit vectors	6
5. Equations of motion	9
6. The integration method	14
7. Characteristic equation for body and shock points	17
8. Treatment of body points	19
9. Treatment of bow shock points	21
10. General outline of one integration step	25
11. Coordinate normalization and grid stretching	27
12. Explicit computation of terms related to mappings	28
13. Initial conditions	33
14. Pointed circular cone	35
15. Attached shock around a hollow intake	38
16. Preliminary tests. Circular cones at no incidence	43
17. Circular cones at an angle of attack	45
18. Elliptic cones	49
19. Cambered wings	69
20. Butler's wing	78
21. A simple fuselage-arrow-wing combination	86
22. Mapping for the arrow-wing airplane	91
23. Additional formulas used beyond t_1	94
24. Some results on fuselage-arrow-wing combinations	96
25. References	117

1. Introduction

The first part of the present Report supersedes Ref. 1; the second part contains a number of calculations and the discussion of their results.

In 1976, when the second part of the work reported in [1] was ready to be published, I decided to reconsider the numerical technique exposed in [1] in order to simplify it and to increase its accuracy. The search was successful, thanks to the good work of de Neef on the methods to compute shock and body points, and of Zannetti on the integration scheme for interior points. The great advantage of de Neef's way of computing shock and body points over the method outlined in [1] stems from his recasting of the characteristic equations in such a way that second derivatives are no longer necessary. In the present category of problems, where the evaluation of second derivatives implies an elaborate manipulation of terms connected with complicated conformal mappings, their elimination provides a substantial saving in coding complexity and running time. On the other hand, the integration scheme which took form as a result of my discussions with Zannetti is, to this date, the closest of all available schemes to the physics of the flow and it has second order accuracy; it is, therefore, best suited to handle complicated flows with formation of imbedded shocks, and entropy layers, in this way allowing the number of grid points to be kept at a minimum. Details on the shock-and-body points method can be found in [2]; details on the integration scheme (which I call the λ - scheme) are given in [3].

In order to avoid confusion, I prefer to expose the analysis in its entirety, rather than referring to [1] and indicating what has to be changed or eliminated. Therefore, parts of the first few Sections of this paper are similar, but not identical, to corresponding parts of [1], which should be considered obsolete.

As stated in the Introduction to [1], we will provide a detailed description of a computational program for the evaluation of three-dimensional, supersonic, inviscid, steady flow past

Introduction

airplanes. No imbedded shocks are considered here explicitly. The emphasis is put instead on how a powerful, automatic mapping technique is coupled to the fluid mechanical analysis in order to assure a high degree of accuracy without increasing the number of computational nodes beyond reasonable limits.

Care has been taken to describe and to code each of the three constituents of the analysis (body geometry, mapping technique, and gas dynamical effects) separately, to facilitate applications to different geometries or substitution of the present set of equations of motion by other sets. Sections 5 through 10 contain the outline of the code dealing with gas dynamical effects; all their statements and formulae are unaffected by changes in the mapping technique or mapping parameters or in the geometry of the airplane. All expressions related to the mapping are given in Sections 11 and 12. Sections 13 through 15 deal with the choice and treatment of initial conditions. Results of computations based on sample geometries, and discussions are contained in the remaining Sections.

2. Frames of reference

The free stream is assumed to be uniform, with a given Mach number, M_∞ . A Cartesian, orthogonal frame of reference, (x,y,t) is defined as having the y and t -axes in the symmetry plane of the vehicle, the t -axis lying along the fuselage. The unit vectors of the x,y , and t -axes are called \hat{i} , \hat{j} and \hat{k} , respectively. The free stream velocity vector, \vec{V}_∞ , is parallel to the (y,t) -plane; the angle of attack, α , is the angle between \vec{V}_∞ and \hat{k} ; therefore,

$$\vec{V}_\infty = V_\infty(\hat{j} \sin\alpha + \hat{k} \cos\alpha) \quad (1)$$

In each cross-sectional plane, a complex variable, z , is defined as

$$z = x+iy \quad (2)$$

A conformal mapping (details of which will be found in Section

Frames of reference

12) defines a one-to-one correspondence between the portions of interest of the right-hand side of the z -plane and a portion of the right-hand side of a ζ -plane where, by and large, the image of the cross-section of the airplane is nearly circular; it is convenient, thus, to express the complex variable ζ in the form:

$$\zeta = \rho e^{i\theta} \quad (3)$$

The analytic function $\zeta(z)$ implies that ρ and θ are functions of x and y , and vice versa. Such functions, in general, change from one cross-section to another; therefore, we may write:

$$\begin{aligned} \rho &= \rho(x, y, t) & x &= x(\rho, \theta, \tau) \\ \theta &= \theta(x, y, t) & y &= y(\rho, \theta, \tau) \\ \tau &= t & t &= \tau \end{aligned} \quad (4)$$

We must take good care of denoting t by another symbol, τ , when considered in connection with ρ and θ since when t changes and x, y remain unchanged, ρ and θ generally change; consequently, derivatives with respect to t (at constant x and y) generally differ from derivatives with respect to τ (at constant ρ and θ). Let $\rho = b(\theta, \tau)$ and $\rho = c(\theta, \tau)$ be the equations of the image of the airplane body contour and of the image of the bow shock in the ζ -plane. A non-conformal mapping, defined by a suitable function of ρ , θ and τ :

$$\begin{aligned} X &= X(\rho, \theta, \tau) & \rho &= \rho(X, Y, T) \\ Y &= \theta & \theta &= Y \\ T &= \tau & \tau &= T \end{aligned} \quad (5)$$

will transform the region of interest in the right-hand side of the ζ -plane bounded by $\rho = b$ and $\rho = c$ onto a rectangle, bounded by the lines:

$X = 0$, corresponding to $\rho = b$ (body)

Frames of reference

$$X = 1, \quad \text{corresponding to } \rho = c \quad (\text{bow shock}) \quad (6)$$

$$Y = -\pi/2, \quad \text{corresponding to } \theta = -\pi/2 \quad (\text{windward symmetry line})$$

$$Y = \pi/2, \quad \text{corresponding to } \theta = \pi/2 \quad (\text{leeward symmetry line})$$

An example of such a function, $X(\rho, \theta, \tau)$ will be discussed in Section 11.

3. Derivatives related to the mappings.

Let

$$g = \frac{d\zeta}{dz} = Ge^{i\omega} \quad (7)$$

be the complex derivative of ζ with respect to z (at t, τ, T all constant); similarly, let

$$\phi = \frac{\zeta}{g} \frac{d \log g}{dz} = \phi_1 + i\phi_2 \quad (8)$$

From (3) and (7) it follows that

$$\frac{G\zeta}{\rho g} = \frac{\zeta/g}{\text{mod}(\zeta/g)} = e^{i(\theta-\omega)} = \mathcal{L} + i\mathcal{S} \quad (9)$$

where

$$\mathcal{L} = \cos(\theta-\omega), \quad \mathcal{S} = \sin(\theta-\omega) \quad (10)$$

We introduce now the notations, ψ and f , for two analytic functions obtained by differentiating g and ζ with respect to t (that is, at constant x and y):

$$\psi = \frac{\partial \log g}{\partial t} = \psi_1 + i\psi_2 \quad (11)$$

$$f = \frac{\partial \log \zeta}{\partial t} = f_1 + if_2 \quad (12)$$

Recalling that

Derivatives related to the mappings.

$$\frac{dz}{dz} = \frac{\partial(\rho \cos \theta)}{\partial x} + i \frac{\partial(\rho \sin \theta)}{\partial x} = \frac{\partial(\rho \cos \theta)}{i \partial y} + \frac{\partial(\rho \sin \theta)}{\partial y} \quad (13)$$

and

$$\frac{\partial \log \zeta}{\partial t} = \frac{1}{\rho} \frac{\partial \rho}{\partial t} + i \frac{\partial \theta}{\partial t} \quad (14)$$

we obtain:

$$\begin{aligned} \rho_x &= G\mathcal{L}, & \rho_y &= G\mathcal{S}, & \rho_t &= \rho f_1 \\ \theta_x &= -\frac{G}{\rho} \mathcal{S}, & \theta_y &= \frac{G}{\rho} \mathcal{L}, & \theta_t &= f_2 \\ \tau_x &= 0, & \tau_y &= 0, & \tau_t &= 1 \end{aligned} \quad (15)$$

Conversely, noting that

$$x_\tau = -(x_\rho \rho_t + x_\theta \theta_t), \quad y_\tau = -(y_\rho \rho_t + y_\theta \theta_t) \quad (16)$$

we obtain:

$$\begin{aligned} x_\rho &= \mathcal{L}/G, & x_\theta &= -\rho \mathcal{S}/G, & x_\tau &= -(\mathcal{L}f_1 - \mathcal{S}f_2)\rho/G \\ y_\rho &= \mathcal{S}/G, & y_\theta &= \rho \mathcal{L}/G, & y_\tau &= -(\mathcal{S}f_1 + \mathcal{L}f_2)\rho/G \\ t_\rho &= 0, & t_\theta &= 0, & t_\tau &= 1 \end{aligned} \quad (17)$$

Between the two sets, (ρ, θ, τ) and (X, Y, T) , the following relations hold:

$$\begin{aligned} \rho_X &= 1/X_\rho, & \rho_Y &= -X_\theta/X_\rho, & \rho_T &= -X_\tau/X_\rho \\ \theta_X &= 0, & \theta_Y &= 1, & \theta_T &= 0 \end{aligned} \quad (18)$$

$$\tau_X = 0, \quad \tau_Y = 0, \quad \tau_T = 1$$

$$\begin{aligned} X_\rho &= 1/\rho_X, & X_\theta &= -\rho_Y/\rho_X, & X_\tau &= -\rho_T/\rho_X \\ Y_\rho &= 0, & Y_\theta &= 1, & Y_\tau &= 0 \end{aligned} \quad (19)$$

$$T_\rho = 0, \quad T_\theta = 0, \quad T_\tau = 1$$

By combining (17) and (18), we obtain:

Derivatives related to the mappings.

$$\begin{aligned}
 x_X &= \frac{\ell}{GX_\rho}, \quad x_Y = -\frac{\rho}{G} \left(\ell \frac{X_\theta}{\rho X_\rho} + \mathcal{S} \right), \quad x_T = -\frac{\ell}{G} \frac{X_\tau}{X_\rho} - (\ell f_1 - \mathcal{S} f_2) \frac{\rho}{G} \\
 y_X &= \frac{\mathcal{S}}{GX_\rho}, \quad y_Y = \frac{\rho}{G} \left(-\mathcal{S} \frac{X_\theta}{\rho X_\rho} + \ell \right), \quad y_T = -\frac{\mathcal{S}}{G} \frac{X_\tau}{X_\rho} - (\mathcal{S} f_1 + \ell f_2) \frac{\rho}{G} \\
 t_X &= 0, \quad t_Y = 0, \quad t_T = 1
 \end{aligned} \tag{20}$$

The following formulae are also obtained easily:

$$G_\rho = G\phi_1/\rho, \quad G_\theta = -G\phi_2, \quad G_\tau = G[\psi_1 - \phi_1 f_1 + \phi_2 f_2] \tag{21}$$

$$\omega_\rho = \phi_2/\rho, \quad \omega_\theta = \phi_1, \quad \omega_\tau = \psi_2 - \phi_1 f_2 - \phi_2 f_1$$

$$G_x = G^2(\ell\phi_1 + \mathcal{S}\phi_2)/\rho, \quad G_y = G^2(\mathcal{S}\phi_1 - \ell\phi_2)/\rho, \quad G_t = G\psi_1 \tag{22}$$

$$\omega_x = -G(\mathcal{S}\phi_1 - \ell\phi_2)/\rho, \quad \omega_y = G(\ell\phi_1 + \mathcal{S}\phi_2)/\rho, \quad \omega_t = \psi_2$$

4. Important unit vectors

We begin this Section by defining a ρ -line on a $t=\text{constant}$ (physical) cross-sectional plane as a line along which $\theta = \text{constant}$; similarly, a θ -line will be a line on the $t = \text{constant}$ plane along which $\rho = \text{constant}$. The unit vectors, \hat{i} and \hat{j} will be used to identify the tangents to a ρ -line and to a θ -line respectively. Note that

$$\hat{i} = \ell\hat{I} + \mathcal{S}\hat{J}, \quad \hat{I} = \ell\hat{i} - \mathcal{S}\hat{j} \tag{23}$$

$$\hat{j} = -\mathcal{S}\hat{I} + \ell\hat{J}, \quad \hat{J} = \mathcal{S}\hat{j} + \ell\hat{i}$$

By using (20) and (23) for any point,

$$Q = x\hat{i} + y\hat{j} + t\hat{K} \tag{24}$$

we obtain:

Important unit vectors

$$Q_X = \frac{1}{GX_\rho} \hat{i}$$

$$Q_Y = \frac{\rho}{G} \left(-\frac{X_\theta}{\rho X_\rho} \hat{i} + \hat{j} \right) \quad (25)$$

$$Q_T = -\frac{\rho}{G} \left(\frac{X_\tau}{\rho X_\rho} + f_1 \right) \hat{i} - \frac{\rho}{G} f_2 \hat{j} + \hat{k}$$

The unit vector, \hat{N} , normal to an $X = \text{constant}$ surface, is important for the calculation of body and bow shock points. The body, indeed, is defined by $X = 0$ and the bow shock by $X = 1$. In general,

$$\hat{N} = N_1 \hat{i} + N_2 \hat{j} + N_3 \hat{k} = \frac{1}{\text{mod}(Q_Y \times Q_T)} Q_Y \times Q_T \quad (26)$$

where Q is a point on the surface. From (25) it follows that

$$N_1 = \frac{1}{v}, \quad N_2 = \frac{X_\theta}{\rho X_\rho} N_1, \quad N_3 = N_1 d \quad (27)$$

with

$$d = \frac{1}{G} \left[\frac{X_\tau}{X_\rho} + \frac{X_\theta}{X_\rho} f_2 + \rho f_1 \right], \quad v = \left[1 + \left(\frac{X_\theta}{\rho X_\rho} \right)^2 + d^2 \right]^{1/2} \quad (28)$$

In particular, at the body, from (18),

$$X_\theta / \rho X_\rho = -b_Y / b, \quad X_\tau / X_\rho = -b_T \quad (\text{body}) \quad (29)$$

Note also that we can write b_Y or b_θ , and b_T or b_τ , indifferently. Therefore, at the body (27) and (28) take on the form:

$$N_1 = 1/v, \quad N_2 = -(b_Y/b) N_1, \quad N_3 = N_1 d \quad (\text{body}) \quad (30)$$

$$d = -(b_T + b_Y f_2 - b f_1)/G, \quad v = [1 + (b_Y/b)^2 + d^2]^{1/2} \quad (\text{body}) \quad (31)$$

Important unit vectors

Similarly, at the shock,

$$X_\theta/\rho X_\rho = -c_Y/c, \quad X_\tau/X_\rho = -c_T \quad (\text{shock}) \quad (32)$$

$$N_1 = 1/v, \quad N_2 = -(c_Y/c)N_1, \quad N_3 = N_1 d \quad (\text{shock}) \quad (33)$$

$$d = -(c_T + c_Y f_2 - c f_1)/G, \quad v = [1 + (c_Y/c)^2 + d^2]^{1/2} \quad (\text{shock}) \quad (34)$$

Let

$$F(x, y, t) = 0 \quad (35)$$

define the geometry of the body in the physical space. The image of the body in the (ρ, θ, τ) space is

$$\rho = b(\theta, \tau) \quad (36)$$

To evaluate (30) and (31), that is the normal to the body, we need b_θ/b and b_τ . At $\tau = \text{constant}$,

$$F_x(x_\rho b_\theta + x_\theta) + F_y(y_\rho b_\theta + y_\theta) = 0 \quad (37)$$

Consequently, and using (17):

$$\frac{b_\theta}{b} = \frac{\mathcal{L}F_x - \mathcal{L}F_y}{\mathcal{L}F_x + \mathcal{L}F_y} \quad (38)$$

Similarly, at $\theta = \text{constant}$,

$$F_x(x_\rho b_\tau + x_\tau) + F_y(y_\rho b_\tau + y_\tau) + F_t = 0 \quad (39)$$

and

$$b_\tau = -f_2 b_\theta + b f_1 - G \frac{F_t}{\mathcal{L}F_x + \mathcal{L}F_y} \quad (40)$$

Therefore, at the body,

Important unit vectors

$$d = \frac{F_t}{\mathcal{L}F_x + \mathcal{S}F_y} \quad (\text{body}) \quad (41)$$

and (30), (31) can be replaced by the simpler expressions:

$$\begin{aligned} N_1 &= (\mathcal{L}F_x + \mathcal{S}F_y)/v, & N_2 &= (\mathcal{L}F_y - \mathcal{S}F_x)/v, & N_3 &= F_t/v \\ v &= (F_x^2 + F_y^2 + F_t^2)^{1/2} \end{aligned} \quad (\text{body}) \quad (42)$$

The above formulae are general. For any particular geometry, F_x , F_y and F_t must be evaluated.

5. Equations of motion

Having chosen a suitable reference length, x_{ref} , the pressure, density and temperature of the free stream are chosen as reference pressure, density and temperature, respectively (p_{ref} , ρ_{ref} and θ_{ref}). With p , ρ , θ measuring non-dimensional quantities, the equation of state is then

$$p = \rho\theta \quad (43)$$

The reference velocity, u_{ref} , is defined by

$$u_{\text{ref}}^2 = p_{\text{ref}}/\rho_{\text{ref}} = R\theta_{\text{ref}} \quad (44)$$

where R is the gas constant divided by the molecular weight of air. The speed of sound in the free stream, in a non-dimensional form, is then

$$a_{\infty} = \sqrt{\gamma} \quad (45)$$

The logarithm of pressure is denoted by P :

$$P = \ln p \quad (46)$$

A non-dimensional entropy, S (which is the difference between the local entropy and the free-stream entropy divided by c_v) is re-

Equations of motion

lated to non-dimensional temperature and pressure by

$$S = \gamma \ln \theta - (\gamma-1)P, \quad \theta = \exp[(\gamma-1)P/\gamma + S/\gamma] \quad (47)$$

Euler's equations of motion in non-dimensional form are:

$$\begin{aligned} \vec{V} \cdot \nabla P + \gamma \nabla \cdot \vec{V} &= 0 \\ \frac{1}{2} \nabla(\vec{V}^2) - \vec{V} \times \nabla \times \vec{V} + \theta \nabla P &= 0 \\ \vec{V} \cdot \nabla S &= 0 \end{aligned} \quad (48)$$

With $\hat{k} = \hat{K}$, let

$$\vec{V} = w(\vec{\chi} + \hat{k}) \quad (49)$$

where

$$\vec{\chi} = \sigma \hat{i} + \eta \hat{j} \quad (50)$$

and let

$$\nabla_1 = \frac{\partial}{\partial x} \hat{i} + \frac{\partial}{\partial y} \hat{j} \quad (51)$$

Note that

$$\begin{aligned} \vec{V} \cdot \nabla P &= w(\vec{\chi} + \hat{k}) \cdot (\nabla_1 P + P_t \hat{k}) = w \vec{\chi} \cdot \nabla_1 P + w P_t \\ \nabla \cdot \vec{V} &= \nabla_1 \cdot [w(\vec{\chi} + \hat{k})] + w_t = \vec{\chi} \cdot \nabla_1 w + w \nabla_1 \cdot \vec{\chi} + w_t \\ \frac{1}{2} \nabla(\vec{V}^2) &= w \nabla w (\vec{\chi}^2 + 1) + \frac{1}{2} w^2 \nabla_1 \vec{\chi}^2 + \frac{1}{2} w^2 (\vec{\chi}^2)_t \hat{k} \\ \vec{V} \times \nabla \times \vec{V} &= -w(\nabla_1 w \cdot \vec{\chi} + w_t)(\vec{\chi} + \hat{k}) + w \nabla w (\vec{\chi}^2 + 1) + w^2 [(\vec{\chi}_t \cdot \vec{\chi}) \hat{k} - \vec{\chi}_t + \vec{\chi} \times \nabla_1 \times \vec{\chi}] \end{aligned} \quad (52)$$

therefore, (48) takes the form:

$$\begin{aligned} w(\vec{\chi} \cdot \nabla_1 P + P_t) + \gamma(\vec{\chi} \cdot \nabla_1 w + w \nabla_1 \cdot \vec{\chi} + w_t) &= 0 \\ \frac{1}{2} w^2 \nabla_1 \vec{\chi}^2 + w(\nabla_1 w \cdot \vec{\chi} + w_t) \vec{\chi} + w^2 \vec{\chi}_t - w^2 \vec{\chi} \times \nabla_1 \times \vec{\chi} + \theta \nabla_1 P &= 0 \\ w(\nabla_1 w \cdot \vec{\chi} + w_t) + \theta P_t &= 0 \end{aligned} \quad (53)$$

Equations of motion

$$\vec{x} \cdot \nabla_1 S + S_t = 0$$

The third of these equations can be used to simplify the first and second equation; finally, the following system is obtained:

$$\begin{aligned} (1 - \frac{a^2}{w^2})P_t + \vec{x} \cdot \nabla_1 P + \gamma \nabla_1 \cdot \vec{x} &= 0 \\ \frac{1}{2} \nabla_1 \vec{x}^2 - \vec{x} \times \nabla_1 \times \vec{x} + \frac{\theta}{w^2} (\nabla_1 P - P_t \vec{x}) + \vec{x}_t &= 0 \end{aligned} \quad (54)$$

$$\vec{x} \cdot \nabla_1 S + S_t = 0$$

The third of (53) is not needed; the above system is composed of four scalar equations for the two unknown scalars, P and S and the two-component unknown vector, \vec{x} . Once P and S are determined, θ is obtained from (47); the modulus of the velocity, q, is obtained from

$$q^2 = \frac{2\gamma}{\gamma-1} (\theta_0 - \theta) \quad (55)$$

where θ_0 is the (non-dimensional) stagnation temperature, and w follows from

$$w^2(1 + \sigma^2 + \eta^2) = q^2 \quad (56)$$

There are definite advantages in using (54) as a basic system of equations (instead of (48) or of equations in divergence form). It contains only four differential equations to be integrated, and it provides a clear separation of unknowns, S on one side and P and \vec{x} on the other side, which is particularly welcome in problems where strong entropy gradients occur [4,5]. Another advantage of (54) stems from the fact that ∇_1 operates on the (x,y)-plane only; therefore, it can be expressed in terms of ρ and θ as independent variables, using \hat{i} and \hat{j} as unit vectors. In particular, note that

$$\begin{aligned} \nabla_1 P &= G(P_\rho \hat{i} + \frac{1}{\rho} P_\theta \hat{j}) \\ \vec{x} \cdot \nabla_1 P &= G(\sigma P_\rho + \frac{\eta P_\theta}{\rho}) \end{aligned}$$

Equations of motion

$$\vec{\chi} \times \nabla_1 \times \vec{\chi} = \frac{G^2}{\rho} \left[\left(\frac{\rho \eta}{G} \right)_\rho - \left(\frac{\sigma}{G} \right)_\theta \right] (\eta \hat{i} - \sigma \hat{j}) \quad (57)$$

$$\nabla_1 \cdot \vec{\chi} = \frac{G^2}{\rho} \left[\left(\frac{\rho \sigma}{G} \right)_\rho + \left(\frac{\eta}{G} \right)_\theta \right]$$

$$\frac{1}{2} \nabla_1 (\vec{\chi}^2) = G [(\sigma \sigma_\rho + \eta \eta_\rho) \hat{i} + \frac{1}{\rho} (\sigma \sigma_\theta + \eta \eta_\theta) \hat{j}]$$

$$\vec{\chi}_t = [\sigma_t + (\omega_t - \theta_t) \eta] \hat{i} + [\eta_t + (\theta_t - \omega_t) \sigma] \hat{j}$$

These expressions can be substituted into (54); in doing it, however, note that t also must be substituted by τ , and that, for any function, Φ :

$$\Phi_t = \Phi_\tau + \Phi_\rho \rho_t + \Phi_\theta \theta_t = \Phi_\tau + \rho f_1 \Phi_\rho + f_2 \Phi_\theta \quad (58)$$

Using the notations:

$$\kappa = 1 - \frac{a^2}{w^2}$$

$$A_1 = G \frac{\sigma}{\kappa} + \rho f_1, \quad A_2 = \frac{G \eta}{\rho \kappa} + f_2 \quad (59)$$

$$B_1 = G \sigma + \rho f_1, \quad B_2 = \frac{G}{\rho} \eta + f_2$$

$$D = \frac{G}{\rho} [\eta(1 - \phi_1) - \sigma \phi_2] + f_2 - \psi_2$$

and taking (21) and (22) into account, (54) become:

$$\begin{aligned} P_\tau + A_1 P_\rho + A_2 P_\theta + \frac{\gamma G}{\kappa} \left(\sigma_\rho + \frac{1}{\rho} \eta_\theta \right) + \frac{\gamma G}{\kappa \rho} [\sigma(1 - \phi_1) + \eta \phi_2] &= 0 \\ \sigma_\tau + B_1 \sigma_\rho + B_2 \sigma_\theta + \frac{\theta}{w^2} [-\sigma P_\tau + (G - \sigma \rho f_1) P_\rho - \sigma f_2 P_\theta] - \eta D &= 0 \\ \eta_\tau + B_1 \eta_\rho + B_2 \eta_\theta + \frac{\theta}{w^2} [-\eta P_\tau - \rho \eta f_1 P_\rho + \left(\frac{G}{\rho} - \eta f_2 \right) P_\theta] + \sigma D &= 0 \end{aligned} \quad (60)$$

$$S_\tau + B_1 S_\rho + B_2 S_\theta = 0$$

Equations of motion

The final form of the equations of motion is obtained by expressing the derivatives in terms of X , Y and T , considering that, for any function ϕ :

$$\begin{aligned}\phi_\rho &= \phi_X X_\rho \\ \phi_\theta &= \phi_Y + \phi_X X_\theta \\ \phi_\tau &= \phi_T + \phi_X X_\tau\end{aligned}\tag{61}$$

and, consequently:

$$\begin{aligned}\phi_\tau + B_1\phi_\rho + B_2\phi_\theta &= \phi_T + E\phi_X + B_2\phi_Y \\ \phi_\tau + A_1\phi_\rho + A_2\phi_\theta &= \phi_T + C\phi_X + A_2\phi_Y\end{aligned}\tag{62}$$

where

$$C = X_\tau + A_1X_\rho + A_2X_\theta, \quad E = X_\tau + B_1X_\rho + B_2X_\theta\tag{63}$$

With the additional notations:

$$\begin{aligned}L &= \sigma(1-\phi_1) + \phi_2 \\ F &= -\sigma X_\tau + (G-\sigma\rho f_1)X_\rho - \sigma f_2 X_\theta \\ H &= -\eta X_\tau - \rho\eta f_1 X_\rho + \left(\frac{G}{\rho} - \eta f_2\right)X_\theta\end{aligned}\tag{64}$$

the equations to be integrated at every grid point are:

$$\begin{aligned}P_T + CP_X + A_2P_Y + \frac{\gamma G}{\kappa} [X_\rho \sigma_X + \frac{1}{\rho} (\eta_Y + X_\theta \eta_X L)] &= 0 \\ \sigma_T + E\sigma_X + B_2\sigma_Y + \frac{\theta}{w^2} [-\sigma P_T + FP_X - \sigma f_2 P_Y] - \eta D &= 0 \\ \eta_T + E\eta_X + B_2\eta_Y + \frac{\theta}{w^2} [-\eta P_T + HP_X + \left(\frac{G}{\rho} - \eta f_2\right)P_Y] + \sigma D &= 0 \\ S_T + ES_X + B_2S_Y &= 0\end{aligned}\tag{65}$$

6. The integration method

The equations of motion are integrated using a predictor-corrector method. If we denote by f the initial value of P , σ , n or S , by \tilde{f} the corresponding value at the end of the predictor stage, and by f^N the value at the end of the corrector stage, that is, the final value, we use the formulae:

$$\tilde{f} = f + f_T \Delta T \quad (66)$$

and

$$f^N = \frac{1}{2}(f + \tilde{f} + \tilde{f}_T \Delta T) \quad \text{or} \quad f^N = \tilde{f} + \frac{1}{2}(\tilde{f}_T - f_T) \Delta T \quad (67)$$

in the predictor and the corrector stage, respectively.

Many different integration schemes can be devised, all making use of (66) and (67), the difference residing in the way f_T and \tilde{f}_T are defined. For example, the original scheme suggested by MacCormack [6] used the equations of motion in divergence form and discretized the space-like derivatives using forward differences in the predictor and backward differences in the corrector (or vice versa). Without recasting the equations in divergence form, I used the same alternating forward-backward differencing in a large number of works, and I called it the MacCormack scheme. The entropy equation, however, was always integrated approximating the derivatives with upwind differences, in order to maintain consistency of the numerical approximation with the physical nature of the problem [4].

Numerical work on three-dimensional, steady, supersonic flows which began under promising auspices, showed that, as the body geometries became more complicated and the local Mach numbers closer to 1, the MacCormack scheme was losing accuracy and reliability. Since the most probable cause of failure was a lack of consistency between the physical domain of dependence of a point and its numerical domain of dependence, in the second phase of the work related to the present paper I tried to approx-

The integration method

imate Lagrangian derivatives by upwind approximations, and I attempted to give an overall second order accuracy to the scheme by a proper definition of difference operators in the predictor and corrector stages. Finally, I decided to adopt the λ -scheme [3] because it seems to offer a maximum of domain-of-dependence consistency together with second-order accuracy. Referring to [3] for a discussion and a detailed description of the scheme, we can see how the scheme is applied to the present problems, in what follows.

The first three equations (65) are split into two systems:

$$\begin{aligned}
 P_T^X + CP_X + \frac{\gamma GX_\rho}{\kappa} \sigma_X + \frac{\gamma GX_\theta}{\kappa \rho} \eta_X + \frac{\gamma GL}{\kappa \rho} &= 0 \\
 \sigma_T^X + \frac{\theta F}{w^2} P_X + E \sigma_X - \eta D - \frac{\theta \sigma}{w^2} P_T^X &= 0 \\
 \eta_T^X + \frac{\theta H}{w^2} P_X + E \eta_X + \sigma D - \frac{\theta \eta}{w^2} P_T^X &= 0
 \end{aligned} \tag{68}$$

and

$$\begin{aligned}
 P_T^Y + A_2 P_Y + \frac{\gamma G}{\kappa \rho} \eta_Y &= 0 \\
 \sigma_T^Y - \frac{\theta \sigma}{w^2} f_2 P_Y + B_2 \eta_Y - \frac{\theta \sigma}{w^2} \sigma P_T^Y &= 0 \\
 \eta_T^Y + \frac{\theta}{w^2} \left(\frac{G}{\rho} - \eta f_2 \right) P_Y + B_2 \eta_Y - \frac{\theta \eta}{w^2} P_T^Y &= 0
 \end{aligned} \tag{69}$$

Using the notations of [3],

$$\begin{aligned}
 a_{11} &= C, \quad a_{12} = \frac{\gamma G}{\kappa} X_\rho, \quad a_{13} = \frac{\gamma G}{\kappa \rho} X_\theta, \quad c_1 = \frac{\gamma GL}{\kappa \rho} \\
 a_{21} &= \frac{\theta F}{w^2}, \quad a_{22} = E, \quad a_{23} = 0, \quad c_2 = -\eta D, \quad k_2 = \frac{\theta \sigma}{w^2} \\
 a_{31} &= \frac{\theta H}{w^2}, \quad a_{32} = 0, \quad a_{33} = a_{22} = E, \quad c_3 = \sigma D, \quad k_3 = \frac{\theta \eta}{w^2}
 \end{aligned} \tag{70}$$

The integration method

$$\begin{aligned}
 b_{11} &= A_2, & b_{12} &= 0, & b_{13} &= \frac{\gamma G}{\kappa \rho} \\
 b_{21} &= -\frac{\theta \sigma}{w^2} f_2, & b_{22} &= B_2, & b_{23} &= 0, & \kappa_2 &= \frac{\theta \sigma}{w^2} \\
 b_{31} &= \frac{\theta}{w^2} \left(\frac{G}{\rho} - \eta f_2 \right), & b_{32} &= 0, & b_{33} &= b_{22} = B_2, & \kappa_3 &= \frac{\theta \eta}{w^2}
 \end{aligned} \quad (71)$$

Therefore,

$$a_{11} + a_{22} + a_{13} \kappa_3 + a_{12} \kappa_2 = 2C$$

and, consequently,

$$\beta^X = [(\sigma X_\rho + \eta X_\theta / \rho)^2 + \kappa (X_\rho^2 + X_\theta^2 / \rho^2)]^{1/2}, \quad \beta^Y = (\eta^2 + \kappa)^{1/2} \quad (72)$$

$$\lambda_1^X = C - \frac{aG}{\kappa w} \beta^X, \quad \lambda_2^X = C + \frac{aG}{\kappa w} \beta^X, \quad \lambda_3^X = E \quad (73)$$

$$\lambda_1^Y = A_2 - \frac{aG}{\kappa w \rho} \beta^Y, \quad \lambda_2^Y = A_2 + \frac{aG}{\kappa w \rho} \beta^Y, \quad \lambda_3^Y = B_2 \quad (74)$$

$$\alpha^X = a_{22} - \lambda_1^X + a_{12} \kappa_2 + a_{13} \kappa_3 = 2C - a_{11} - \lambda_1^X = C - \lambda_1^X = \frac{aG}{\kappa w} \beta^X \quad (75)$$

$$\alpha^Y = b_{22} - \lambda_1^Y + b_{13} \kappa_3 = 2A_2 - b_{11} - \lambda_1^Y = A_2 - \lambda_1^Y = \frac{bG}{\kappa w \rho} \beta^Y \quad (76)$$

To determine P_T^X and P_T^Y , Eq. (51) from [3] and its Y-counterpart are used. Similarly, to determine the auxiliary quantities ϕ^X , ϕ^Y , ψ^X and ψ^Y , Eqs. (52) and (54) from [3] and their Y-counterparts are used. Moreover,

$$\Delta^X = \begin{vmatrix} a_{12} & a_{13} \\ \mu_{32}^X & \mu_{33}^X \end{vmatrix}, \quad \Delta^Y = \begin{vmatrix} 0 & b_{13} \\ \mu_{32}^Y & \mu_{33}^Y \end{vmatrix} \quad (77)$$

$$\sigma_T^X = 1/\Delta^X \begin{vmatrix} \phi^X & a_{13} \\ \psi^X & \mu_{33}^X \end{vmatrix}, \quad \sigma_T^Y = 1/\Delta^Y \begin{vmatrix} \phi^Y & b_{13} \\ \psi^Y & \mu_{33}^Y \end{vmatrix} \quad (78)$$

The integration method

$$\eta_T^X = 1/\Delta^X \begin{vmatrix} a_{12} & \phi^X \\ \mu_{32}^X & \psi^X \end{vmatrix}, \quad \eta_T^Y = 1/\Delta^Y \begin{vmatrix} 0 & \phi^Y \\ \mu_{32}^Y & \psi^Y \end{vmatrix} \quad (79)$$

Once expressions of the type f_T^X and f_T^Y have been evaluated, f_T is obtained as

$$f_T = f_T^X + f_T^Y \quad (80)$$

All X- and Y-derivatives are approximated by expressions, generally denoted by f_{X1} , f_{X2} , f_{Y1} , f_{Y2} , which are defined in Section 3 of [3].

Approximations to S_X and S_Y are always defined using upwind information only; two- and three-point formulae of the type shown in (14) and (15) of [3] are used in order to provide second-order accuracy.

7. Characteristic equation for body and shock points

Although the following discussion could be conducted on the basis of the characteristic equations of the preceding Section, it is simpler to proceed without splitting the equations, as follows. We build up a characteristic equation in the (X,T) plane by multiplying the first three equations (65) by μ_1 , μ_2 , and μ_3 , respectively, adding, and calling λ the slope of the characteristic in the (X,T) plane:

$$[\mu_1 - \frac{\theta}{w^2}(\sigma\mu_2 + \eta\mu_3)](P_T + \lambda P_X) + \mu_2(\sigma_T + \lambda\sigma_X) + \mu_3(\eta_T + \lambda\eta_X) = R_0 \quad (81)$$

where R_0 contains all Y-derivatives and all non-differentiated terms. In turn, λ is defined by

Characteristic equation for body and shock points

$$\begin{vmatrix} C-\lambda & \frac{\theta}{w^2}(F+\sigma\lambda) & \frac{\theta}{w^2}(H+\eta\lambda) \\ \frac{\gamma G}{\kappa} X_\rho & E-\lambda & 0 \\ \frac{\gamma G}{\kappa \rho} X_\theta & 0 & E-\lambda \end{vmatrix} = 0 \quad (82)$$

that is,

$$(E-\lambda)(C-\lambda) - \frac{a^2 G}{w^2 \kappa} [X_\theta (H+\eta\lambda)/\rho + X_\rho (F+\sigma\lambda)] = 0$$

or

$$\lambda^2 - 2(X_\tau + A_1 X_\rho + A_2 X_\theta)\lambda + EC - \frac{a^2 G}{w^2 \kappa} (FX_\rho + HX_\theta/\rho) = 0$$

which, after some manipulations, yields:

$$\lambda = C \pm \beta \frac{aG}{w\kappa} \quad (83)$$

$$\beta = [(\sigma X_\rho + \eta X_\theta/\rho)^2 + \kappa(X_\rho^2 + X_\theta^2/\rho^2)]^{1/2} \quad (84)$$

The lower sign and the upper sign must be used at body and bow shock points, respectively. From (82), we obtain

$$\mu_1 = E - \lambda, \quad \mu_2 = -\frac{\gamma G}{\kappa} X_\rho, \quad \mu_3 = -\frac{\gamma G}{\kappa \rho} X_\theta \quad (85)$$

$$-\mu_1 + \frac{\theta}{w^2}(\sigma \mu_2 + \eta \mu_3) = \pm \beta \frac{aG}{w\kappa} \quad (86)$$

The compatibility equation (81) is then

$$\pm(P_T + \lambda P_X) + \frac{\gamma W}{\beta a} [X_\rho(\sigma_T + \lambda \sigma_X) + X_\theta(\eta_T + \lambda \eta_X)/\rho] = R_0 \quad (87)$$

8. Treatment of body points

At body points, the boundary condition,

$$\vec{V} \cdot \vec{N} = 0 \quad (88)$$

yields

$$\sigma - \eta b_Y/b + d = 0 \quad (89)$$

if (49), (50), (30) and (31) are taken into account. On the other hand, (63) and (29) give

$$E = X_\rho (-b_T + B_1 - B_2 b_Y) \quad (90)$$

and, using (59) and (31), it is easy to see that

$$E = 0 \quad (91)$$

Following de Neef's suggestions [2], we evaluate the pressure at the body as follows. If we use the formulae of the preceding Section to obtain P_T , σ_T and η_T at a body point, we obtain three values which satisfy (87) but do not necessarily satisfy the boundary conditions. Let us denote them by a superscript E. On the other hand, there exist a set of values, P_T , σ_T and η_T which are the exact solutions and consequently satisfy both (87) and the boundary condition. If we write (87) twice, once for the E-values and once for the exact values, and subtract, we obtain

$$P_T - P_T^E - \frac{\gamma w}{\beta a} X_\rho \left[\sigma_T - \frac{b_Y}{b} \eta_T - \sigma_T^E + \frac{b_Y}{b} \eta_T^E \right] = 0 \quad (92)$$

Considering now that, across the interval ΔT , it is, in general,

$$f_T = (f - f_0)/\Delta T, \quad f_T^E = (f^E - f_0)/\Delta T \quad (93)$$

if f_0 are initial values, f are exactly updated values and f^E are

Treatment of body points

values updated following the procedure of the preceding Section. Therefore, (92) can be substituted by

$$P = P^E + \frac{\gamma w}{\beta a} X_\rho \left[\sigma - \frac{b_Y}{b} \eta - \sigma^E + \frac{b_Y}{b} \eta^E \right] \quad (94)$$

Using (89) and the first of (31), the equation to determine P at a body point is finally put into the form:

$$P = P^E - \frac{\gamma w}{\beta a} X_\rho \left[\sigma^E - \frac{b_Y}{b} \eta^E + (b f_1 - b_Y f_2 - b_t) / G \right] \quad (95)$$

The kinematical unknowns at body points can be determined as follows. Let \tilde{v} be the velocity component tangent to the body in the cross-sectional plane:

$$\tilde{v} = w (\eta + \sigma b_Y / b) \quad (96)$$

The third of (53) in the (X, Y, T) frame, with $E=0$, reads:

$$w_T + B_2 w_Y + \frac{\theta}{w} [P_T + (X_T + \rho X_\rho f_1 + X_\theta f_2) P_X + f_2 P_Y] = 0 \quad (97)$$

If (97) is multiplied by \tilde{v}/w^2 and added to the third of (65) and the second of (65) multiplied by b_Y/b , the following equation is obtained:

$$\tilde{v}_T = -B_2 \tilde{v}_Y + w \left[\sigma \left(\frac{b_Y}{b} \right)_T + \sigma B_2 \left(\frac{b_Y}{b} \right)_Y - \frac{G\theta}{\rho w^2} P_Y - D \left(\sigma - \frac{b_Y}{b} \eta \right) \right] \quad (98)$$

Note that the Lagrangian derivative of \tilde{v} , as expressed by (98) in the (X, Y, T) frame, depends on the geometry of the body and on the Y -derivative of P only. It is crucial to approximate \tilde{v}_Y using upwind information [5].

From the body geometry and local values of \tilde{v} and q , the corresponding values of σ and η are obtained as follows. First, v is evaluated using (31); then, from (96), (56) and (75):

$$w = \frac{1}{v} [q^2 (1 + b_Y^2 / b^2) - \tilde{v}^2]^{1/2} \quad (99)$$

Treatment of body points

$$\sigma = \frac{(\tilde{v}/w)(b_Y/b) - d}{1 + (b_Y/b)^2} \quad (100)$$

$$\eta = \tilde{v}/w - \sigma b_Y/b \quad (101)$$

9. Treatment of bow shock points

Let

$$\hat{N} = N_1 \hat{i} + N_2 \hat{j} + N_3 \hat{k} \quad (102)$$

be the unit vector normal to the bow shock surface. The values of N_1 , N_2 , N_3 are the same as the values defined by (33). The velocity component normal to the shock in front of it, \tilde{u}_∞ , is

$$\tilde{u}_\infty = \vec{V}_\infty \cdot \hat{N} = u_\infty N_1 + v_\infty N_2 + w_\infty N_3 \quad (103)$$

where

$$\begin{aligned} u_\infty &= V_\infty \xi \sin \alpha \\ v_\infty &= V_\infty \zeta \sin \alpha \\ w_\infty &= V_\infty \cos \alpha \end{aligned} \quad (104)$$

If we denote by \tilde{u} the corresponding velocity component behind the shock, the velocity vector, \vec{V} behind the shock is:

$$\vec{V} = \vec{V}_\infty + (\tilde{u} - \tilde{u}_\infty) \hat{N} \quad (105)$$

The Rankine-Hugoniot conditions provide the increment in P and the ratio $\tilde{u}/\tilde{u}_\infty$ across the shock (here P is the logarithm of pressure behind the shock; let us keep in mind that $P_\infty=0$):

$$P = \ln \frac{2}{\gamma+1} + \ln \left(\tilde{u}_\infty^2 - \frac{\gamma-1}{2} \right) \quad (106)$$

$$\tilde{u} = \frac{\gamma-1}{\gamma+1} \tilde{u}_\infty + \frac{2\gamma}{\gamma+1} \frac{1}{\tilde{u}_\infty} \quad (107)$$

Since (106) and (107) are identically satisfied at any T , and P

and \tilde{u} are functions of \tilde{u}_∞ alone,

$$P_T = \frac{\partial P}{\partial \tilde{u}_\infty} \tilde{u}_{\infty T} \quad (108)$$

$$\tilde{u}_T = \frac{\partial \tilde{u}}{\partial \tilde{u}_\infty} u_{\infty T} \quad (109)$$

where

$$\frac{\partial P}{\partial \tilde{u}_\infty} = \frac{2\tilde{u}_\infty}{\tilde{u}_\infty^2 - \frac{\gamma-1}{2}}, \quad \frac{\partial \tilde{u}}{\partial \tilde{u}_\infty} = \frac{\gamma-1}{\gamma+1} - \frac{2\gamma}{\gamma+1} \frac{1}{\tilde{u}_\infty^2} \quad (110)$$

In turn, from (103), (9), (18) and (21):

$$\begin{aligned} u_{\infty T} &= -v_{\infty} \omega_T \\ v_{\infty T} &= u_{\infty} \omega_T \\ w_{\infty T} &= 0 \end{aligned} \quad (111)$$

and

$$\omega_T = \psi_2 - f_2 \phi_1 - f_1 \phi_2 + \phi_2 c_T / c \quad (112)$$

Therefore,

$$\tilde{u}_{\infty T} = -(v_{\infty} N_1 - u_{\infty} N_2) \omega_T + u_{\infty} N_{1T} + v_{\infty} N_{2T} + w_{\infty} N_{3T} \quad (113)$$

We can proceed now as at body points, by writing first a characteristic equation similar to (91), as obtainable from the integration of Euler's equations as executed in Section 6:

$$P_T^E + \lambda P_X + \frac{\gamma W}{\beta a} X_\rho [\sigma_T^E + \lambda \sigma_X - \frac{c_Y}{c} (\eta_T^E + \lambda \eta_X)] = R_0 \quad (114)$$

where, as in the preceding Section, the superscript E means that the values are compatible with Euler's equations but not necessarily with the Rankine-Hugoniot conditions. On the other hand, the same equations can be rewritten for the exact values, which satisfy the Rankine-Hugoniot conditions:

$$P_T + \lambda P_X + \frac{\gamma W}{\beta a} X_p [\sigma_T + \lambda \sigma_X - \frac{c_Y}{c} (\eta_T + \lambda \eta_X)] = R_0 \quad (115)$$

By subtracting (114) from (115), we obtain:

$$P_T - P_T^E + \frac{\gamma W}{\beta a} X_p [\sigma_T - \sigma_T^E - \frac{c_Y}{c} (\eta_T - \eta_T^E)] = 0 \quad (116)$$

Now, P_T , σ_T and η_T can be interpreted as the sum of two terms, as follows:

$$f_T = f_T^* + \frac{\partial f}{\partial c_T} c_{TT}$$

if f_T^* is obtained from the Rankine-Hugoniot conditions under the assumption that c_T remains constant. From (34),

$$\partial d / \partial c_T = -1/G = C_2 \quad (117)$$

$$\partial v / \partial c_T = dC_2/v = C_4 \quad (118)$$

From (33),

$$\partial N_1 / \partial c_T = -C_4/v^2 = C_6 \quad (119)$$

$$\partial N_2 / \partial c_T = -c_Y C_6/c = C_8 \quad (120)$$

$$\partial N_3 / \partial c_T = C_6 d + N_1 C_2 = C_{10} \quad (121)$$

Then,

$$\partial \tilde{u}_\infty / \partial c_T = u_\infty C_6 + v_\infty C_8 + w_\infty C_{10} = C_{12} \quad (122)$$

From (108) and (109),

$$\partial P / \partial c_T = \frac{\partial P}{\partial \tilde{u}_\infty} C_{12} = C_{14} \quad (123)$$

$$\partial \tilde{u}_T / \partial c_T = \frac{\partial \tilde{u}}{\partial \tilde{u}_\infty} C_{12} = C_{16} \quad (124)$$

Then,

Treatment of bow shock points

$$\partial(\tilde{u}-\tilde{u}_\infty)/\partial c_T = C_{16}-C_{12} = C_{18} \quad (125)$$

With

$$\vec{V} = u\hat{i} + v\hat{j} + w\hat{k} \quad (126)$$

it follows from (105) that

$$\begin{aligned} u &= u_\infty + (\tilde{u}-\tilde{u}_\infty)N_1 \\ v &= v_\infty + (\tilde{u}-\tilde{u}_\infty)N_2 \\ w &= w_\infty + (\tilde{u}-\tilde{u}_\infty)N_3 \end{aligned} \quad (127)$$

Therefore,

$$\begin{aligned} \partial u/\partial c_T &= C_{18}N_1 + (\tilde{u}-\tilde{u}_\infty)C_6 = C_{20} \\ \partial v/\partial c_T &= C_{18}N_2 + (\tilde{u}-\tilde{u}_\infty)C_8 = C_{22} \\ \partial w/\partial c_T &= C_{18}N_3 + (\tilde{u}-\tilde{u}_\infty)C_{10} = C_{24} \end{aligned} \quad (128)$$

and

$$\begin{aligned} \partial \sigma/\partial c_T &= (C_{20}-\sigma C_{24})/w = C_{26} \\ \partial \eta/\partial c_T &= (C_{22}-\eta C_{24})/w = C_{28} \end{aligned} \quad (129)$$

By replacing (123) and (129) into (116), the latter becomes

$$P_T^* + C_{14}d_{TT} - P_T^E + \frac{\gamma w}{\beta a} X_\rho [\sigma_T^* + C_{26}c_{TT} - \sigma_T^E - \frac{c_Y}{c}(\eta_T^* + C_{28}c_{TT} - \eta_T^E)] = 0 \quad (130)$$

Let

$$D_7 = -1/[C_{14} + \frac{\gamma w}{\beta a} X_\rho (C_{26} - \frac{c_Y}{c} C_{28})] \quad (131)$$

Then,

$$c_{TT} = D_7 (P_T^* - P_T^E + \frac{\gamma w}{\beta a} X_p [\sigma_T^* - \sigma_T^E - \frac{c_Y}{c} (\eta_T^* - \eta_T^E)]) \quad (132)$$

Using the same argument as in (93), the increment in c_T across the entire integration step, Δc_T , turns out to be:

$$\Delta c_T = D_7 (P_T^* - P_T^E + \frac{\gamma w}{\beta a} X_p [\sigma_T^* - \sigma_T^E - \frac{c_Y}{c} (\eta_T^* - \eta_T^E)]) \quad (133)$$

The value of c_T can thus be updated and, by a further integration, c itself can be updated. Once a new shock geometry, $\rho=c(\theta, \tau)$, is obtained, the new \hat{N} and \tilde{u}_∞ are evaluated; then, (106) and (107) can be applied to compute P and \tilde{u} . The three velocity components follow from (127); therefore $\sigma (=u/w)$ and $\eta (=v/w)$ are made known. Finally, S is given by

$$S = P - \gamma \ln(\tilde{u}_\infty/\tilde{u}) \quad (134)$$

10. General outline of one integration step

The equations obtained in the preceding Sections are used to proceed from a station, t , to a station, $t+\Delta t$, as follows.

Predictor stage

Given, original values of P , σ , η , S , c , c_Y , c_T , b , b_Y , b_T , ζ , z , G , f , ϕ and ψ at all nodal points (including body and shock points), compute q^2, θ, w and all auxiliary quantities necessary to determine λ_i^X and λ_i^Y , ($i=1,2,3$), where λ_3^X and λ_3^Y are 'streamline slopes' used to identify the upwind direction for the proper approximation of X - and Y -derivatives, when needed; specifically, $\lambda_3^X=E$ and $\lambda_3^Y=B_2$. Compute all X - and Y -derivatives. Compute $P_T, \sigma_T, \eta_T, S_T$. At all body points, compute \tilde{v}_T . At all nodal points, update P, σ, η and S using (66). At all body points, update \tilde{v} using (66). At all shock points, update c using the formula:

$$c^N = c + c_T \Delta T + \frac{1}{2} c_{TT} \Delta T^2 \quad (135)$$

At all shock points, compute c_Y (from the updated shock geometry), $d, v, \hat{N}, u_\infty, v_\infty, \tilde{u}_\infty, P^*, \tilde{u}^*$, all the coefficients needed to

General outline of one integration step

evaluate D_7 , Δc_T , and an intermediate value of c_T ,

$$\tilde{c}_T = c_T + \Delta c_T \quad (136)$$

Move to the station defined by $t+\Delta t$, compute the new geometry of the body and b_Y .

Corrector stage

The computation is restarted as at the beginning of the predictor stage. The geometry and the grid, however, are now those of the new station, and all the variables have their predicted values at $t+\Delta t$ as well. The updating of P, σ, η, S and \tilde{v} is performed using (67).

At all shock points, d is recomputed using the original value of c_T , and all the other values mentioned in the predictor stage are recomputed. An equation similar to (136) is used to determine the final value of c_T :

$$c_T^N = c_T + \Delta c_T \quad (137)$$

where c_T is, once more, the original value at the beginning of the step. Once c_T is updated, a new value of d is obtained from:

$$\Delta d = \Delta c_T / G \quad (138)$$

with the new value of d , v, \hat{N} , and \tilde{u}_∞ are determined; then one proceeds as mentioned at the end of the preceding Section.

At all body points, (95) is applied to update P ; then, from P and the updated value of S , θ and q^2 are obtained; σ and η follow from (99), (100) and (101).

11. Coordinate normalization and grid stretching

The object of the transformation (5) is twofold. It defines a variable X which is constant (equal to zero) along the body and also constant (equal to 1) along the bow shock. In addition, it provides a stretching of coordinates according to which evenly spaced grid points on the X -axis correspond to unevenly spaced points on the ρ -lines. The latter property is used to accumulate θ -lines in the vicinity of the body where a stronger resolution is needed.

The values of the derivatives, X_ρ , X_θ and X_τ , depend on the choice of the stretching function $X(\rho, \theta, \tau)$. In this Section we give an example of such a function. If the definition of $X(\rho, \theta, \tau)$ is changed, the definitions of X_ρ , X_θ and X_τ must be changed accordingly. The rest of the program does not need to be altered.

Let

$$\rho = c + \varnothing \tanh[\alpha(X-1)] \quad (139)$$

with

$$\varnothing = \frac{c-b}{\tanh\alpha} \quad (140)$$

Obviously, X as defined by (139) satisfies conditions (6). Different values of α provide different degrees of accumulation of θ -lines near the body. To give an idea of the effect of α , let $b=0$, $c=1$. Fig. 1 plots X vs. ρ for various values of α . Clearly, strong stretching effects begin to appear for values of α larger than 2.

It is easily proven that:

$$X_\rho = \frac{\varnothing}{\alpha[\varnothing^2 - (\rho-c)^2]} \quad (141)$$

$$X_\theta = -\left[\frac{\rho-c}{\tanh\alpha}(c_Y - b_Y) + \varnothing c_Y\right] X_\rho / \varnothing \quad (142)$$

$$X_{\tau} = -\left[\frac{\rho-c}{\tanh\alpha}(c_T-b_T)+\emptyset c_T\right]X_{\rho}/\emptyset \quad (143)$$

On those rare occasions when stretching is not needed, the following definition of X can be used:

$$X = \frac{\rho-b}{c-b} \quad (144)$$

from which

$$X_{\rho} = \frac{1}{c-b} \quad (145)$$

$$X_{\theta} = [(X-1)b_Y - Xc_Y]X_{\rho} \quad (146)$$

$$X_{\tau} = [(X-1)b_T - Xc_T]X_{\rho} \quad (147)$$

12. Explicit computation of terms related to the mappings

The mapping of the z -plane onto the ζ -plane, mentioned in Section 2, is performed according to the general scheme exposed in [7]. In the z -plane, the 'hinge-points' are denoted by $h_{1,1}$ ($l=1$ through J). In addition, $h_{J+1,1}$ and $h_{J+2,1}$ are the affixes of the lower and upper intersection of the cross-sectional contour with the y -axis.

Let

$$z_1 = z \quad (148)$$

and a sequence of J mappings be used, each defined by the equation:

$$\frac{z_{j+1}^{-\delta_j \alpha_j}}{z_{j+1}^{+\delta_j \alpha_j}} = \left\{ \frac{z_j - h_{jj}}{z_j + h_{jj}^*} \right\}^{\delta_j} \quad (j=1, 2, \dots, J) \quad (149)$$

or its inverse:

$$\frac{z_j - h_{jj}}{z_j + h_{jj}^*} = \left\{ \frac{z_{j+1}^{-\delta_j \alpha_j}}{z_{j+1}^{+\delta_j \alpha_j}} \right\}^{1/\delta_j} \quad (150)$$

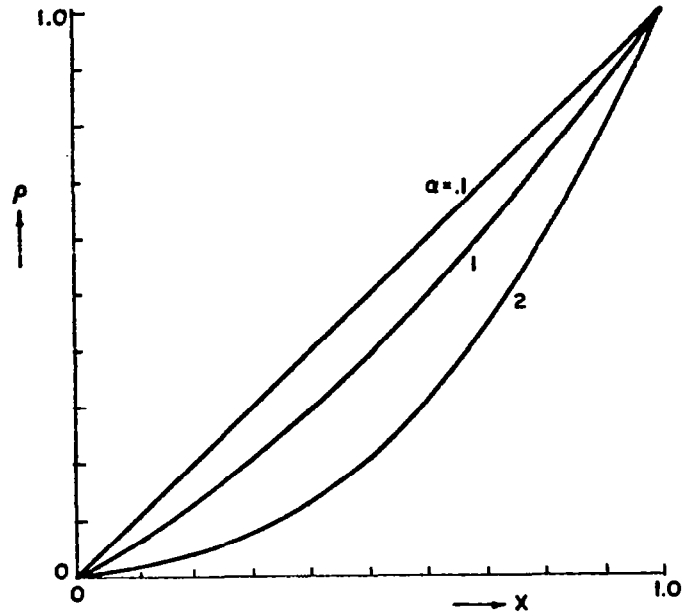


Fig. 1

where

$$h_{jj} = a_j + i \beta_j \quad (151)$$

The mappings are automatically performed in order of increasing δ_j .

With

$$\Sigma = \frac{1}{2}(h_{J+1,J+1} + h_{J+2,J+1}) \quad (152)$$

the ζ -plane is defined as

$$\zeta = z_{J+1} - \Sigma \quad (153)$$

To obtain the derivatives used in the computation of the flow field, the following definitions are used:

$$k_1 = (h_{jj} - z_j) / \alpha_j$$

Explicit computation of terms related to the mappings

$$\begin{aligned}
 k_2 &= z_{j+1}^2 - \delta_j^2 \alpha_j^2 \\
 k_3 &= -\alpha_j k_1 \\
 k_4 &= z_j + h_{jj}^* \\
 k_5 &= \log(k_3/k_4) \\
 k_6 &= \dot{\alpha}_j \\
 k_7 &= \dot{z}_j - \dot{h}_{jj} \\
 k_8 &= z_j - i\beta_j \\
 k_9 &= \dot{z}_j - i\dot{\beta}_j \\
 k_{10} &= \alpha_j \delta_j (\alpha_j \dot{\delta}_j + \dot{\alpha}_j \delta_j) \\
 k_{11} &= 1/(k_3 k_4)
 \end{aligned} \tag{154}$$

where dots mean partial differentiations with respect to t at constant x and y (that is, at constant z). We also define

$$g_j = \frac{dz_{j+1}}{dz_j} = k_2 k_{11} \tag{155}$$

and we note that

$$\frac{\partial z_{j+1}}{\partial h_{jj}} \dot{h}_{jj} + \frac{\partial z_{j+1}}{\partial h_{jj}^*} \dot{h}_{jj}^* = g_j (k_1 k_6 - \dot{h}_{jj}) \tag{156}$$

Therefore,

$$z_{j+1} = g_j (k_7 + k_1 k_6) + [z_{j+1} k_{10} / \alpha_j \delta_j + \frac{1}{2} k_2 k_5 \dot{\delta}_j] / \alpha_j \delta_j \tag{157}$$

and

$$\dot{\zeta} = \dot{z}_{j+1} - \frac{1}{2} (\dot{h}_{j+1, j+1} + \dot{h}_{j+2, j+1}) = \dot{z}_{j+1} - \dot{\Sigma} \tag{158}$$

Explicit computation of terms related to the mappings

The t-derivatives of the h_{11} can be obtained as particular cases of (157), with $h_{1,j+1}$, h_{1j} in lieu of z_{j+1} , z_j respectively. In particular, if $l=j$, $h_{j,j+1}=\delta_j \alpha_j$, as evident from (189), and $h_{j,j+1}=\alpha_j \delta_j k_{10}$.

The functions g , ϕ , f and ψ are determined at each grid point as follows:

$$g = \frac{d\zeta}{dz} = \frac{dz_{J+1}}{dz_1} = \prod_{j=1}^J g_j \quad (159)$$

$$\phi = \frac{\zeta}{g} \frac{d \log g}{dz} = \frac{\zeta}{g} \sum_{j=1}^J \frac{d \log g_j}{dz} = \frac{\zeta}{g} \sum_{j=1}^J \left[\frac{d \log g_j}{dz_j} \prod_{l=0}^{j-1} g_l \right] \quad (160)$$

$$= \frac{2\zeta}{g} \sum_{j=1}^J \frac{z_{j+1}^{-k_8}}{k_2} \prod_{l=0}^j g_l$$

with $g_0=1$,

$$f = \frac{1}{\zeta} \frac{\partial \zeta}{\partial t} = \frac{1}{\zeta} (\dot{z}_{J+1} - \dot{\Sigma}) \quad (161)$$

$$\psi = \frac{\partial \log g}{\partial t} = \sum_{j=1}^J \frac{\dot{g}_j}{g_j} \quad (162)$$

$$= 2 \sum_{(j=1)}^J [(\dot{z}_{j+1} z_{j+1}^{-k_{10}})/k_2 - (k_8 k_9^{-k_6} \alpha_j) k_{11}]$$

At every new cross-section, the geometry defines the values of h_{11} , h_{1j} ($l=1$ through $J+2$) as well as of δ_j , δ_j ($j=1$ through J). According to the procedure explained in [7], the mappings are performed in order of increasing δ_j . First, the values of $h_{1,j+1}$ ($j=1$ through J) are found by repeated applications of the mapping routine, which also provides the values of $\partial h_{1,j+1}/\partial h_{1j}$. Then, Σ is obtained from (152). Repeated applications of (157) allow all the values of h_{1j} to be determined. It

is possible, thus, to evaluate \dot{z} as well.

Grid points on the contour of the body are determined next. For them, the value of θ (that is, Y) is assigned and the value of ρ (that is, b) has to be found. Letting aside those simple problems (such as circular or elliptic cones and cambered wings as defined in this Report) where the body contour can be mapped on a circle with a known radius, b , the task can be performed in two different ways. The first seems to be more direct and, consequently, less time consuming, and it proceeds as follows.

Given a value of Y , a value of b is guessed. All the mappings are executed in reverse order until a value of z is found. Using its x , the geometry subroutine is called to generate the corresponding value of y . Then, the modulus of z and the modulus of $x+iy$ are compared and a trial-and-error procedure is started in order to get coincidence of the two moduli.

The procedure, if working at all, works very fast; in fact, the first guess for b can be taken from the final result of the preceding point and it must be very close to the correct value, since the body contour in the ζ -plane is almost circular. Unfortunately, certain geometries require the use of trigonometric functions and square roots in order to get y , once x is given. In the trial-and-error procedure, values of x which produce, for example, negative radicands or sines greater than 1 may appear. A typical case is shown in Fig. 2 where the abscissa of point z_1 is able to provide a body point, z'_1 but the abscissa of point z_2 cannot generate any body point. Round-off errors which vary from one computer to another compound the difficulty. Constructing a procedure which takes care of such possibilities and corrects the guesses in such a way that a body point is always definable in the course of the trial-and-error iteration, and which also provides a final value of z with the required accuracy seems to be a rather difficult task. For this reason, the procedure described above was abandoned in favor of the following one, whose fine details seemed to be easier to implement.

Given a value of Y , a value of x is guessed (suitably located between the value of the previous point and the maximum value admissible at a given station). From the geometry

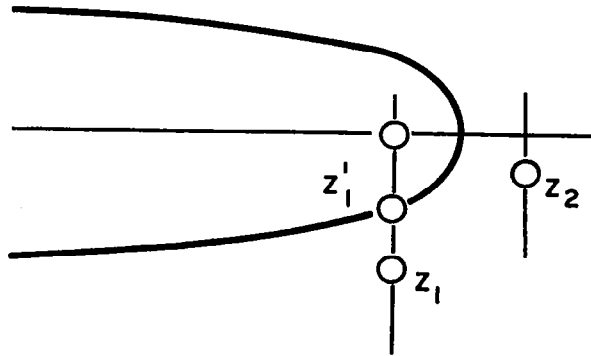


Fig. 2

subroutine, a corresponding value of y can thus be found, with no exceptions. By applying the mapping procedure to $z (=x+iy)$, a value of ζ is found, and its argument is compared with the given Y . the procedure is repeated by increasing or decreasing x until two successive values of the argument of ζ are found which bracket the given Y ; then, a trial-and-error iteration is performed.

Subsequently, g , ϕ , ψ , f , \mathcal{L} and \mathcal{S} are computed and the geometry subroutine is used to determine F_x , F_y and F_t at all body points.

Once b has been determined and c is known from the updating of the shock, all grid points in the ζ -plane can be defined according to (139) and (140). For each of them, the mapping procedure is applied in reverse order until each grid point in the physical plane is obtained. In so doing, we also obtain all values necessary to evaluate g , ϕ , ψ , f , \mathcal{L} and \mathcal{S} .

13. Initial conditions

Three different assumptions can be made with respect to the form of the front end of the vehicle:

Initial conditions

- 1) The body begins with a blunted nose, or
- 2) the body begins with a pointed cone, or
- 3) The body begins with a hollow intake, having a sharp lip contained in a plane normal to the t -axis.

The first assumption is not only realistic since most of the vehicles have a blunt nose, but is also convenient for a safe start of a numerical analysis since the three-dimensional blunt body problem has a solution, regardless of the values of the free-stream Mach number and angle of attack. The analysis described in this Report can be easily started after solving the blunt body problem in a spherical, wind-oriented frame and applying an auxiliary program to advance the solution through a spherical frame whose axis slowly rotates until it coincides with the body axis, t ; simultaneously, the surface supporting the data at every step (which is a cone) slowly tends to become a plane, which will be the initial plane for the present computation.

The second assumption is very convenient if the pointed nose has a circular cross-section and merges smoothly into the rest of the vehicle; in addition, the solution is accurate in the vicinity of the nose only if the angle of attack is zero. If the angle of attack is different from zero but less than the semi-aperture of the cone, a reasonable approximation can still be obtained in the vicinity of the apex. The numerical results, instead, can be grossly inaccurate if the angle of attack is larger than the semi-aperture of the cone.

The assumption of a hollow intake in lieu of a pointed or blunted nose provides a speedy way of initiating the supersonic shock layer about the vehicle by surrounding the sharp rim of the intake with a locally two-dimensional attached shock; of course, an attached shock solution may not exist, and this limits the usability of the device, particularly for very low Mach numbers and high angles of attack.

In the next two Sections, details will be given about the way the second and third assumptions are implemented.

14. Pointed circular cone

We assume that the trace of the shock on a plane, normal to the axis of the cone, is an ellipse if the angle of attack, α , is different from zero. Obviously, the trace of the shock is circular if $\alpha=0$. We consider such a plane as tangent to the unit sphere, whose center is the apex of the cone, and also assume that, within the shock layer, θ is practically equal to $\tan \theta$ (here, θ is the azimuthal angle in a spherical frame, r, θ, ϕ). Therefore in Fig. 3, where the plane is represented, θ is equal to the distance between the point to which it belongs and the origin, O , which is the trace of the axis of the cone. In the same figure, V is the trace of the vector, parallel to \vec{V}_∞ , through the apex of the cone, E is the center of the ellipse representing the shock, δ_1 and δ_2 are the angles between shock and body in the leeward and windward side respectively, A and B are the semi-axes of the ellipse, ϵ is the angle between shock and body on the x -axis, and b is the semi-angle of the cone. Note that

$$\epsilon = A (1 - C^2/B^2)^{1/2} - b \quad (163)$$

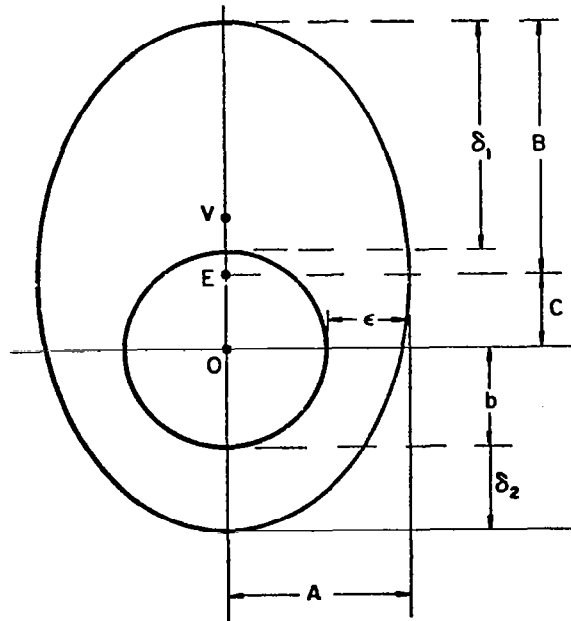


Fig. 3

Pointed circular cone

At zero angle of attack, the conical flow is governed by the equations:

$$du/d\theta = v \quad (164)$$

$$dv/d\theta = -u + (u+v \cotan\theta)/(v^2/a^2-1) \quad (165)$$

Here, the three velocity components in the spherical frame are u, v , and w , respectively and a is the speed of sound. If $\alpha=0$, the problem is solved by assuming a value for the shock angle, δ_0 , getting u, v and a behind the shock from the Rankine-Hugoniot conditions, and integrating (164) and (165) for decreasing values of θ until v equals zero. Since such a condition should occur when $\theta = b$ (that is, on the cone surface) and that hardly happens for the assumed value of δ_0 , the latter is corrected and the procedure repeated until the condition is satisfied. To assure accuracy, I generally divide the shock layer into 300 intervals, which allows a simple method, such as Euler's, to be used.

If the angle of attack is not zero, (165) must be replaced by

$$v_\theta = -u + (u+v \cotan\theta + w_\phi/\sin\theta)/(v^2/a^2-1) \quad (166)$$

The same iteration technique is used to integrate (164) and (166), assuming that w_ϕ is constant across the shock layer between M and N and between P and Q. In addition, we postulate that

$$(\epsilon+\delta_2)/2 = \delta_0 \quad (167)$$

regardless of the Mach number and of the angle of attack. From (163) and (167) A may be expressed as a function of B and C,

$$A = \frac{2\delta_0 - \delta_2 + b}{(1-C^2/B^2)^{1/2}} \quad (168)$$

Consequently, only two parameters, B and C, are left to define the ellipse. They are related to δ_1 and δ_2 through the equations,

Pointed circular cone

$$B = b + (\delta_1 + \delta_2)/2 \quad (169)$$

$$C = (\delta_1 - \delta_2)/2$$

To find approximate initial conditions for the conical shock layer at an angle of attack, we call s the value of θ at the shock. From the equation of the ellipse, it follows that

$$s = \frac{C \cos \phi + B[(B^2 - C^2)/A^2 \sin^2 \phi + \cos^2 \phi]^{1/2}}{(B/A)^2 \sin^2 \phi + \cos^2 \phi} \quad (170)$$

and

$$s_{\phi\phi} = s \left(1 - \frac{B}{A^2} s\right) \quad (171)$$

at the symmetry plane. From the Rankine-Hugoniot equations,

$$w_\phi = \tilde{u} s_{\phi\phi} / \sin s - V_\phi \quad (172)$$

where \tilde{u} is the component of the velocity behind the shock along the normal to the shock wave, pointing inwards, and V_ϕ is the derivative with respect to ϕ of the component of the velocity along the tangent to the shock wave in the plane of Fig. 3. The component of the velocity in front of the shock along the normal is

$$V_\infty \sin(s \pm \alpha) \quad (173)$$

where the upper sign holds for point Q and the lower for point N. From (173), \tilde{u} is obtained through the Rankine-Hugoniot equations. From the same equations,

$$V_\phi = V_\infty [s_{\phi\phi} \cos \alpha \pm (s_{\phi\phi} \cotan s - 1) \sin \alpha] \quad (174)$$

We have now the equations which are necessary and sufficient to determine B and C. From a computational point of view, an iteration procedure is convenient. The value of C is initially assumed as zero and a value of B is guessed; A is computed from (168) and the corresponding values of w_ϕ on the windward and leeward side are evaluated. Then the equations (164) and (166) are

Pointed circular cone

integrated between N and M and between Q and P. Two new values of δ_1 and δ_2 result, from which two new values of B and C are obtained, and the procedure is repeated until convergence is achieved.

Once the shock shape has been determined, the Rankine-Hugoniot conditions provide all the physical parameters behind the shock at any point. The pressure on the body is linearly interpolated between windward and leeward side; σ equals the tangent to the cone angle; S is taken equal to its windward value everywhere except at the leeward point. The cross-flow velocity on the body is defined by a parabola:

$$w = b\phi + c\phi^2 + d\phi^3 \quad (175)$$

where

$$b = w_{\phi(lee)}, \quad d = (w_{\phi(lee)} + w_{\phi(wind)})/\pi^2, \quad c = -(w_{\phi(lee)}/\pi + d\pi)$$

From P and S, the temperature is determined and then q^2 . Finally,

$$\eta = wd/(q^2 - w^2)^{1/2} \quad (176)$$

The values of P, S, σ and η are linearly interpolated between shock and body on each meridional plane except the windward and leeward plane, where they are obtained from the converged solution above. Such a linear interpolation between shock and body is rather simplistic and it is a far cry from the real solution to the conical flow past a circular cone at an angle of attack. More parametric studies of the latter could provide a better set of initial conditions. The current procedure surely shows its age [3].

15. Attached shock around a hollow intake

If we assume that the body begins with a hollow intake of a prescribed cross section, whose lip produces an attached shock, the latter and the physical parameters behind it can be evaluated

as follows.

Let \hat{A} be the unit vector, normal to the lip, in the first $t=\text{constant}$ plane, \hat{N} the unit vector, normal to the body surface in the same plane, and \hat{n} the unit vector, normal to the shock produced by the lip, again in the same plane. Note that \hat{A} is contained in the $t=\text{constant}$ plane, but \hat{N} and \hat{n} are not.

For \hat{N} , (30) and (31) hold. Therefore,

$$H_1 = 1/v_1, \quad H_2 = -(b_Y/b)H_1 \quad (177)$$

with

$$v_1 = [1 + (b_Y/b)^2]^{1/2} \quad (178)$$

Since the shock is attached to the lip, the latter is initially the cross-section of the shock itself; therefore, the unit vector normal to the shock in the $t=\text{constant}$ plane coincides with \hat{A} . We may write:

$$\hat{n} = n_O \hat{A} + n_J \hat{k} \quad (179)$$

and note that

$$n_O^2 + n_J^2 = 1 \quad (180)$$

Since

$$n_1 = n_O H_1, \quad n_2 = n_O H_2 \quad (181)$$

n_O and n_J are the only two quantities to be evaluated, in order to determine the initial direction of \hat{n} .

The free stream velocity is

$$\vec{V}_\infty = u_\infty \hat{i} + v_\infty \hat{j} + w_\infty \hat{k} = \tilde{u}_\infty \hat{n} + \vec{v}_\infty^* \quad (182)$$

Note that

$$u_\infty = V_\infty \sin \alpha, \quad v_\infty = V_\infty \cos \alpha, \quad w_\infty = V_\infty \cos \alpha \quad (183)$$

according to (103) and (104). Obviously,

$$\begin{aligned}\tilde{u}_\infty = \vec{V}_\infty \cdot \hat{n} &= u_\infty n_1 + v_\infty n_2 + w_\infty n_3 = n_0 (u_\infty H_1 + v_\infty H_2) + w_\infty n_3 \\ &= n_0 \vec{V}_\infty \cdot \vec{A} + w_\infty n_3\end{aligned}\quad (184)$$

and

$$\vec{V}_\infty^* = \vec{V}_\infty - \tilde{u}_\infty \hat{n} = (u_\infty - \tilde{u}_\infty n_0 H_1) \hat{i} + (v_\infty - \tilde{u}_\infty n_0 H_2) \hat{j} + (w_\infty - \tilde{u}_\infty n_3) \hat{k} \quad (185)$$

The velocity behind the shock is:

$$\vec{V} = u\hat{i} + v\hat{j} + w\hat{k} = \tilde{u}\hat{n} + \vec{V}_\infty^* \quad (186)$$

with

$$\tilde{u} = \frac{\gamma-1}{\gamma+1} \tilde{u}_\infty + \frac{2\gamma}{\gamma+1} \frac{1}{\tilde{u}_\infty} \quad (187)$$

so that

$$\Delta \tilde{u} = \tilde{u} - \tilde{u}_\infty = \frac{2}{\gamma+1} (\gamma \tilde{u}_\infty - \tilde{u}_\infty) \quad (188)$$

The velocity behind the shock must be parallel to the body:

$$\vec{V} \cdot \vec{N} = 0 \quad (189)$$

From (189), (187), (185) and (188) we obtain the condition:

$$[u_\infty + \Delta \tilde{u} \cdot n_0 H_1] N_1 + [v_\infty + \Delta \tilde{u} \cdot n_0 H_2] N_2 + [w_\infty + \Delta \tilde{u} \cdot n_3] N_3 = 0 \quad (190)$$

The equation above, by virtue of (180), contains the only unknown, n_3 . By introducing the notations:

$$\begin{aligned}V_{\infty H} &= \vec{V}_\infty \cdot \vec{A}, \quad V_{\infty N} = \vec{V}_\infty \cdot \vec{N}, \quad N_H = \vec{N} \cdot \vec{A}, \quad A^2 = V_{\infty H}^2 \\ B &= V_{\infty H}^2 - w_\infty^2, \quad C = 2w_\infty V_{\infty H} N_H, \quad D = AN_H + V_{\infty N} V_{\infty H} \frac{\gamma+1}{2} \\ E &= AN_3 - C + w_\infty V_{\infty N} \frac{\gamma+1}{2}, \quad F = BN_H - 2w_\infty V_{\infty H} N_3, \quad G = BN_3 + C\end{aligned}$$

(190) can be written in the form:

$$(1-n_3^2)(D+Fn_3)^2=(E+Gn_3^2)^2 \quad (191)$$

or

$$n_3^6+bn_3^4+cn_3^2+d=0 \quad (192)$$

where

$$b = \Delta[2(DF+EG)-F^2], \quad c = \Delta[D(D-2F)+E^2], \quad d = -\Delta D^2$$

$$\Delta = 1/(F^2+G^2) \quad (193)$$

Note that (192) has the same form as (150a) in [10] and a similar physical meaning. If there is only one real root for n_3^2 , no attached shock is possible (the root corresponds to a value on the outgoing branch of the shock polar, Fig. 4). If there are three real roots for n_3^2 , the intermediate one corresponds to the physi-

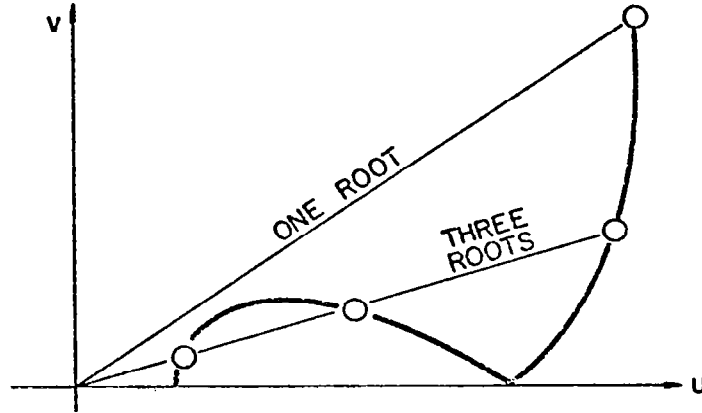


Fig. 4

cal condition of a weak, attached shock (point B in Fig. 4). The computational program chooses the intermediate value of n_3^2 and then computes n_o from (180), \tilde{u}_∞ from (184), $\Delta\tilde{u}$ from (18d); it follows that

$$M_{n_\infty}^2 = \tilde{u}_\infty^2/\gamma \quad (194)$$

and, behind the shock,

Attached shock around a hollow intake

$$P = \ln \left(\gamma M_{n\infty}^2 - \frac{\gamma-1}{2} \right) / \frac{\gamma+1}{2}$$

$$S = P + \gamma \ln (\tilde{u}/\tilde{u}_\infty) \quad (195)$$

$$u = \Delta \tilde{u} n_1 + u_\infty, \quad v = \Delta \tilde{u} n_2 + v_\infty, \quad w = \Delta \tilde{u} n_3 + w_\infty$$

From (33) and (34), written with n in lieu of N , we see that

$$c_T = c[f_1 - (c_Y/c)f_2] - Gd = [c(n_1 f_1 + n_2 f_2) - G n_3]/n_1 \quad (196)$$

A very small step, Δt , may be taken, and a new shock shape assumed in the ζ -plane, given by

$$c = b + c_T \Delta t \quad (197)$$

where c_T is defined by (196). Then, values of P , S , w , $\sigma = u/w$, $\eta = v/w$ as obtained in (195) are uniformly distributed between shock and body at the new station, for every value of Y . To speed up the subsequent calculation, only four points for every value of Y are considered, one on the body, one on the shock and two in between. A slight correction may be needed, in order to make σ at the body compatible with the new body geometry at $t + \Delta t$. We leave η unchanged and, after computing new values of N_1 , N_2 and N_3 according to (30), define

$$\sigma = - (N_3 + \eta N_2) / N_1 \quad (198)$$

according to (189). The initial values of \tilde{v} at the body are then determined by using (100).

16. Preliminary tests. Circular cones at no incidence

In what follows, detailed descriptions of the geometry subroutines for each body geometry are given. For each body geometry, the computations performed are reported with pertinent comments.

A preliminary set of tests was performed on circular cones at no incidence. Any cross-section of a circular cone is defined by

$$x^2 + y^2 = a^2 \quad (199)$$

with

$$a = At \quad , \quad a_t = A \quad , \quad a_{tt} = 0 \quad (200)$$

Circular cones are used primarily to test the logic and the coding of the mapping subroutines, and to get an idea of the accuracy and reliability of the integration technique.

The latter is the object of a first series of tests. The free-stream Mach number is set equal to 6, the angle of attack equal to 0 and the cone angle equal to 30° ($A = .57735$). In Run 1, the pointed nose model is used, and the computation starts at $t=1$ with 12 radial intervals and 2 circumferential intervals (of course, at no incidence, all meridional planes should contain identical results and all Y -derivatives should vanish). No stretching is used. One mapping function is used, with $h_{11}=a/2$ and $\delta=1$. The resulting mapping is an identity. Runs 2, 3, and 4 are similar, but the X -coordinate is stretched, with $\alpha=0.5, 1$ and 2 respectively. In all four cases, the calculation is carried on for a large number of steps (100 for the first three cases and 200 for the fourth) and the differences between the final and the initial values of pressure (multiplied by 10,000) are reported in Fig. 5. As the figure shows, the stability and accuracy of the computational technique is indeed remarkable (at least, when only one space-like dimension is involved).

Preliminary tests. Circular cones at no incidence

The errors are almost in round-off error order range. It must be noted that Fig. 5 is intended to give an appreciation for the order of magnitude of the errors; from step to step, they oscillate in a wavelike form between body and shock, but they always

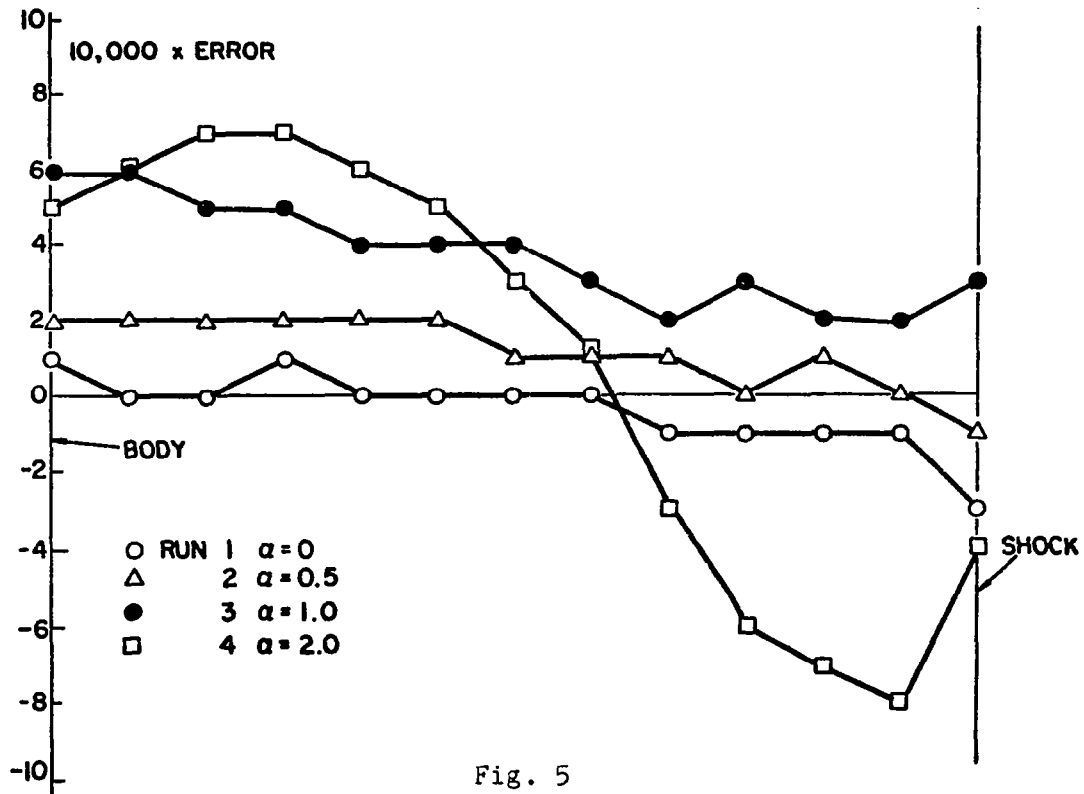


Fig. 5

remain confined to the ranges shown in the figure.

These results also show that one can use rather strong stretching devices with confidence. Note, in Fig. 6, the distribution of nodal points between body and shock in the four cases, and the very strong accumulation of nodes near the body resulting from the use of a stretching parameter equal to 2.

A second series of runs was made to test the mapping subroutines, using the same physical and geometrical inputs as in the first series. In the first run, two mapping functions are used in a sequence, the first with $h_{11}=a/2$ and the second with $h_{21}=(1+i)h_{11}$. For both mappings, $\delta_1=\delta_2=1$; therefore, both map-

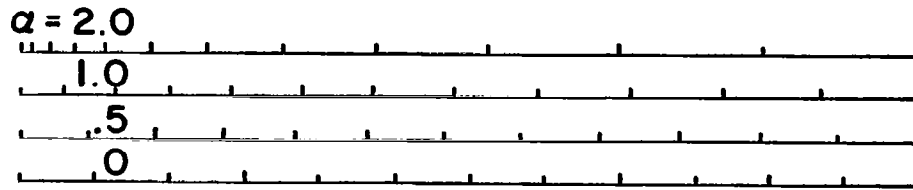


Fig. 6

pings are identities.

In the second run, the effect of non-identical mappings is tested. Two mapping functions are used, with their hinge-points on the same location ($h_{11}=h_{21}=a/2$). The values of δ are: $\delta_1=1/2$, $\delta_2=2$. Therefore, the first mapping transforms the circle into an ellipse, and the second transforms the ellipse back again into the original circle.

In the third run, the effect of non-identical mappings and of variable values of δ is tested. Here, $\delta_1=.2+6(t-.2)$, $\delta_2=1/\delta_1$.

A fourth run was made to test whether the results were affected by making use of the symmetry of the flow with respect to the x-axis and, consequently, computing only in one quadrant of the z-plane.

In all of the runs above the results were identical to the ones obtained in the first run, to within 4 significant digits.

17. Circular cones at an angle of attack

Next, flows past circular cones at an angle of attack were computed. For all of them, one mapping function is used as in Run 1, with $h_{11}=a/2$ and $\delta=1$. The first case considered has a

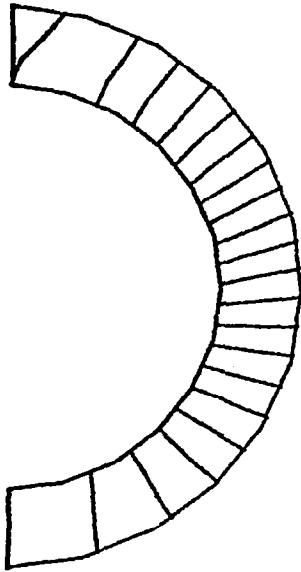
10° cone in a free stream Mach number of $M=2$ at an angle of attack of 5° . The cone starts at $t = 1$ with a hollow intake; the initial mesh has 3 radial and 12 circumferential intervals; the number of radial intervals is doubled at $t=1.5$ and again at $t=2$. The stretching parameter is equal to 1. The computation is continued for 500 steps, till $t = 1880$. At that step, the maximum value of c_{tt} is less than 10^{-4} and we can consider that the flow is entirely conical. A sequence of isobars plots for this computation (Run 11) is shown in Fig. 7.

Another calculation for the same geometry, Mach number and angle of attack was performed using a stretching parameter equal to 1.5; the radial intervals, initially in number of 3, were doubled at $t=1.5$ and $t=2$; the circumferential intervals, initially in number of 12, were doubled at $t=2.5$. A sequence of isobar plots for this case (Run 152) is shown in Fig. 8. At step 500 ($t=34.4$), c_{tt} does not exceed 0.0002. In Fig. 9 the circumferential pressure distribution on the cone at the final step of both runs is compared with the pressure distribution predicted by Jones [9]. In Fig. 10 a similar comparison is made for the radial pressure distribution at the windward and leeward side, as well as at $\theta=90^\circ$. The agreement is very good.

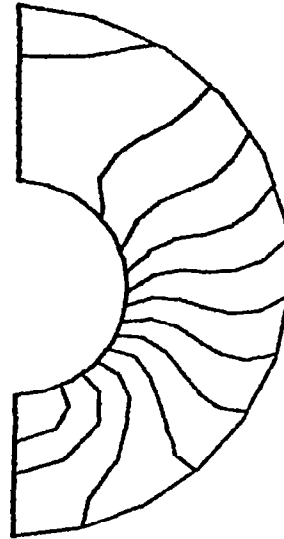
The evolution shown in Figs. 7 and 8 deserves a careful examination, since it shows how the flow, which is initially locally two-dimensional and practically independent on the radius (as it should be in the proximity of the intake lip) gets twisted into a complicated conical pattern. In the first phase of the evolution, a pressure 'valley' and a pressure 'hill' appear; the former near the shock and the latter near the body (Fig. 11); further ahead, the valley disappears and the hill gets stabilized into the asymptotic pattern.

Another shockless flow field is obtained, for $M=2$, about a 5° cone at 10° angle of attack (Run 121). The computational parameters adopted for this case are the same as for Run 152; only the stretching parameter has been set equal to 2. A sequence of isobar plots is shown in Fig. 12. The asymptotic pressure coefficient, as computed, is compared in Fig. 13 with values obtained by other Authors [11]. Note the formation of a pressure valley on the leeward side of the cone, anticipating the formation of a cross-flow shock, which occurs for higher incidences.

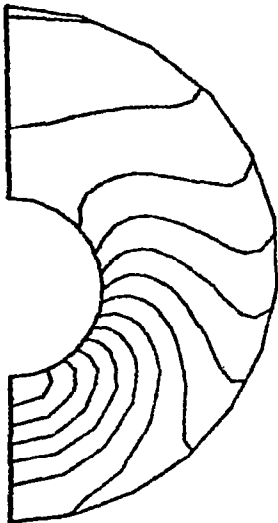
Elliptic cones



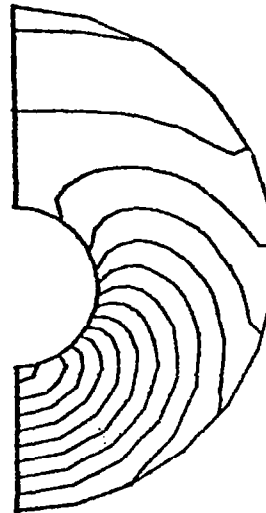
RUN= 11 M= 2.00 K= 25 T= 1.1226
DREF=0.0200 MAX=0.6200 2



RUN= 11 M= 2.00 K= 50 T= 1.8903
DREF=0.0200 MAX=0.4000 2



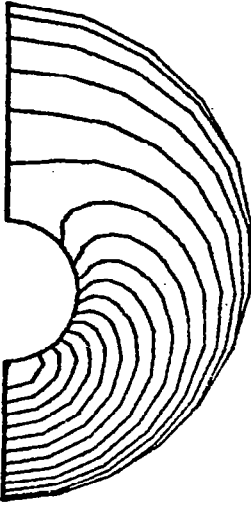
RUN= 11 M= 2.00 K= 75 T= 2.7518
DREF=0.0200 MAX=0.3800 2



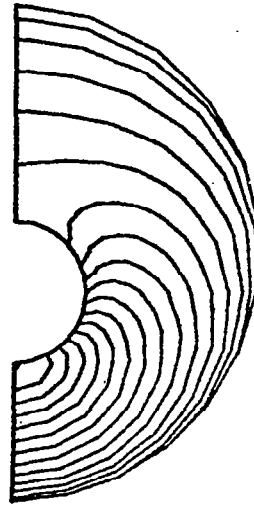
RUN= 11 M= 2.00 K= 100 T= 4.1047
DREF=0.0200 MAX=0.3800 2

Fig. 7(a)

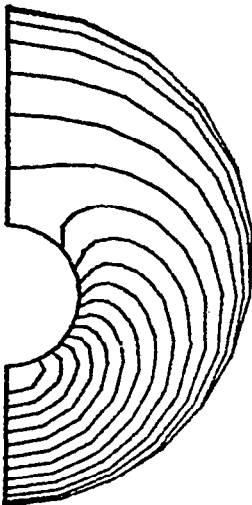
Elliptic cones



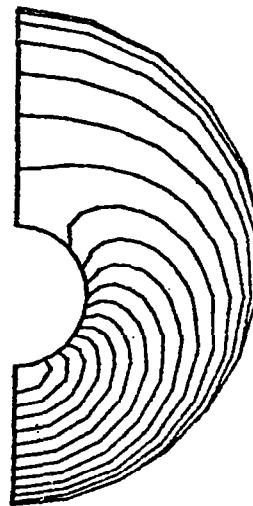
RUN= 11 M= 2.00 K= 250 T= 63.1981
DREF=0.0200 MAX=0.3800 2



RUN= 11 M= 2.00 K= 300 T= 159.3302
DREF=0.0200 MAX=0.3800 2



RUN= 11 M= 2.00 K= 400 T= 879.6572
DREF=0.0200 MAX=0.3600 2



RUN= 11 M= 2.00 K= 500 T=1879.6572
DREF=0.0200 MAX=0.3600 2

Fig. 7(b)

Elliptic cones

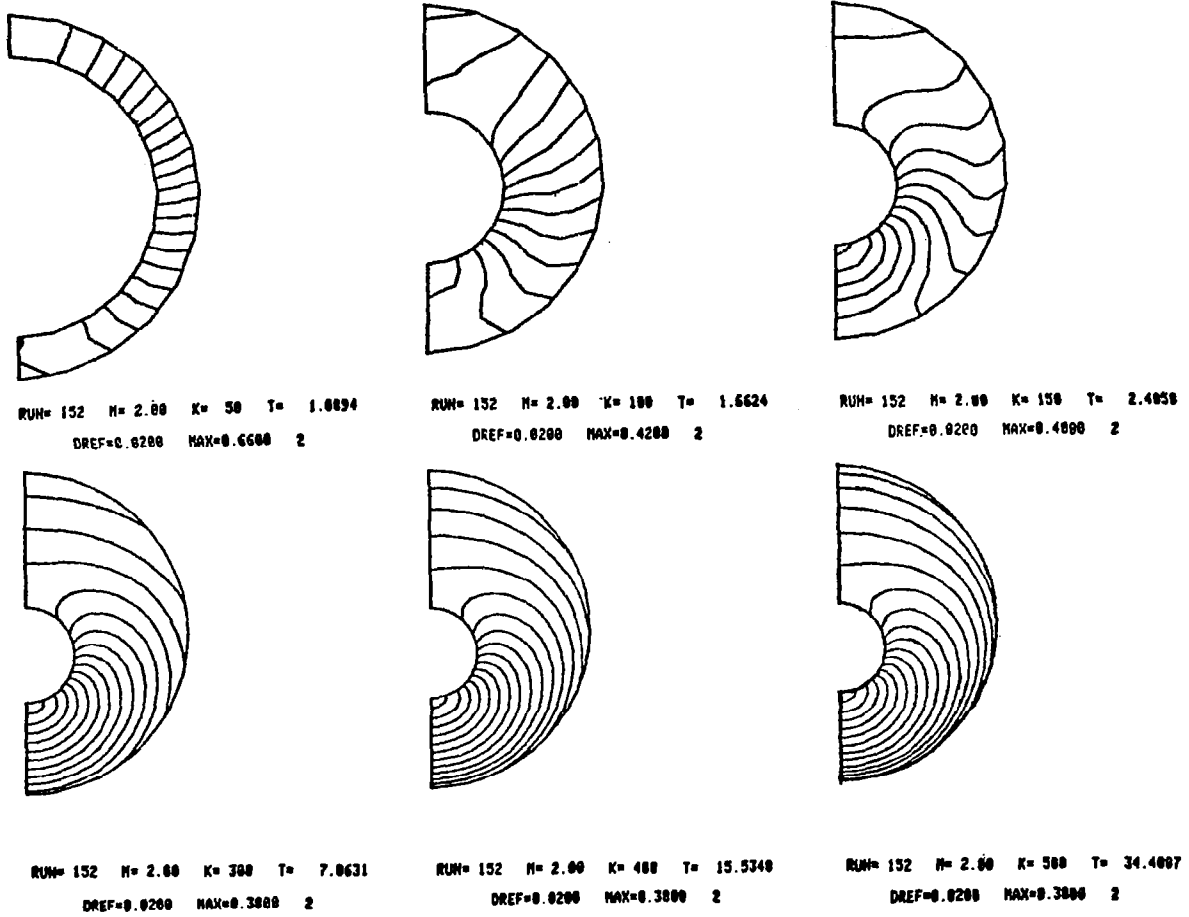


Fig. 8

18. Elliptic cones

Any cross-section of an elliptic cone is defined by

$$\frac{x^2}{a^2} + \frac{y^2}{b^2} = 1 \quad (201)$$

Elliptic cones

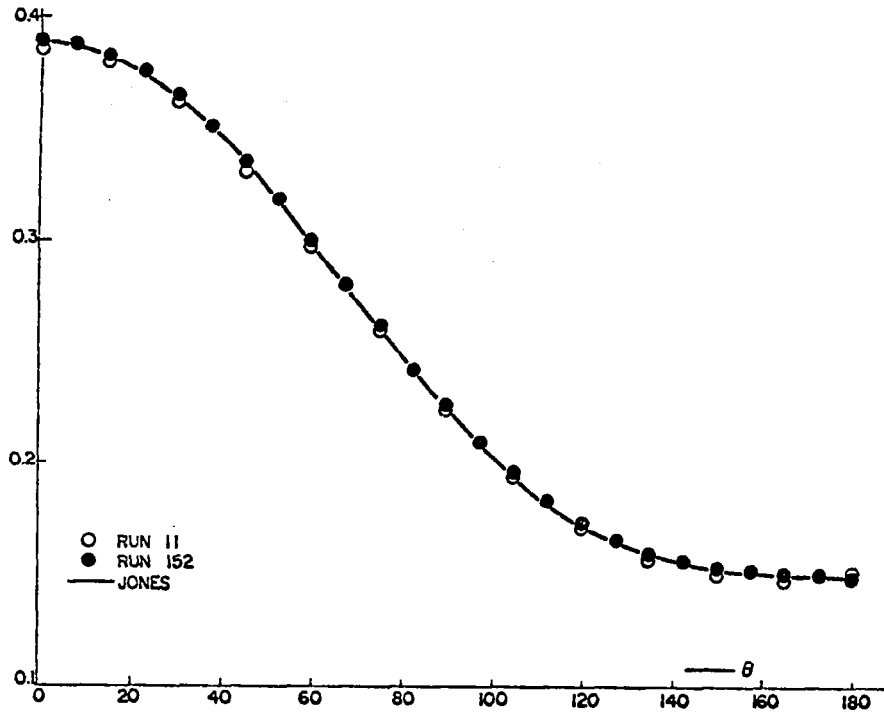


Fig. 9

with

$$\begin{aligned} a &= At \quad , \quad a_t = A \\ b &= Ba \quad , \quad b_t = BA \end{aligned} \quad (202)$$

The derivatives of F , as defined by (35), are

$$F_x = 2x/a^2 \quad , \quad F_y = 2y/b^2 \quad , \quad F_t = -2A/a \quad (203)$$

To obtain a perfect circle as the image of the body in the ζ -plane, one mapping function can be used, with

$$h_{11} = a(1-B^2)^{1/2} \quad , \quad \dot{h}_{11} = A(1-B^2)^{1/2} \quad , \quad \delta_1 = 1/2$$

The other two points of interest are the lower and upper intersection of the body with the $x = 0$ line, viz.

$$h_{21} = -ib \quad , \quad h_{31} = ib$$

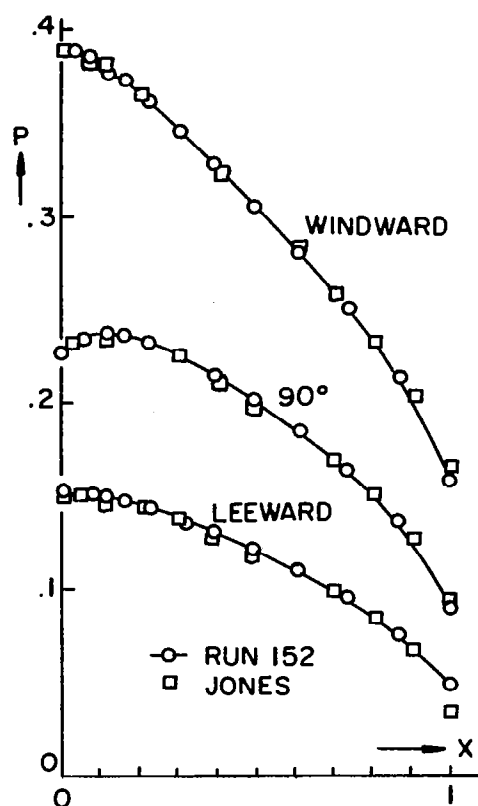


Fig. 10

from which it follows that

$$\dot{h}_{21} = -iAB, \quad \dot{h}_{31} = iAB$$

A computation was performed (Run 16) with $A = 0.6$, $B = 0.5$, $M_\infty = 6$ at an angle of attack equal to 16° . The initial lip is assumed to be at $t=0.2$. The computational grid begins with 3 intervals in the radial direction and 12 intervals circumferentially; the radial intervals are doubled at $t=0.4$ and again at $t=0.6$. The circumferential intervals are doubled at $t=0.6$ only. The stretching parameter, α , is made equal to 1. In Figs. 14 and 15 isobar plots at selected steps are shown. After 1500 computational steps, the station defined by $t=12.37$ is reached and the computation is halted. At this stage, the computational grid appears as in Fig. 16. In Figs. 17 and 18 curves of constant P , S , σ and η are shown. In all these figures we may note an indentation in the outer shock at the leeward symmetry point. Does it indicate a programming error? A careful analysis of outputs of preceding steps led us to the conclusion that slight inaccuracies may result because of insufficient resolution, but that a similar

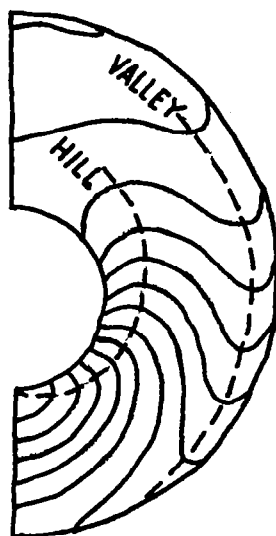
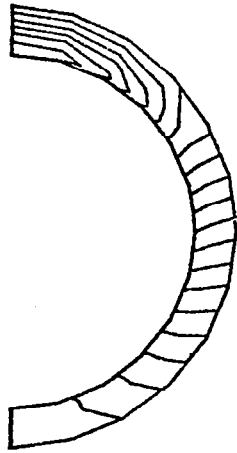


Fig. 11

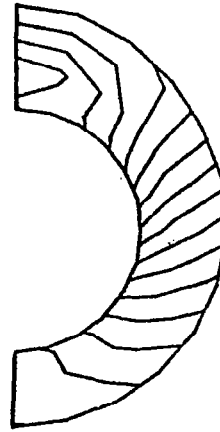
trend is justifiable on physical grounds; the indentation is expected to disappear after a large number of additional computational steps. In other words, the flow is not yet conical on the leeward side after 1500 steps. Let us examine then how the shock shape varies from $t=0.2$ to $t=12.37$ and how the conical flow pattern sets in.

At the beginning, we assume that, at every point on the lip, a shock is formed according to the analysis of Section 14. Such a shock is evidently two-dimensional at each point since no signal from neighboring points on the lip can be transmitted laterally due to the supersonic nature of the flow. Therefore, the initial shock and the consequent distribution of values between shock and body are not conical. The rate of change of the shock in the physical space is controlled by the values of c_t in the mapped plane for every cross-section. We can, thus, analyze the evolution of the distribution of c_t as a function of θ , as t increases. In a conical flow, c_t should be constant in t for every point. In Fig. 19, computed values of c_t are shown at selected steps. Initially, such values are very high near $\theta=0$ where the

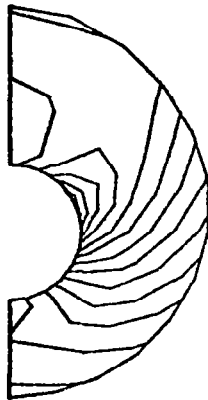
Elliptic cones



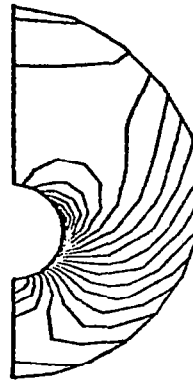
RUN= 121 M= 2.00 K= 50 T= 1.0328
DREF=0.0500 MAX=0.6500 2



RUN= 121 M= 2.00 K= 100 T= 1.101
DREF=0.0500 MAX=0.5500 2



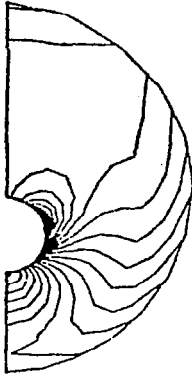
RUN= 121 M= 2.00 K= 150 T= 1.3677
DREF=0.0400 MAX=0.3600 2



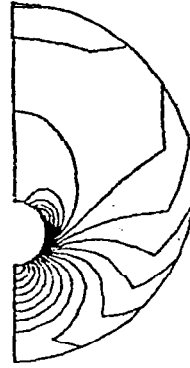
RUN= 121 M= 2.00 K= 200 T= 1.761
DREF=0.0200 MAX=0.3000 2

Fig. 12(a)

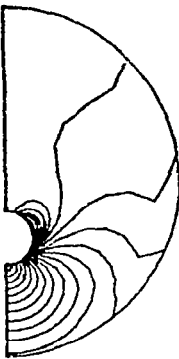
Elliptic cones



RUN= 121 M= 2.00 K= 300 T= 2.4780
DREF=0.0200 MAX=0.3000 2



RUN= 121 M= 2.00 K= 400 T= 3.4152
DREF=0.0200 MAX=0.3000 2



RUN= 121 M= 2.00 K= 600 T= 7.0031
DREF=0.0200 MAX=0.3000 2



RUN= 121 M= 2.00 K= 800 T= 15.0196
DREF=0.0200 MAX=0.3000 2

Fig. 12(b)

Elliptic cones

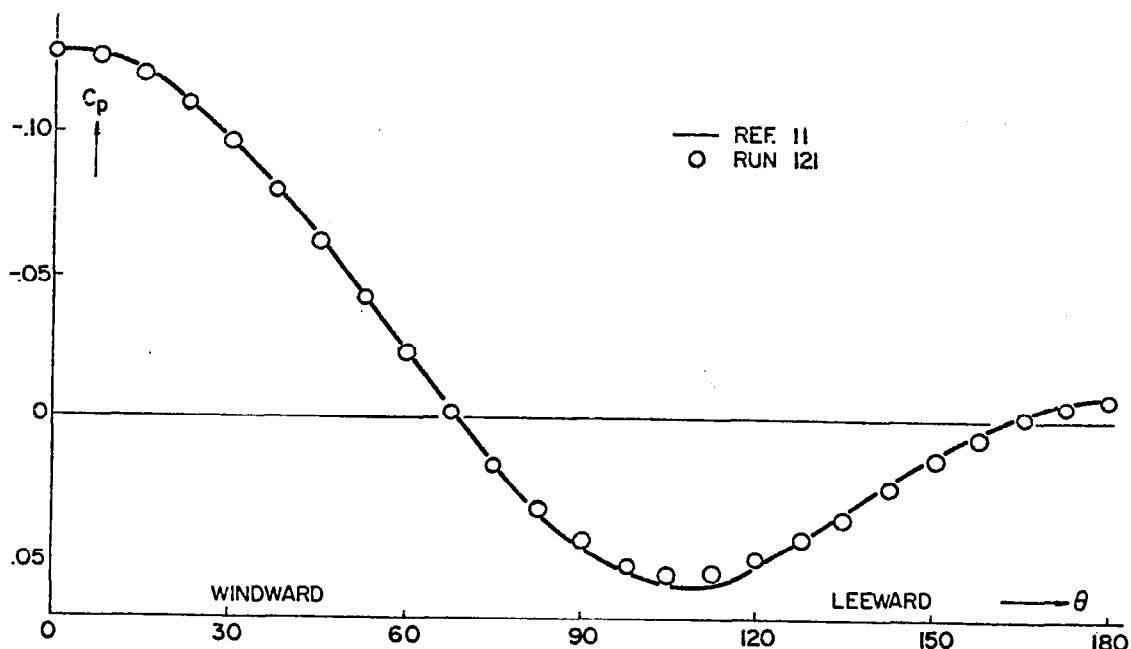
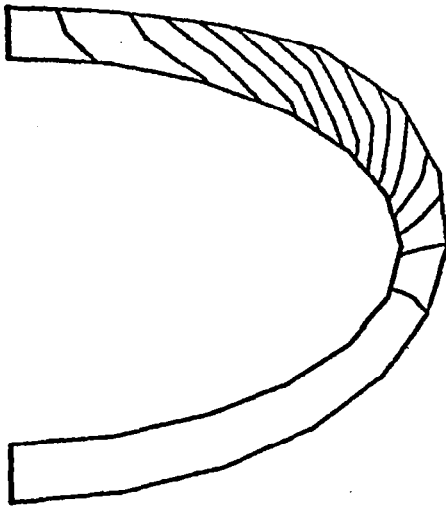


Fig. 13

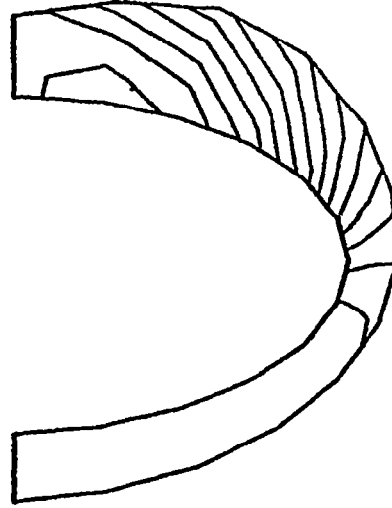
curvature of the cross-section of the body is the highest and, therefore, the deviation of the initial two-dimensional shock from the conical one is also the greatest. The windward side of the flow, however, tends to get stabilized very rapidly, thanks to rather low Mach numbers in the shock layer (of the order of 2). All perturbations tend to be carried towards the leeward side since the velocity vectors are so oriented ($n > 0$). The shock tends to move outwards for values of θ greater than 0, and the point of maximum c_t shifts rapidly towards the leeward symmetry plane. Note, incidentally, the refinement in the curve of c_t which occurs after the number of grid points in the circumferential direction is doubled.

As t increases, we expect the peak in the c_t -distribution to move further towards $\theta = \pi/2$, and eventually reach it. At this stage, however, the locus of the peak is shifted only very slowly; for an observer watching the cone from above, the angle under which the peak approaches the leeward symmetry plane is about 10° ; that is, the numerical perturbation travels along a characteristic. A finer mesh could show a better behavior of the shock

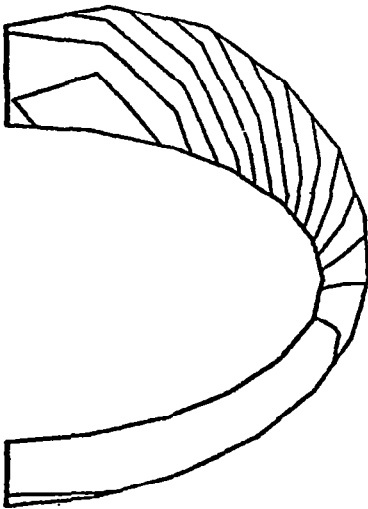
Elliptic cones



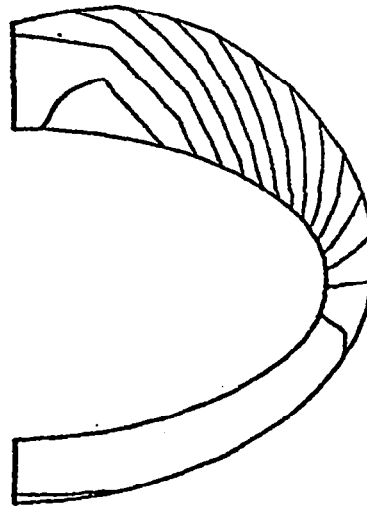
RUN= 16 M= 6.00 K= 100 T= 0.3470
DREF=0.2000 MAX=2.8000 2



RUN= 16 M= 6.00 K= 200 T= 0.7946
DREF=0.2000 MAX=2.8000 2



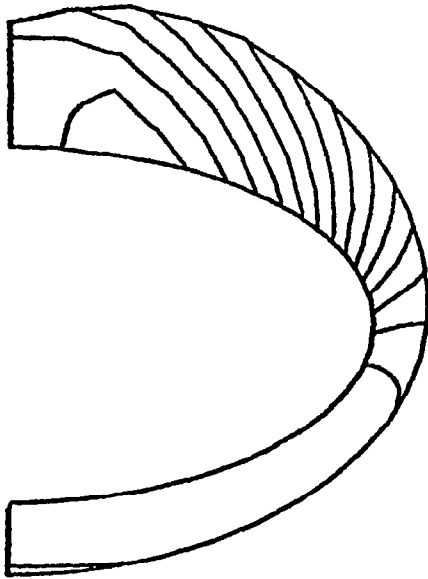
RUN= 16 M= 6.00 K= 300 T= 1.9248
DREF=0.2000 MAX=2.8000 2



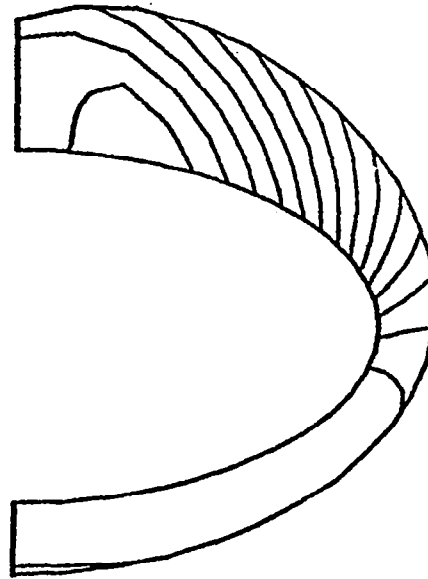
RUN= 16 M= 6.00 K= 400 T= 3.0412
DREF=0.2000 MAX=2.8000 2

Fig. 14

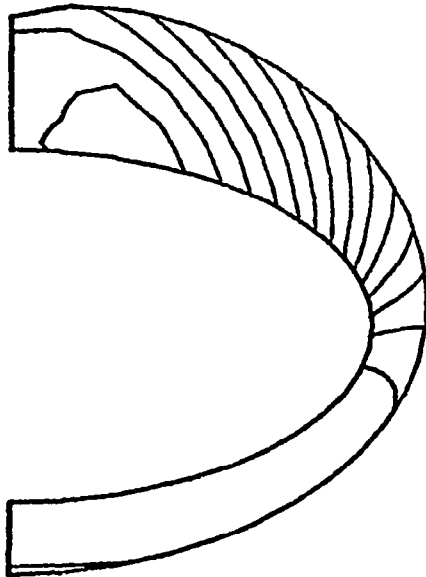
Elliptic cones



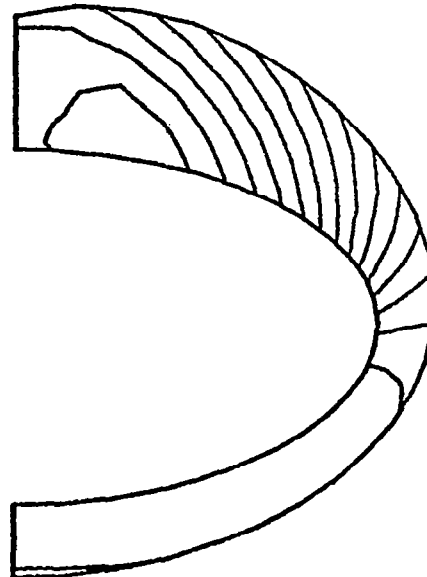
RUN= 16 M= 6.00 K= 500 T= 3.8140
DREF=0.2000 MAX=2.8000 2



RUN= 16 M= 6.00 K= 800 T= 7.6863
DREF=0.2000 MAX=2.8000 2



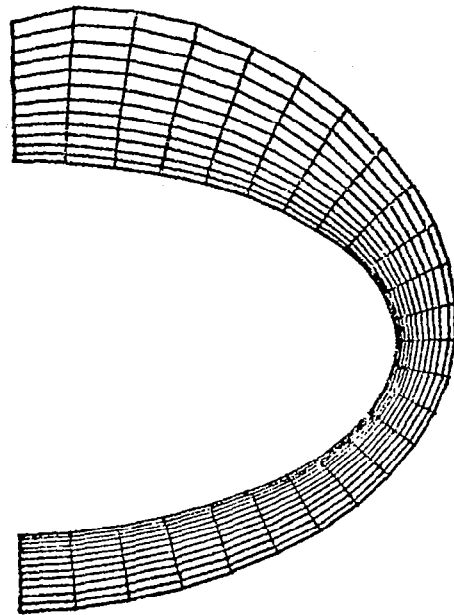
RUN= 16 M= 6.00 K=1100 T= 15.6152
DREF=0.2000 MAX=2.8000 2



RUN= 16 M= 6.00 K=1300 T= 25.1008
DREF=0.2000 MAX=2.8000 2

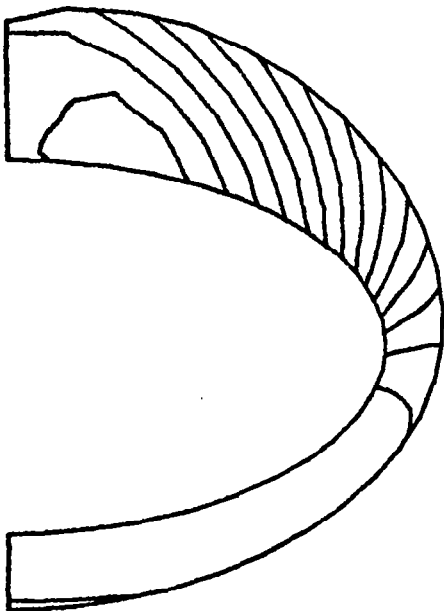
Fig. 15

Elliptic cones



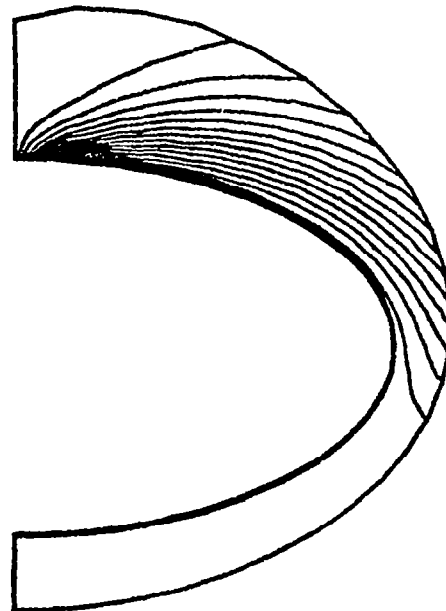
RUN= 16 M= 6.00 K=1501 T= 12.3728

Fig. 16



RUN= 16 M= 6.00 K=1501 T= 12.3728

DREF=0.2000 MAX=2.0000 2



RUN= 16 M= 6.00 K=1501 T= 12.3728

DREF=0.0500 MAX=1.0000% 3

Fig. 17

shape in the vicinity of the leeward symmetry plane, but we do not expect a perfectly convex shape to appear, even after a

Elliptic cones

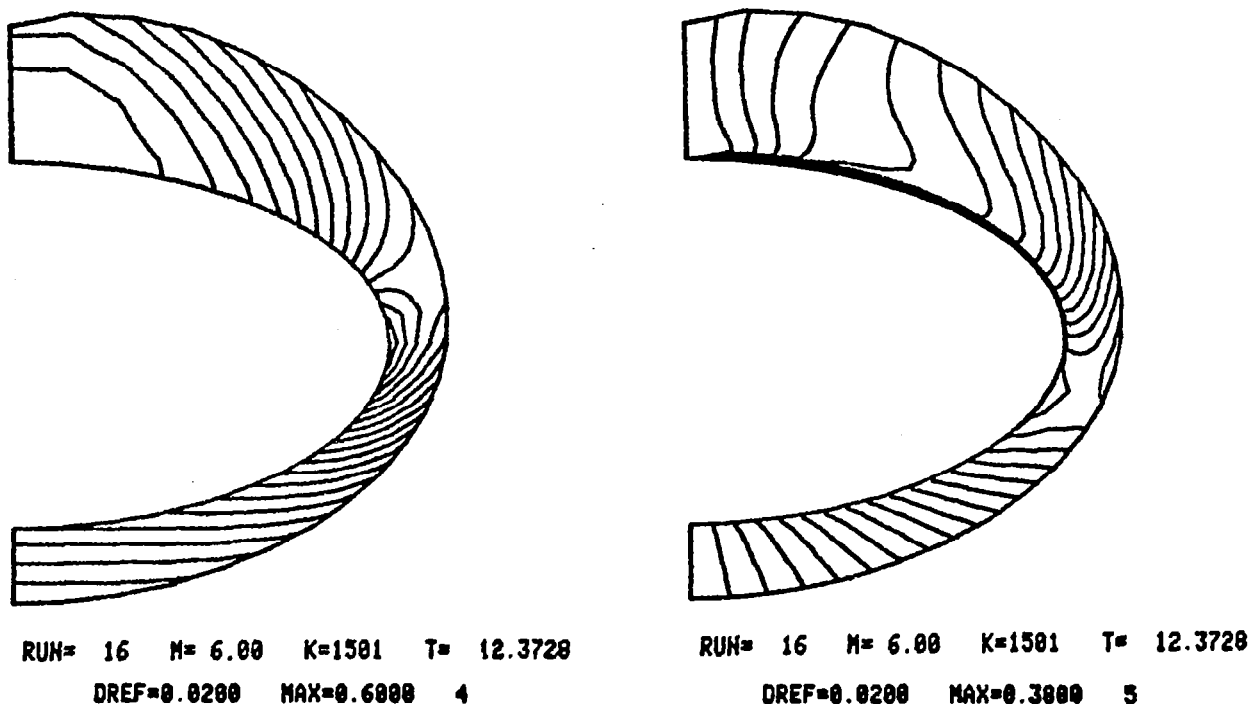


Fig. 18

prohibitive number of additional steps.

Quite reliable results on the same case have been obtained by Pandolfi [17]. We present some comparisons of our results at the last computed step with the latter's in Figs. 20 through 22. The shock shape is compared in Fig. 20 and the pressure distribution in Figs. 21 and 22; Fig. 23 shows the η -distribution along the body. We note some rather large discrepancies in the upper portion of the body or, more precisely, from the conical 'stagnation point' upwards; the stagnation point itself, however, coincides in both calculations. The value of η at the body is, in our case, obtained from (101), which in turn depends on (100), (99) and (98). The latter is a sensitive equation and small changes in its coding may produce large variations in results, for flows such as the present leeward side flow. Pandolfi and myself have commented on this difficulty in a previous paper [5], but this does not imply that his elliptic cone program and the present, general-purpose program are similarly coded! In particular, I believe that Pandolfi did not compute \tilde{v}_y as I do and this is sufficient reason to account for the

Elliptic cones

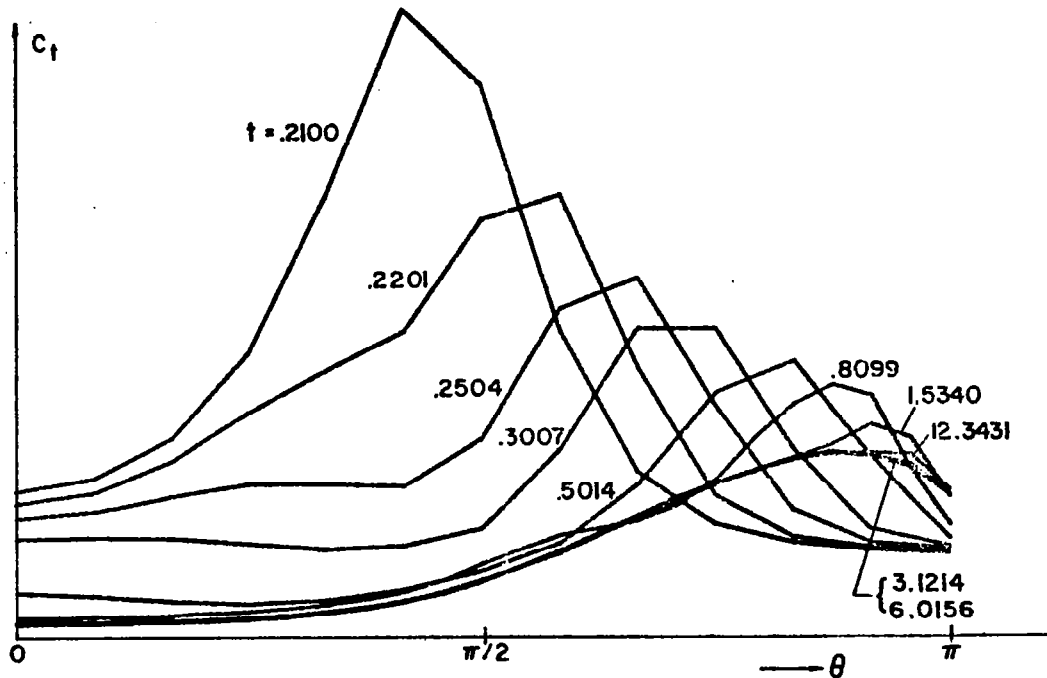


Fig. 19

discrepancy. At this time, it is hardly possible to make a statement about the accuracy of either result.

A second computation was performed (Run 24) with $A=.3640$, $B=.1667$, $M_\infty = 2$, at an angle of attack equal to 10° . The hollow intake is assumed at $t=1$; 24 intervals are used circumferentially; radially, we start with 3 intervals, doubling them at $t=1.25$ and again at $t=1.6$; the stretching parameter is taken equal to 1.

The computation is halted at step 1000 ($t=11.112$). A sequence of isobar plots is shown in Fig. 24. In Fig. 25, the values of P around the body are compared with results by other Authors [12,13]. The agreement between the present results and those obtained by relaxation is excellent in the windward side. On the leeward side, our results seem to overshoot the expansion and the 'shock' appears too far to the left.

In order to assess the reliability of the calculation and the effect of resolution in the radial direction, the calculation

Elliptic cones

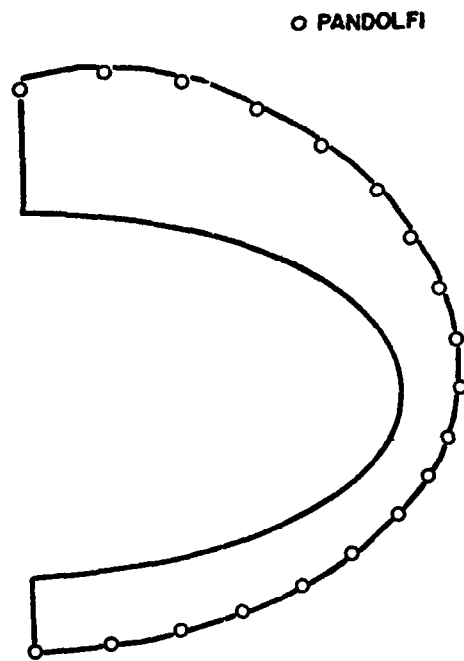


Fig. 20

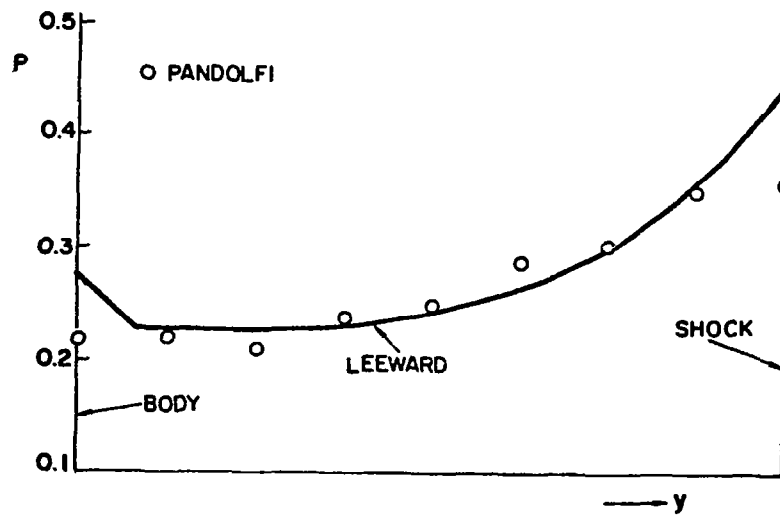


Fig. 21

Elliptic cones

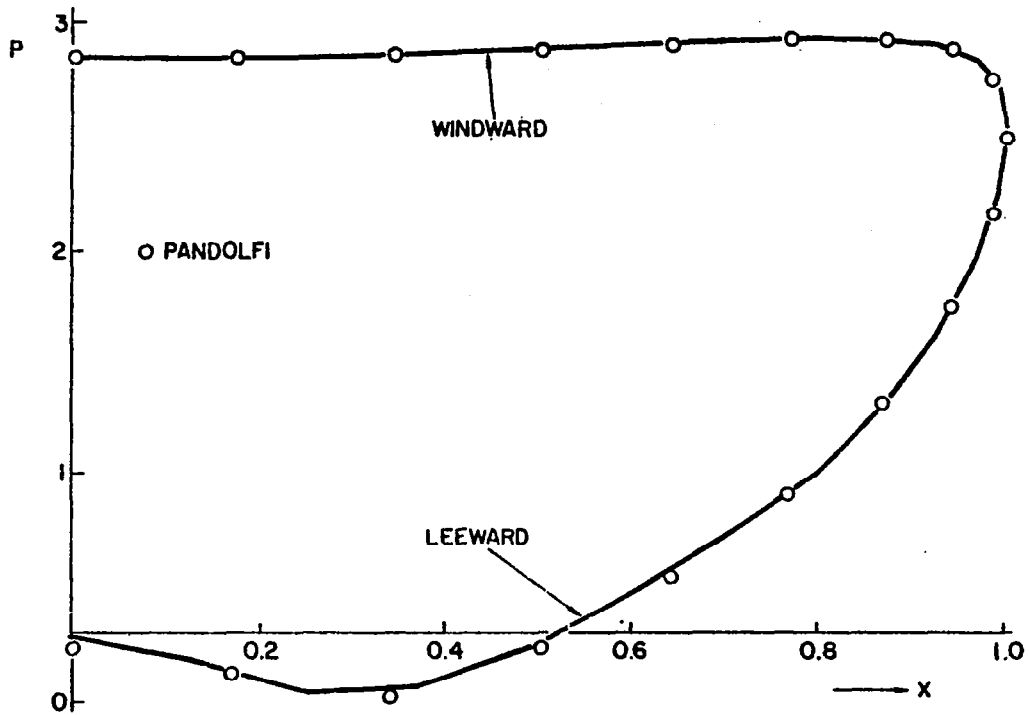


Fig. 22

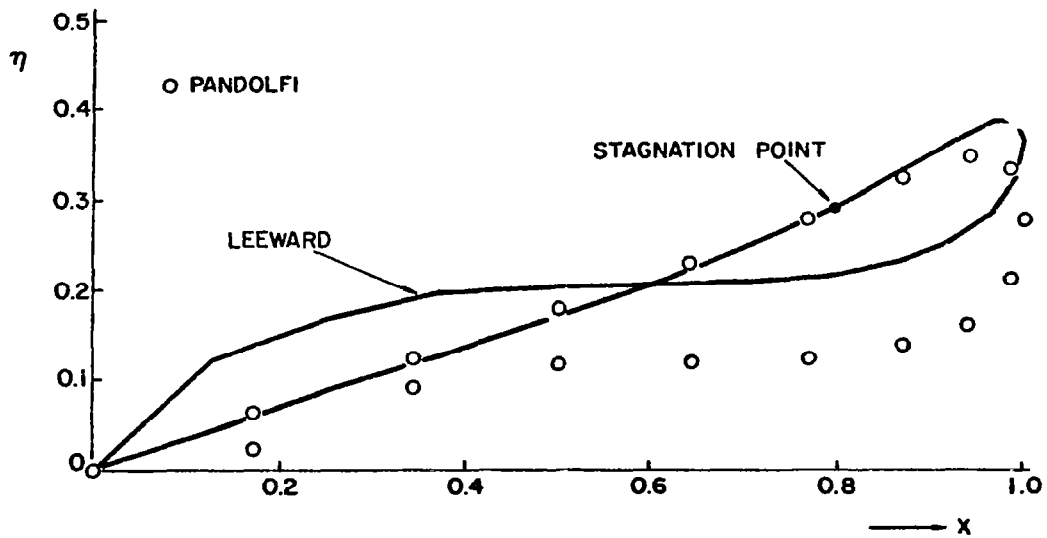
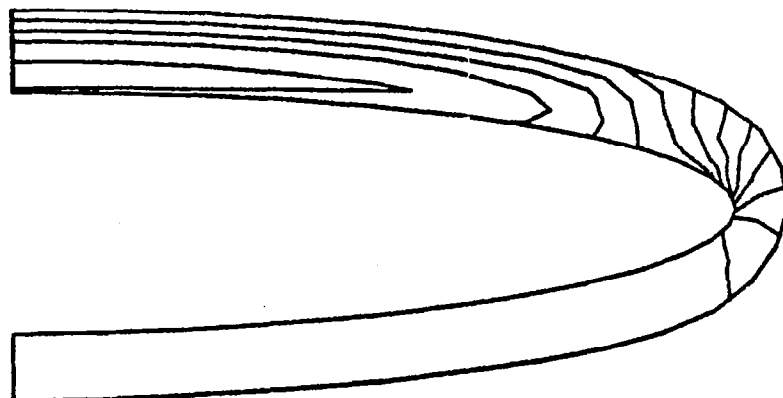
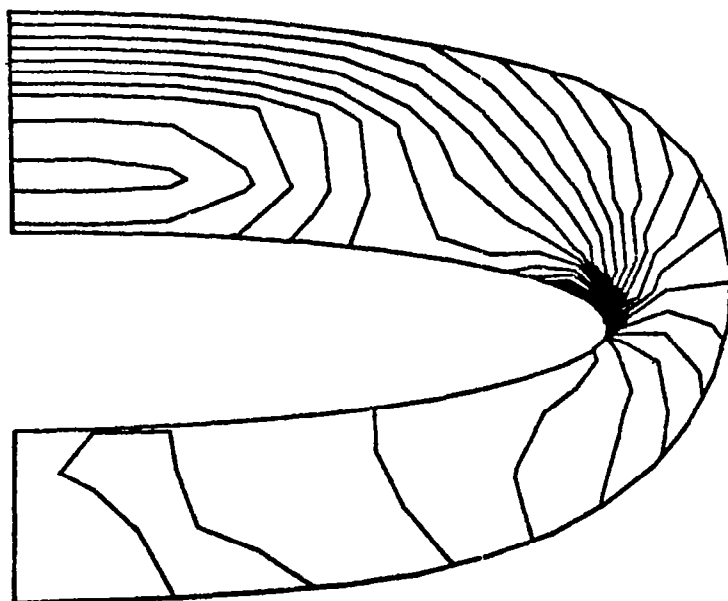


Fig. 23

Elliptic cones

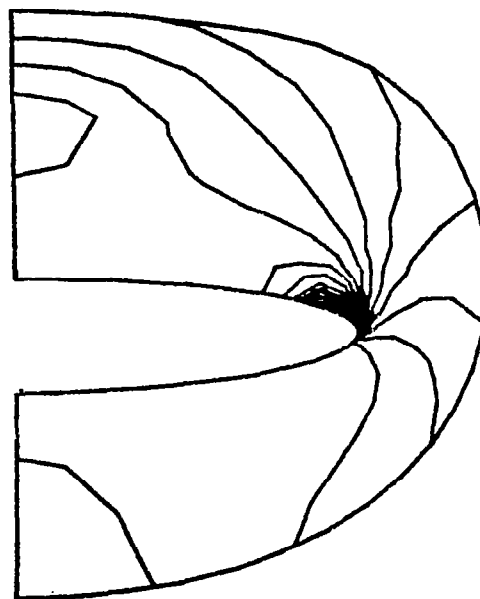


RUN= 24 M= 2.00 K= 50 T= 1.0569 DREF=0.1000 MAX=0.7000 2



RUN= 24 M= 2.00 K= 100 T= 1.2095

DREF=0.0500 MAX=0.7000 2

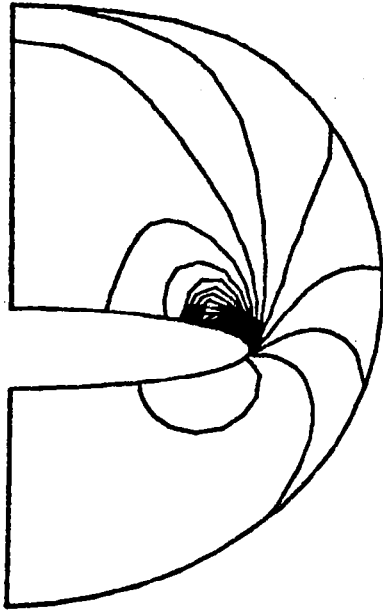


RUN= 24 M= 2.00 K= 200 T= 1.5811

DREF=0.1000 MAX=0.6000 2

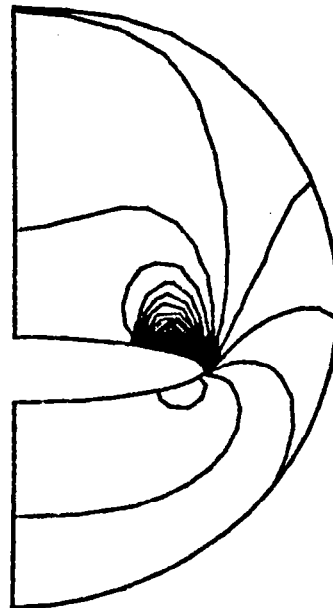
Fig. 24(a)

Elliptic cones



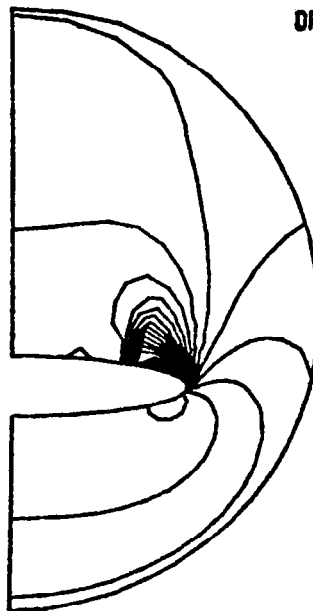
RUN= 24 M= 2.00 K= 400 T= 2.410

DREF=0.1000 MAX=0.5000



RUN= 24 M= 2.00 K= 700 T= 5.1403

DREF=0.1000 MAX=0.5000 2



RUN= 24 M= 2.00 K=1000 T= 11.1120

DREF=0.1000 MAX=0.5000 2

Fig. 24(b)

Elliptic cones

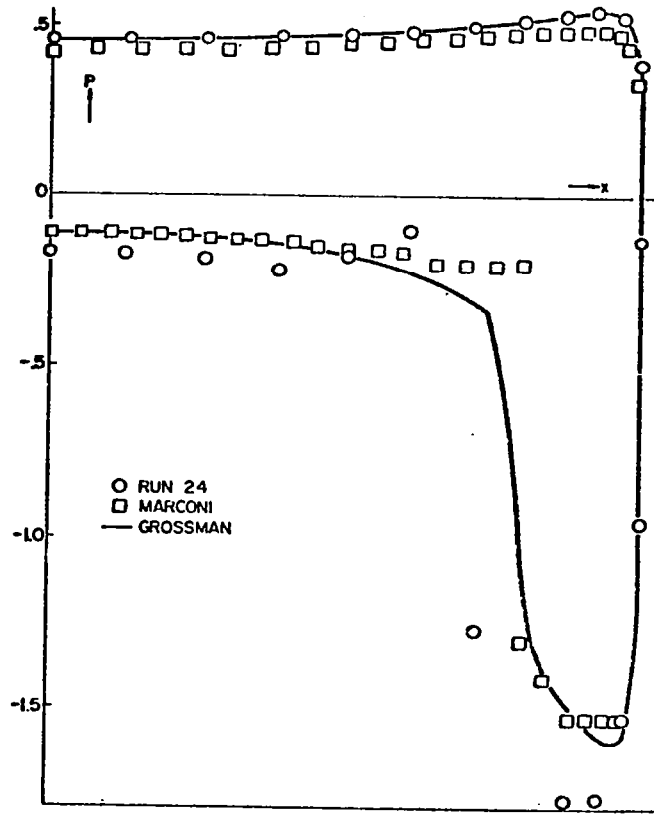


Fig. 25

has been repeated increasing the stretching parameter to 1.5 (Run 124). To avoid difficulties in the initialization, the initial conditions are taken from the solution of a circular pointed cone at zero angle of attack, the cone semi-angle being equal to 20° . The initial cross section is located at $t=0.1$; doubling of the radial intervals occurs at $t=0.125$ and $t=0.16$. In Fig. 26, our results after 1500 computational steps are compared again with those of [13]. The overshoot is slightly improved, but the mesh is definitively too coarse circumferentially to resolve the shock properly. Whether the shock could be 'captured' in the right position by using a finer mesh, still remains an open question. One thing which appears from the evolution of the calculation is that the improper collocation of the shock is closely related to a progressive deterioration of the flow downstream of it. Some wiggles develop in the pressure distribution on the leeward side of the body, as t increases. In conclusion, fitting of the imbedded shock is necessary for accuracy on the leeward side, at

Elliptic cones

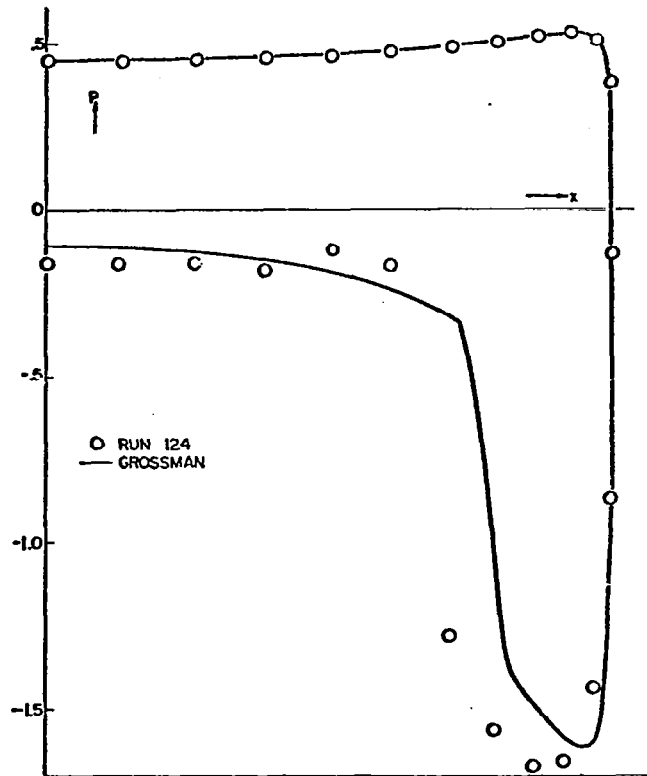
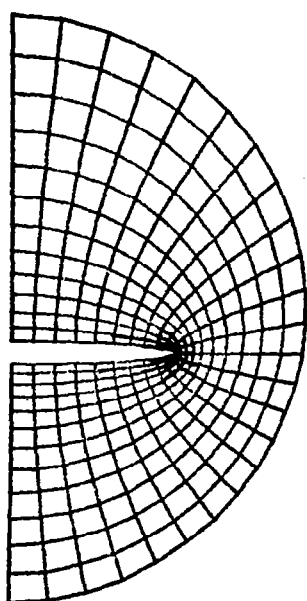


Fig. 26

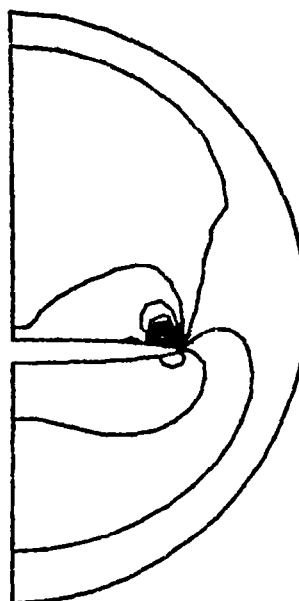
least with the present resolution.

Finally, the flow past an elliptic cone with a 1:14 axis ratio was evaluated (Run 25). In this case, $A=0.3640$, $B=0.0714$, $M_\infty=2$, at an angle of attack equal to 5° . The computation is started at $t=0.1$, assuming, as in Run 124, that the initial conditions are given by the solution of the conical flow at zero incidence about a circular cone having a diameter equal to the major axis of the elliptic cone. The number of intervals and their doublings are as in Run 124. The computational grid and a set of isobars at step 2000 are shown in Fig. 27. In Fig. 28, the pressure coefficient is compared with the results of other Authors [12,13]. In this case the agreement is better, despite the extreme coarseness of the mesh. This case is, in my opinion, a good example of the efficiency of the computational technique. Note that Marconi's results have been obtained with a method very similar to the present one, but not employing the λ -scheme, and with a careful fitting of the imbedded shock; note how much finer his mesh is. Nevertheless, our present 'shock' is in the computational cell where the fitted one appears; about the wiggles and

Elliptic cones



RUN= 25 M= 2.00 K=2000 T= 1.8787



RUN= 25 M= 2.00 K=2000 T= 1.8787

DREF=0.1000 MAX=0.4000 2

Fig. 27

general discrepancy of results behind the shock, we can repeat the comments to Runs 24 and 124; we may also note explicitly that our 'shock' is isentropic. We are sure that no higher resolution is needed for the calculation of these flows, once the code is supplemented by a shock-fitting routine.

Elliptic cones

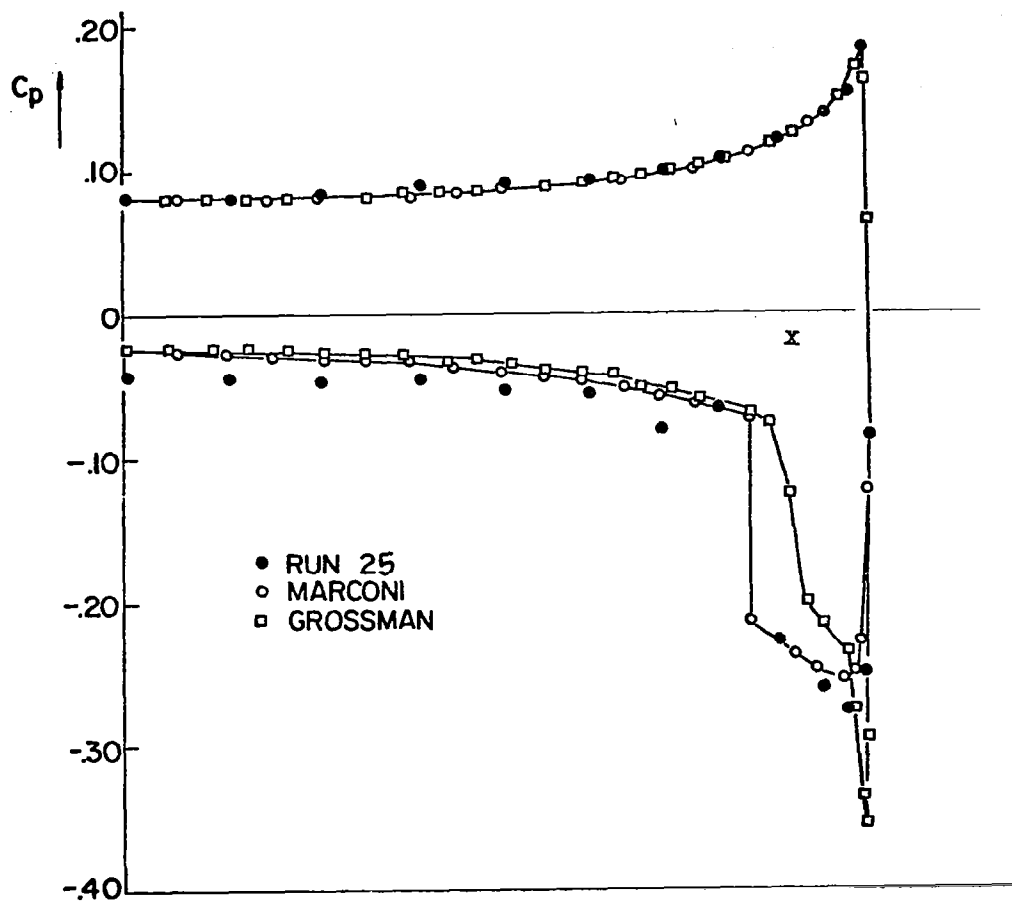


Fig. 28

19. Cambered wings

To test the program on shapes which are of current interest, without making the mapping unnecessarily cumbersome, we

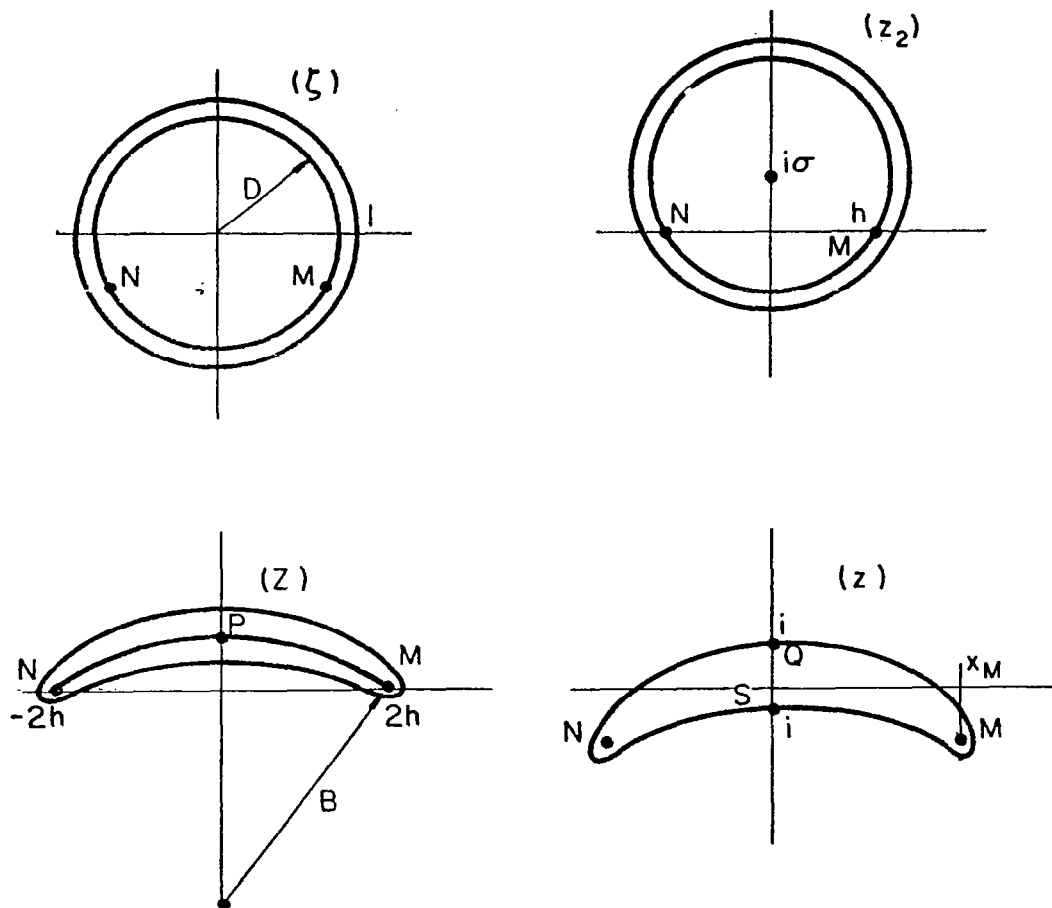


Fig. 29

generate a cambered wing as follows (Fig. 29). In the ζ -plane, a circle centered at the origin and with a radius D is considered as the image of the camber line of the wing. Another circle, concentric to the first, with a radius l , is the image of the wing itself. The z_2 -plane is obtained from the ζ -plane by a simple translation:

Cambered wings

$$z_2 = \zeta + i\sigma \quad , \quad \zeta = z_2 - i\sigma \quad (204)$$

Let ζ_M be the point of the ζ -plane whose image in the z_2 -plane is h . Let the Z -plane be obtained from the z_2 -plane via a Joukowski mapping:

$$Z = z_2 + \frac{h^2}{z_2} \quad (205)$$

In the Z -plane, the camber line becomes a circular arc counted twice. Finally, let a second translation be applied to get the z -plane from the Z -plane:

$$z = Z - i\beta \quad , \quad Z = z + i\beta \quad (206)$$

We want the cambered wing to have a maximum thickness equal to 2, with its points z_Q and z_S equal to $-i$ and $+i$, respectively. Let

$$C = B - (B^2 - 4h^2)^{1/2} \quad (207)$$

where B is a prescribed constant. Clearly, C is the distance between point P in the Z -plane and the origin, if B is the radius of the camber line. Therefore,

$$\sigma + D - \frac{h^2}{\sigma + D} = C \quad (208)$$

Let us prescribe the variation of x_M with t , for example by saying that

$$x_M = At \quad (209)$$

where A is a prescribed constant. It follows that

$$h = At/2 \quad (210)$$

Since, as it can be seen in the z_2 -plane,

$$D^2 = h^2 + \sigma^2 \quad (211)$$

(208) and (211) provide D and σ as functions of h :

Cambered wings

$$D = (M+h^2/M)/2 \quad , \quad \sigma = (M-h^2/M)/2 \quad (212)$$

where

$$M = \frac{1}{2} [C+2BC]^{1/2} \quad (213)$$

and, because of (210), of t . The remaining two unknown parameters, l and β , are determined by the conditions imposed upon points Q and S in the z -plane:

$$\sigma - 1 - \frac{h^2}{\sigma-1} = -1 + \beta \quad (214)$$

$$\sigma + 1 - \frac{h^2}{\sigma+1} = 1 + \beta \quad (215)$$

Therefore, l can be determined by solving the third degree equation (which has only one real root):

$$(1 - l) (\sigma^2 - l^2) + h^2 l = 0 \quad (216)$$

and β follows from (215). The t -derivatives are:

$$h_t = A/2 \quad (217)$$

$$\sigma_t = \frac{DMC_t + hh_t(C-2\sigma)}{(2M - C) M} \quad (218)$$

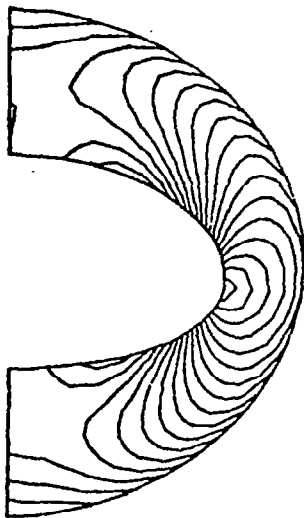
$$D_t = (hh_t + \sigma\sigma_t)/D \quad (219)$$

$$l_t = 2 \frac{DlD_t - \sigma\sigma_t}{(3l-2) l - D^2} \quad (220)$$

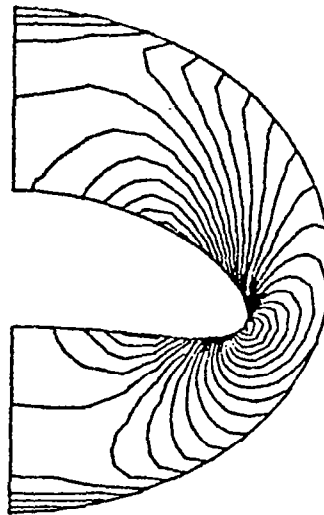
$$\beta_t = (\sigma_t + l_t) \left(1 + \frac{h^2}{(\sigma+1)^2} \right) - \frac{2hh_t}{\sigma+1} \quad (221)$$

Since we do not have an implicit form, $F(x,y,t)=0$ for the wing contour, and we need F_x , F_y , and F_t , we may proceed as follows. First, we use (10), (15) and (22) to evaluate

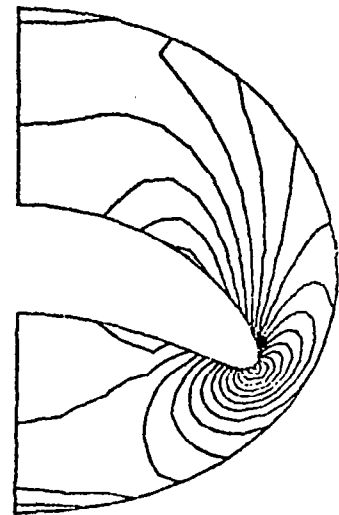
Cambered wings



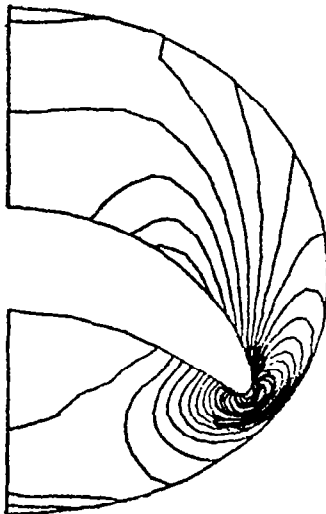
RUN= 28 M= 3.00 K= 100
DREF=0.0500 MAX=0.6500 2
T= 4.2947



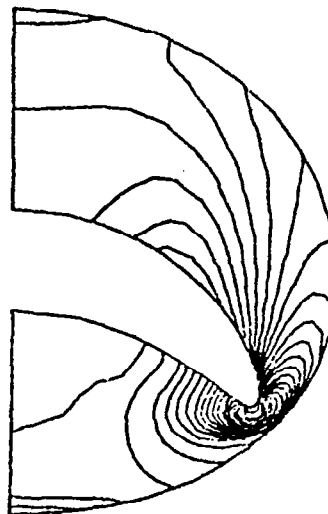
RUN= 28 M= 3.00 K= 200
DREF=0.0500 MAX=1.0000 2
T= 8.0200



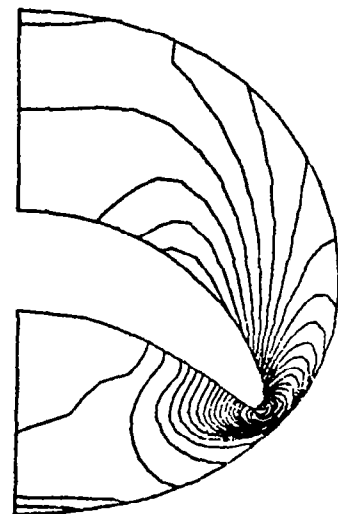
RUN= 28 M= 3.00 K= 300
DREF=0.1000 MAX=1.4600 2
T= 10.4976



RUN= 28 M= 3.00 K= 400
DREF=0.1000 MAX=1.8000 2
T= 11.4635



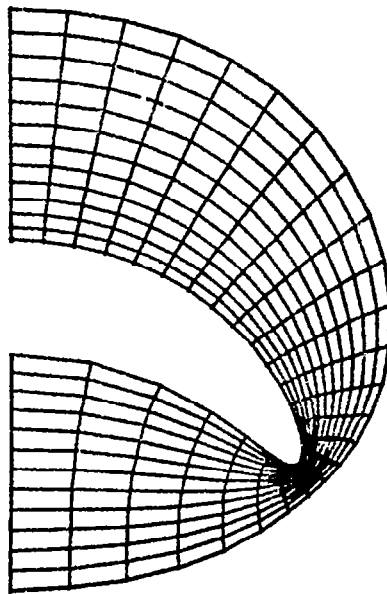
RUN= 28 M= 3.00 K= 500
DREF=0.1000 MAX=2.1000 2
T= 11.7721



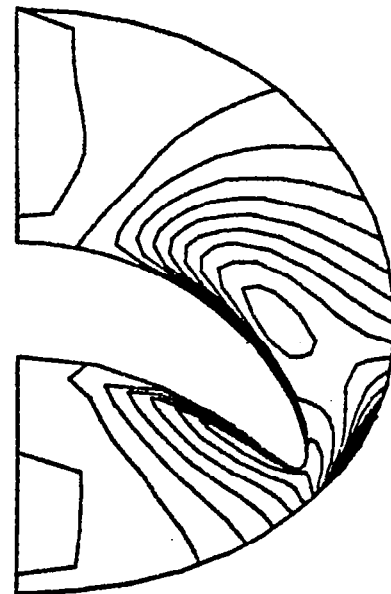
RUN= 28 M= 3.00 K= 550
DREF=0.1000 MAX=2.1000 2
T= 11.8247

Fig. 30

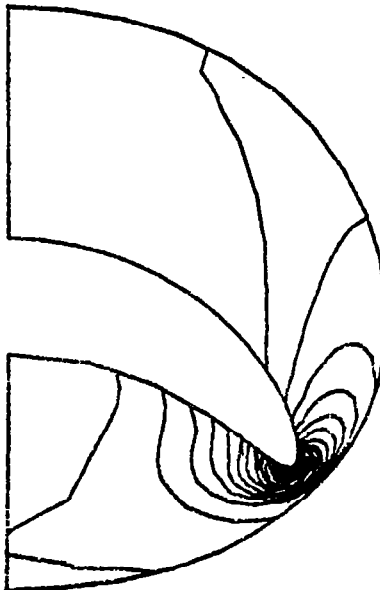
Cambered wings



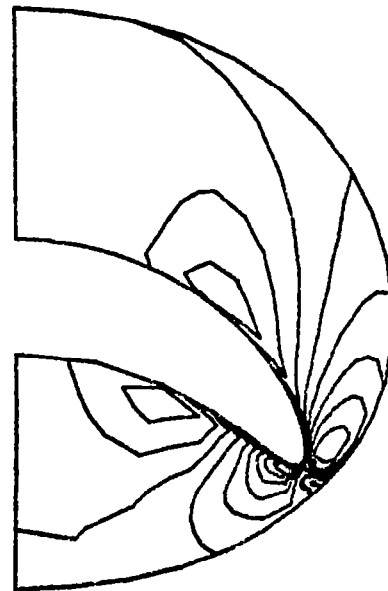
RUN= 28 M= 3.00 K= 550
T= 11.8247



RUN= 28 M= 3.00 K= 550
DREF=0.0010 MAX=0.0160 3
T= 11.8247



RUN= 28 M= 3.00 K= 550
DREF=0.0500 MAX=1.0500 4
T= 11.8247



RUN= 28 M= 3.00 K= 550
DREF=0.0200 MAX=0.2200 5
T= 11.8247

Fig. 31

Cambered wings

$$\mathcal{S}_x = \mathcal{L}(\theta_x - \omega_x) = -\frac{G\mathcal{L}}{1}[\mathcal{S}(1-\phi_1) + \mathcal{L}\phi_2] \quad (222)$$

$$\mathcal{L}_y = -\mathcal{S}(\theta_y - \omega_y) = -\frac{G\mathcal{L}}{1}[\mathcal{S}(1-\phi_1) + \mathcal{L}\phi_2] + \frac{G}{1}\phi_2 = \mathcal{S}_x + \frac{G}{1}\phi_2 \quad (223)$$

(note that $\mathcal{L} + i\mathcal{S}$, defined by (9), is not an analytic function; therefore, $\mathcal{L}_y \neq \mathcal{S}_x$). Now, since the image of the wing in the ζ -plane is a perfect circle, b_θ vanishes identically. Therefore, (38) tells us that

$$F_y = K\mathcal{S}, \quad F_x = K\mathcal{L} \quad (224)$$

where K is a function to be determined. By writing that $F_{xy} = F_{yx}$ and using (21) we see that K is defined by

$$K_x\mathcal{S} - K_y\mathcal{L} = K \frac{G}{1}\phi_2 \quad (225)$$

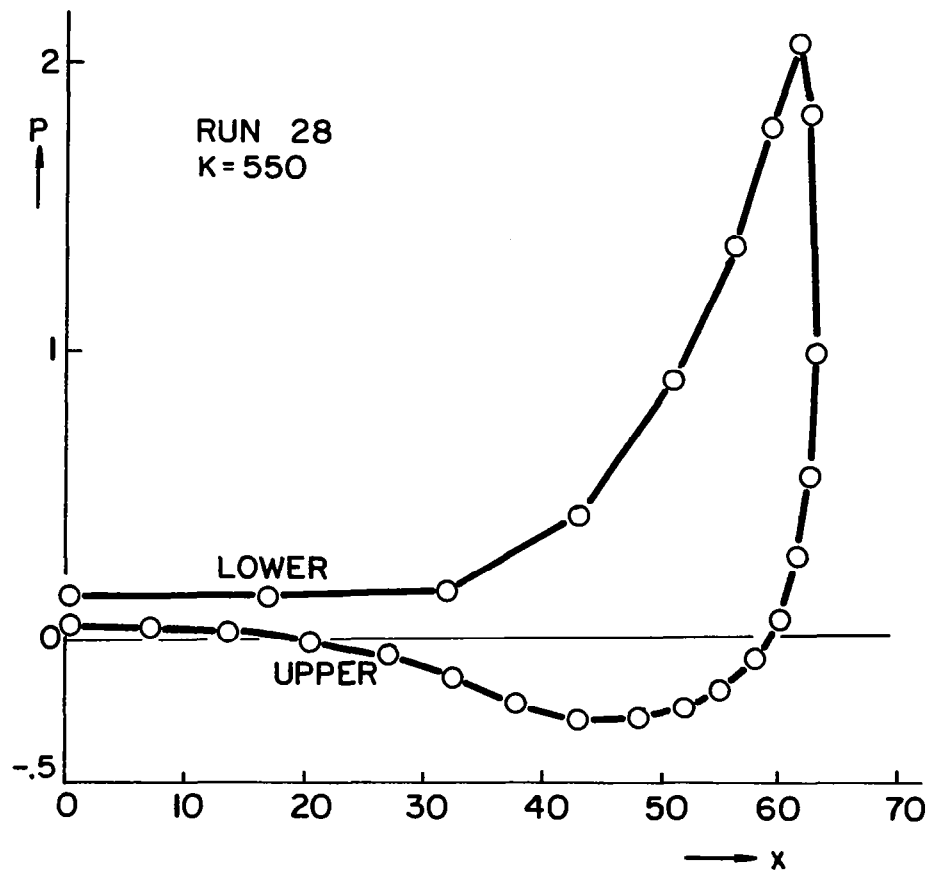


Fig. 32

The equation is satisfied by $K = G$, as (225) proves. Therefore,

Cambered wings

$$F_x = G\ell \quad , \quad F_y = G\mathcal{L} \quad (226)$$

In addition, starting from (41) and the first of (31), with $b_Y=0$ and $b = 1$, we obtain

$$F_t = \frac{1}{G}(\ell f_1 - l_t)(\ell F_x + \mathcal{L} F_y) = \ell f_1 - l_t \quad (227)$$

As is evident from Fig. 29 and Eqs. (208) through (210), only one mapping function is needed to obtain the circle image of the wing. The pertinent value of δ is obviously $1/2$ and the position of the hinge-point in the physical plane is that of point M, that is,

$$h_{11} = At - i\beta \quad , \quad \dot{h}^{11} = A - i\beta_t \quad (228)$$

The other two points of interest are the lower and upper intersection of the wing with the $x = 0$ line, viz.

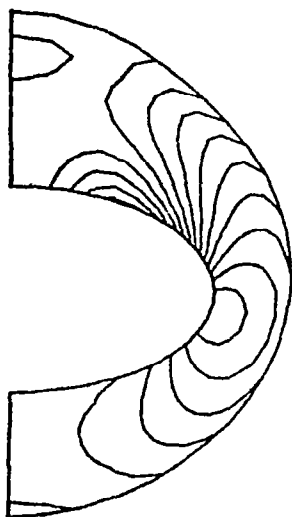
$$h_{21} = -i \quad , \quad h_{31} = i \quad (229)$$

Their t -derivatives obviously vanish identically.

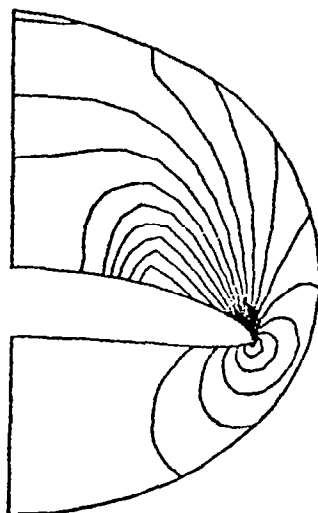
Two examples are given. In the first (Run 28), the angle of attack is zero and the free stream Mach number is 3. The values of A and B are 0.4 and 5, respectively. The stretching parameter, α , is equal to 1. The hollow intake is at $t=.5$; initially, we have 3 intervals radially and 12 circumferentially; the radial intervals are doubled at $t=2$ and 3.5; the circumferential intervals are doubled at $t=2$. Some isobar plots are shown in Fig. 30; the computational grid and level lines of σ , η and S at step 550 are shown in Fig. 31. Finally, in Fig. 32 the pressure distribution around the body at step 550 is shown.

In the second example (Run 29), the angle of attack is 5° and B is 20. All the other values are unchanged. Again, we show isobar plots in Fig. 33, the computational grid and level lines of σ , η and S at step 1100 in Fig. 34, and the pressure distribution around the body at step 1100 in Fig. 35.

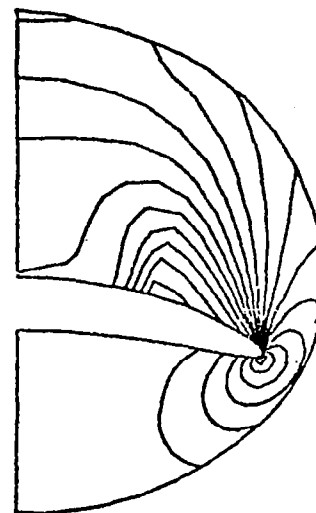
Cambered wings



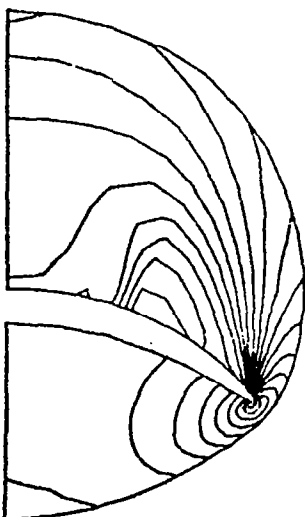
RUN= 29 M= 3.00 K= 100
DREF=0.1000 MAX=0.0000 2
T= 4.2265



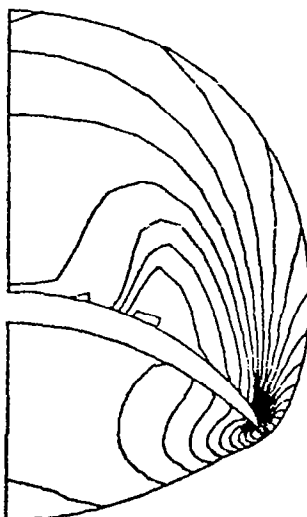
RUN= 29 M= 3.00 K= 400
DREF=0.1000 MAX=0.9000 2
T= 16.0356



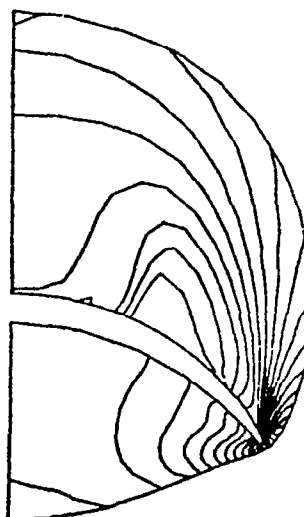
RUN= 29 M= 3.00 K= 550
DREF=0.1000 MAX=1.0000 2
T= 22.5321



RUN= 29 M= 3.00 K=1100
DREF=0.1000 MAX=1.2000 2
T= 35.3109



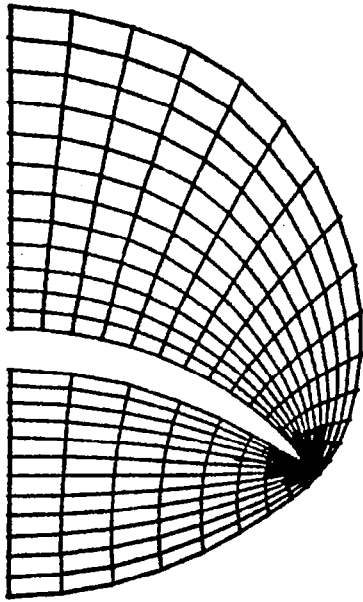
RUN= 29 M= 3.00 K=1500
DREF=0.1000 MAX=1.6000 2
T= 40.5016



RUN= 29 M= 3.00 K=2000
DREF=0.1000 MAX=1.6000 2
T= 42.9527

Fig. 33

Cambered wings

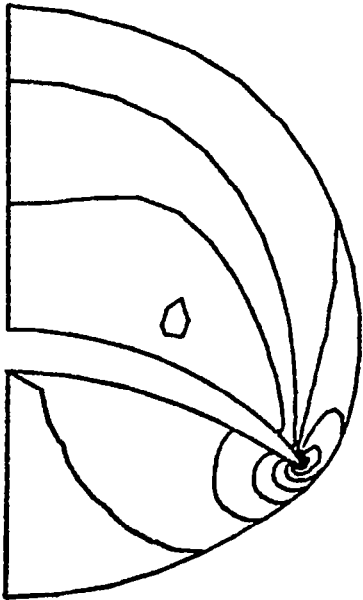


RUN= 29 M= 3.00 K=1100 T= 35.3109



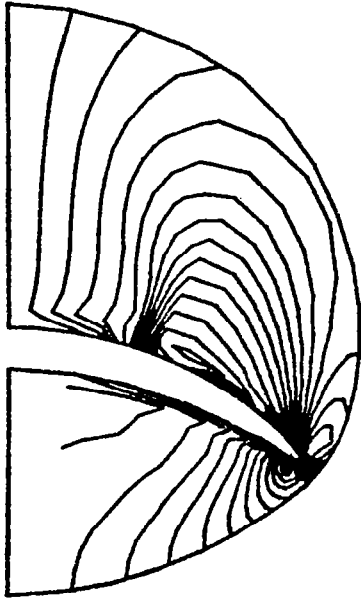
RUN= 29 M= 3.00 K=1100 T= 35.3109

DREF=0.0020 MAX=0.0200 3



RUN= 29 M= 3.00 K=1100 T= 35.3109

DREF=0.0400 MAX=0.5200 4



RUN= 29 M= 3.00 K=1100 T= 35.3109

DREF=0.0100 MAX=0.2000 5

Fig. 34

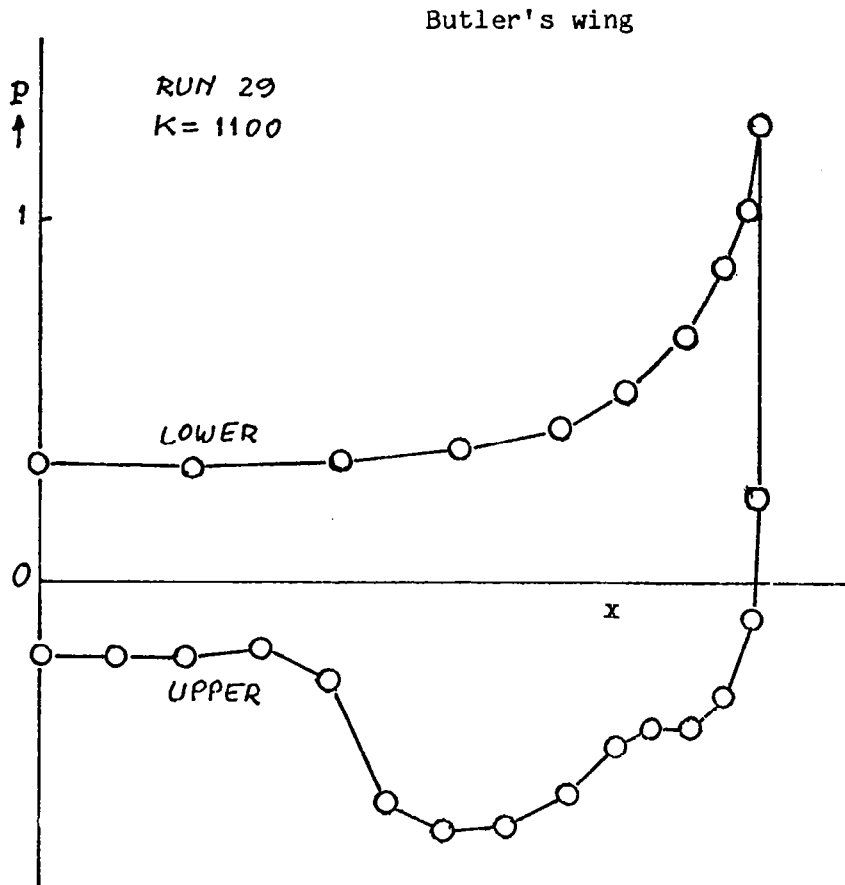


Fig. 35

20. Butler's wing

Another set of tests has been run in connection with work in progress at the University of Salford, UK. A body is defined as follows. For the first 20% of its length the body is a circular cone. The remainder of the body has elliptic sections which become more eccentric as the sharp trailing edge is approached. The values of a and b as defined by (201) are:

$$a = At$$

$$b = At \quad 0 \leq t \leq .2 \quad (230)$$

$$b = At \left[1 - \left(\frac{t-.2}{.8t} \right)^4 \right] \quad .2 \leq t \leq 1$$

This body was considered in [14] and we will call it Butler's wing for brevity. From (230) it follows that

$$a_t = A$$

Butler's wing

$$b_t = A \quad 0 \leq t \leq .2 \quad (231)$$

$$b_t = \frac{b}{t} - \frac{A}{64t} (5 - \frac{1}{t})^3 \quad .2 \leq t \leq 1$$

and

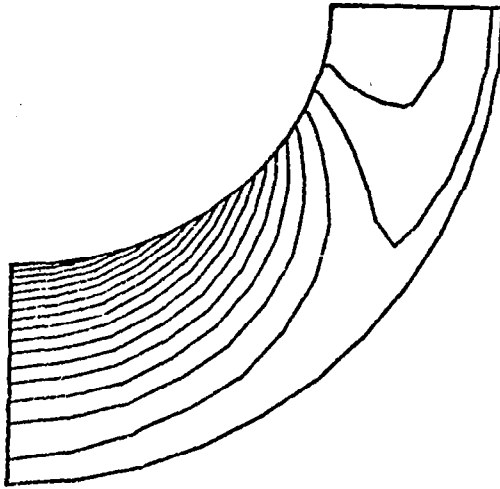
$$F_x = 2x/a^2, \quad F_y = 2y/b^2, \quad F_t = -2(Ax^2/a^3 + b_t y^2/b^3) \quad (232)$$

The definition of the mapping and the location of the hinges are obviously similar to the ones given for the elliptic cone.

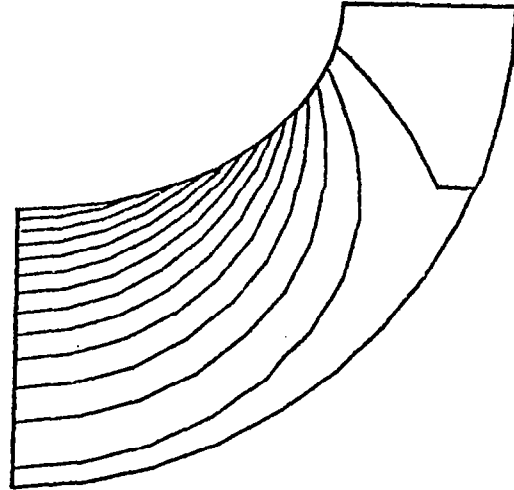
The value of A was chosen as 0.29814; the free stream Mach number is 3.5. The first calculation (Run 14) was made at no incidence, with $\alpha=2$, using 12 intervals radially and beginning with 6 intervals circumferentially; the number of circumferential intervals was doubled at $t=.4$ and again at $t=.6$. Typical isobar plots are shown in Fig. 36. In Figs. 37 and 38 some experimental values [14,15] are compared with the results of our calculation. In Fig. 39 our results are compared with Butler's. It is obvious that our results are closer to the experimental values, which should not be a surprise since our calculations took advantage of twenty years of improvements in numerical techniques; the match is not perfect, however, and possible effects, for example of viscosity, remain to be explored.

A similar comparison is given in Fig. 40 for the same wing, same free stream Mach number, at an angle of attack of 10° .

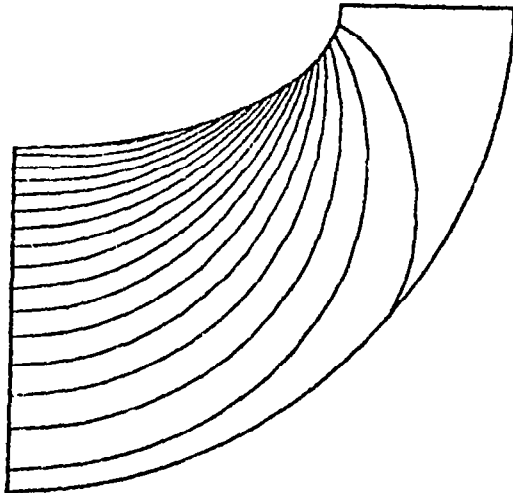
Butler's wing



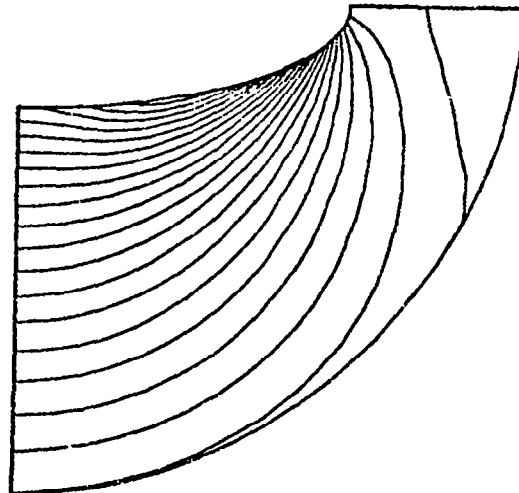
RUN= 14 M= 3.50 K= 200 T= 0.4032 DREF=0.0500
MAX=0.9500 2



RUN= 14 M= 3.50 K= 275 T= 0.5105 DREF=0.1000
MAX=0.8000 2



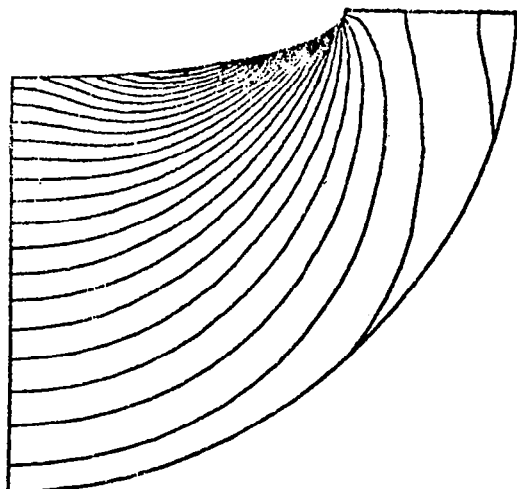
RUN= 14 M= 3.50 K= 350 T= 0.6354 DREF=0.1000
MAX=6.7000 2



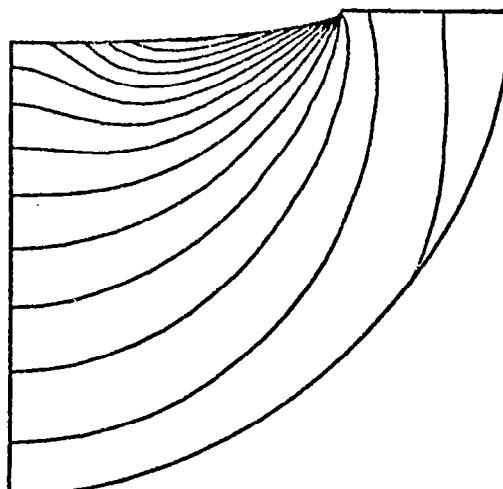
RUN= 14 M= 3.50 K= 400 T= 0.7219 DREF=0.1000
MAX=0.7000 2

Fig. 36(a)

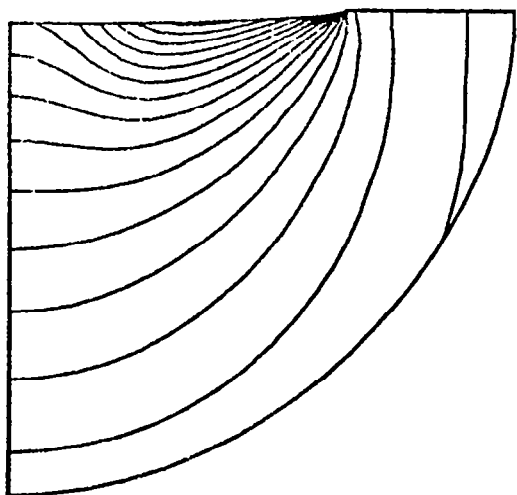
Butler's wing



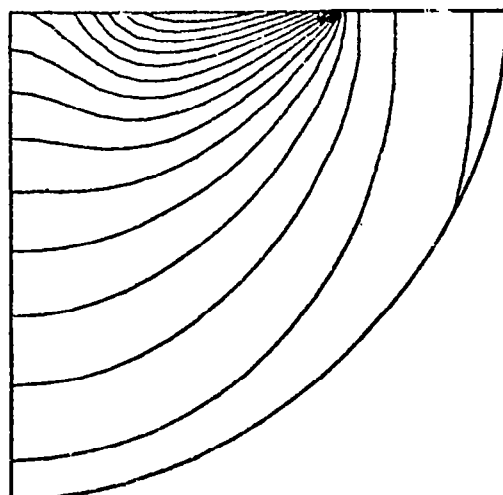
RUN= 14 M= 3.50 K= 450 T= 0.8025 DREF=0.1000
MAX=0.7000 2



RUN= 14 M= 3.50 K= 525 T= 0.8967 DREF=0.2000
MAX=0.6000 2



RUN= 14 M= 3.50 K= 600 T= 0.9525 DREF=0.2000
MAX=0.6000 2



RUN= 14 M= 3.50 K= 725 T= 0.9895 DREF=0.2000
MAX=0.6000 2

Fig. 36(b)

Butler's wing

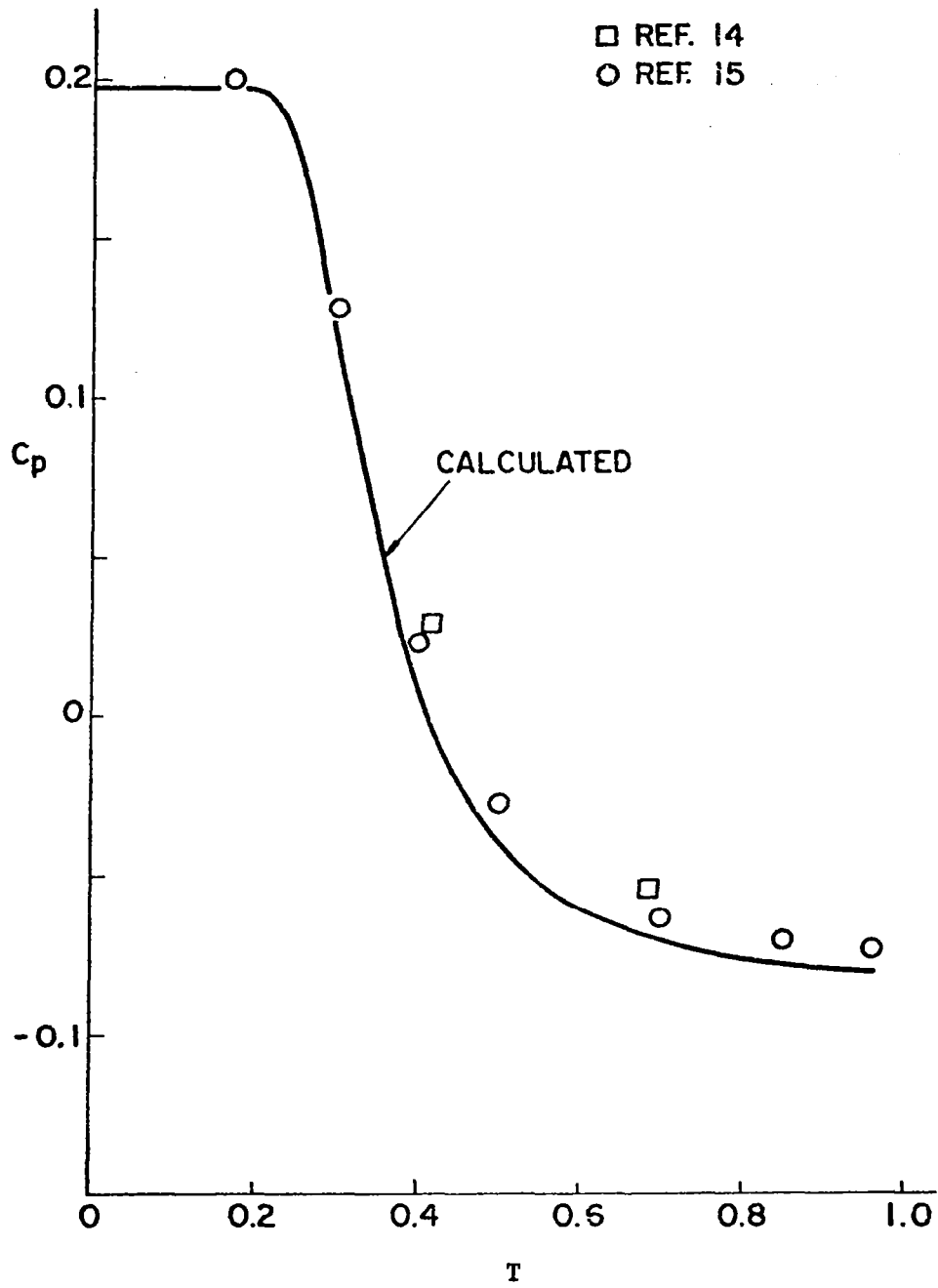


Fig. 37

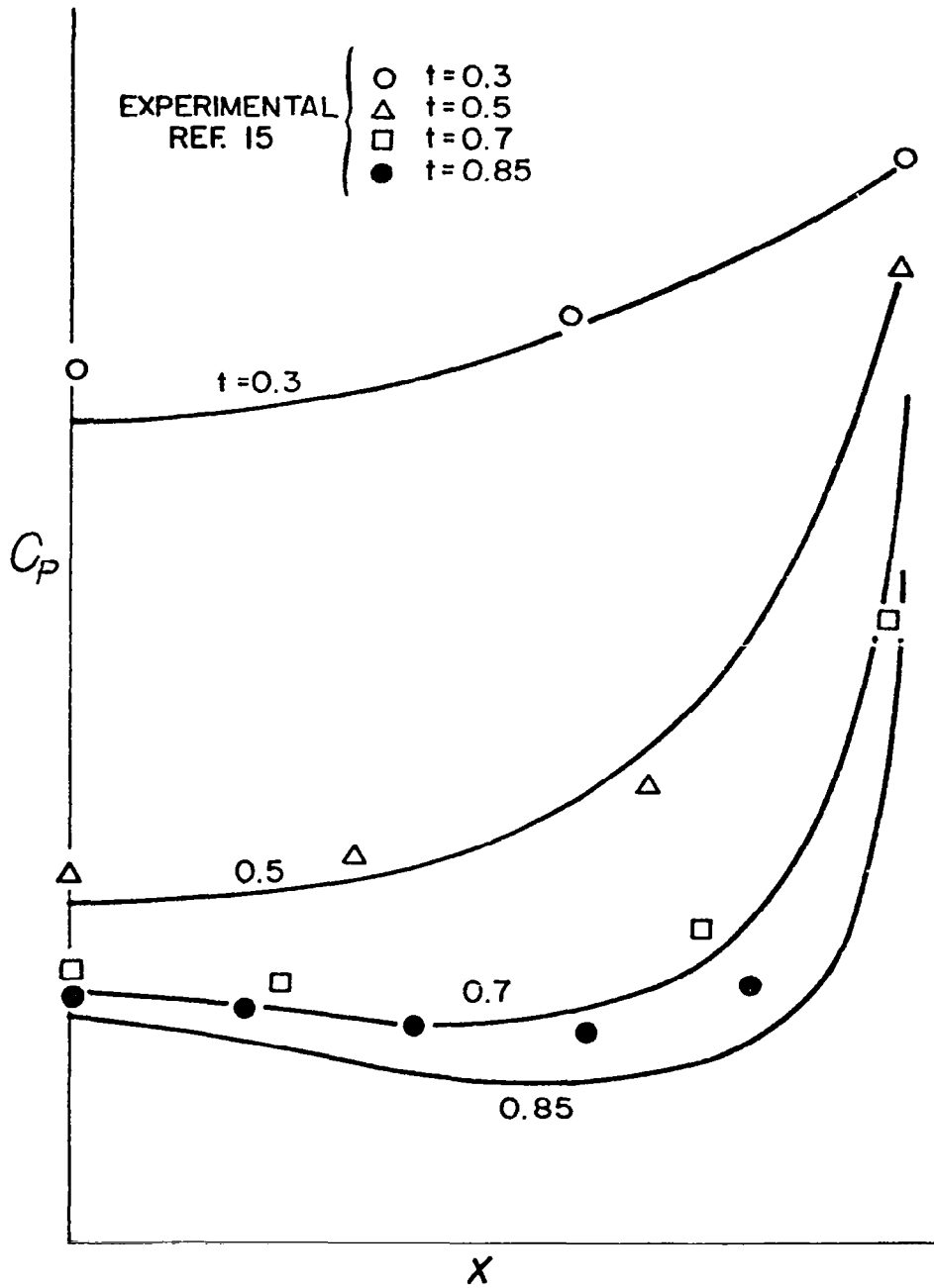


Fig. 38

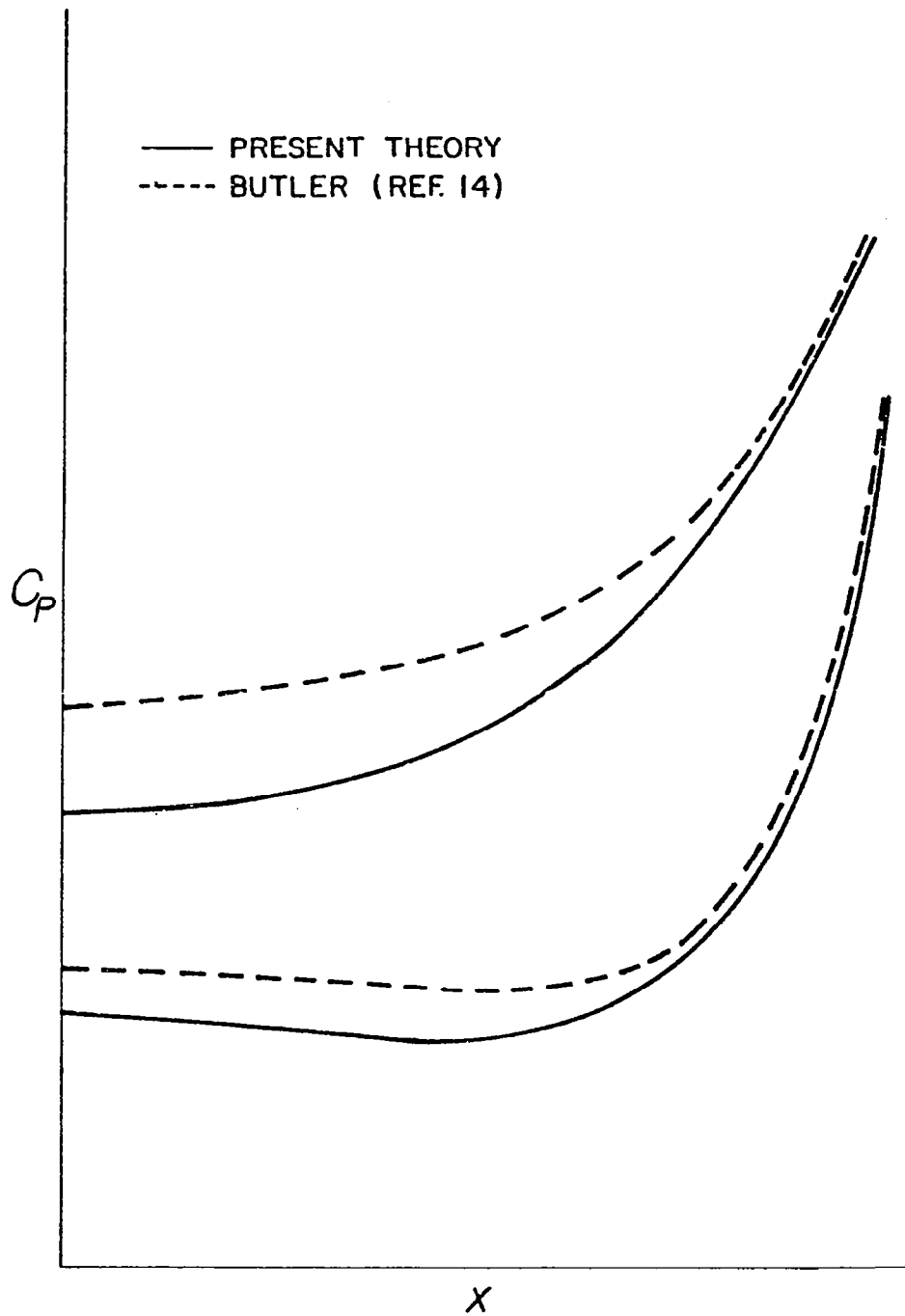


Fig. 39

Butler's wing

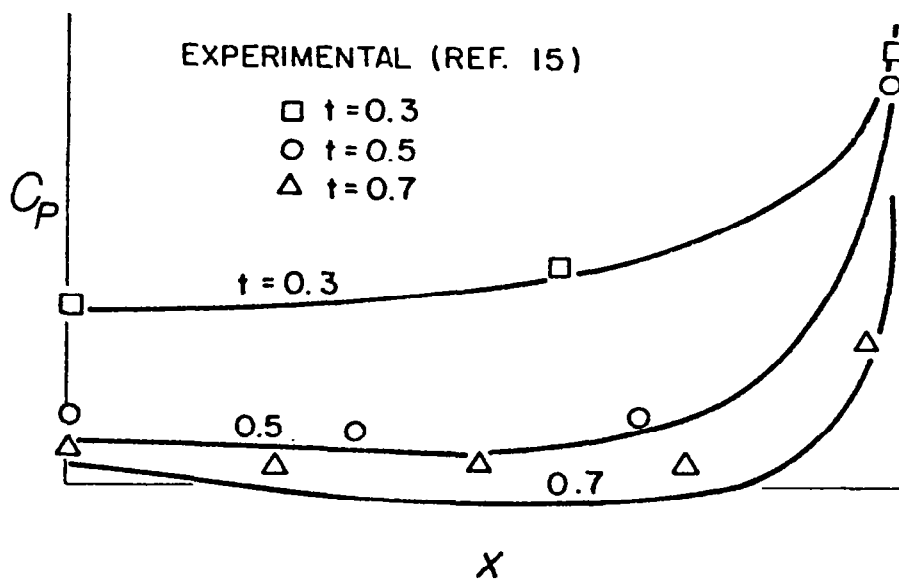
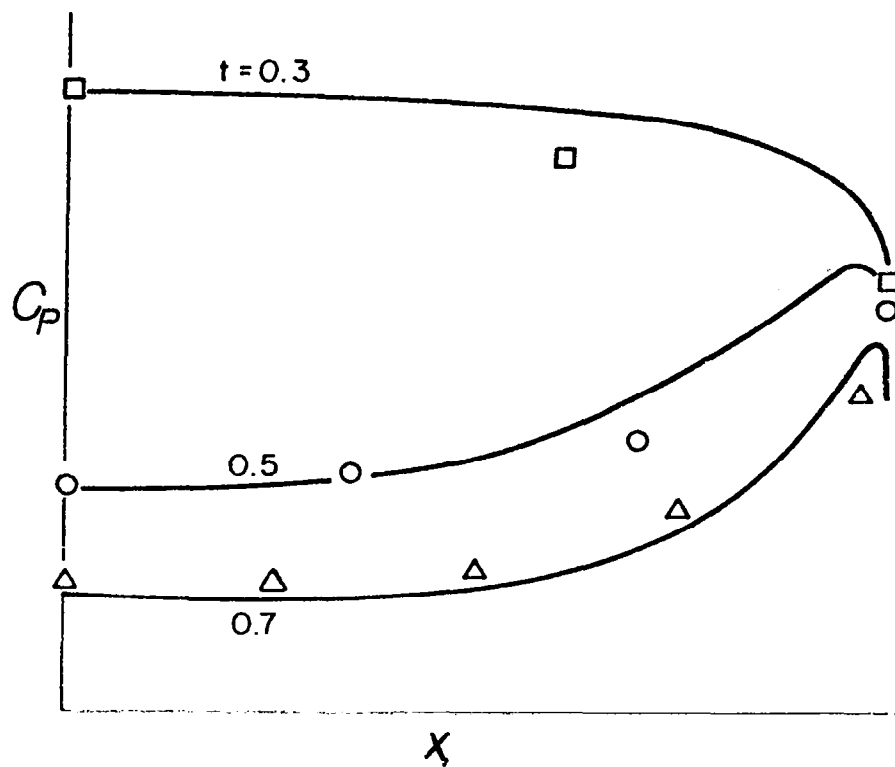


Fig. 40

21. A simple fuselage-arrow-wing combination

A configuration which is closer to a realistic airplane geometry with a distinctive differentiation between a fuselage and an arrow wing has been defined as explained in this Section. To maintain the analysis as clean as possible, the entire geometry has been defined analytically. The configuration has been chosen trying to minimize causes of formation of imbedded shocks.

The top view of the airplane (Fig. 41) shows a straight 'leading edge',

$$x = a = At \quad (233)$$

where A is an input value. The nose of the airplane is an elliptic cone, whose cross-sections are defined by

$$\frac{x^2}{a^2} + \frac{y^2}{B^2} = 1 \quad (234)$$

with

$$B = \frac{t(A+\beta t)}{1+\beta t} \quad (235)$$

where

$$\beta = A - 2/t_3, \quad \beta = -1/t_3^2 \quad (236)$$

and t_3 is an input value. It follows that

$$B_t = \frac{B}{t} + \frac{t(\beta - A\beta)}{(1+\beta t)^2} \quad (237)$$

A simple fuselage-arrow-wing combination

and $B = 0$, $B_t = A$ at $t = 0$ and $B = 1$, $B_t = 0$ at $t = t_3$.

Another line,

$$x = x_0(t) \quad (238)$$

defines the 'center' of a wing which begins at $t = t_0$, the latter being an input value. The wing is a Joukowski profile, modified by an additional thickness to give it some structural strength. The basic profile is obtained by mapping a circle,

$$\bar{\zeta} = g + 1 e^{i\phi} \quad (239)$$

onto the z -plane, via the transformations

$$z_1 = x_1 + y_1 = x_0 + \bar{\zeta} + k^2/\bar{\zeta}, \quad z = x_1 + i\beta y_1 \quad (240)$$

The additional thickness is obtained by adding a value, \bar{y} , given by

$$\bar{y} = \beta(x - x_{TE}) \left(\frac{x - a}{x_{TE} - a} \right)^2 \quad (241)$$

where x_{TE} is the abscissa of the trailing edge of the Joukowski profile, to each y obtained from (239) and (240); β is a function of t , to be defined later. Beyond t_0 , an elliptic fuselage,

$$x^2 + \frac{y^2}{B^2} = 1 \quad (242)$$

begins to be differentiated from the wing, until at $t = t_1$ (an input value) wing and fuselage become detached. The end of the airplane is at $t = t_2$ (another input value).

To assure a smooth transition from the nose to the wing-fuselage arrangement, the Joukowski profile must be made to coincide with the elliptic cross-section at $t = t_0$, and no additional thickness must be used there. This is obtained by imposing the conditions:

A simple fuselage-arrow-wing combination

$$g=g_0=0, \quad l=l_0=(a_0+1)/2, \quad k=k_0=(a_0^2-1)^{1/2}/2, \quad \beta=\beta_0=0 \quad (243)$$

at $t = t_0$.

Since the leading edge of the profile corresponds to $\bar{\zeta}=g+1$ and it must be at $x = a$, we have the condition:

$$a = x_0 + g + 1 + \frac{k^2}{g+1} \quad (244)$$

The trailing edge, $x = x_{TE}$, corresponds to $\bar{\zeta}=g-1$:

$$x_{TE} = x_0 + g - 1 + \frac{k^2}{g-1} \quad (245)$$

At $t = t_1$, we want

$$(x_{TE})_1 = 1 \quad (246)$$

and we also want to have the cusp of the profile at $x=1$:

$$k_1 = l_1 - g_1 \quad (247)$$

Finally, we want

$$\beta = \beta_1 \quad (248)$$

where β_1 is a prescribed value, at $t = t_1$ and constant for all $t \geq t_1$. Note that, at $t = t_1$, (245) can be replaced by a combination of (244), (245), (246) and (247):

$$a_1 - 1 = \frac{4l_1^2}{l_1 + g_1} \quad (249)$$

We should also prescribe g_1 , in addition to A , t_0 , t_1 , t_2 , t_3 , and β_1 ; the two parameters, g_1 and β_1 control the thickness of the wing. Then, (249), (247) and (244) yield l_1 , k_1 and x_{01} , respectively. We will also impose that

$$x_0 = E(t - t_0) \quad (250)$$

A simple fuselage-arrow-wing combination

between t_0 and t_1 . Therefore, $x_{01} = E(t_1 - t_0)$ and it is clear that E and t_1 cannot be prescribed independently. We choose to prescribe E .

Between t_0 and t_1 , g , β and l can be interpolated linearly, and x_0 is given by (250). Therefore, k and x_{TE} are obtained from (244) and (245). In particular,

$$k = [(a - x_0 - g - 1)(g + 1)]^{1/2} \quad (251)$$

Between t_0 and t_1 , one must also determine the point of intersection between wing and fuselage. The wing is defined by (239), (240) and (241); letting $X = x - x_0$, $\Gamma = g + l \cos \phi$, and noting that

$$(g + l \cos \phi)^2 + l^2 \sin^2 \phi = 2g\Gamma + l^2 - g^2 \quad (252)$$

the Cartesian coordinates of a cross-section of the wing are given by

$$X = \Gamma \left(1 + \frac{k^2}{2g\Gamma + l^2 - g^2} \right) \quad (253)$$

$$y = l \sin \phi \left(1 - \frac{k^2}{2g\Gamma + l^2 - g^2} \right) + \beta (x - x_{TE}) \left(\frac{x - a}{x_{TE} - a} \right)^2$$

From the first of (253)

$$\Gamma = \frac{-(l^2 - g^2 + k^2 - 2gX) + [(l^2 - g^2 + k^2 - 2gX)^2 + 8gX(l^2 - g^2)]^{1/2}}{4g} \quad (254)$$

$$\cos \phi = \frac{\Gamma - g}{l}, \quad \sin \phi = [1 - \left(\frac{\Gamma - g}{l}\right)^2]^{1/2} \quad (255)$$

and y can be obtained from the second of (253). The values of x and y which satisfy the latter and (242) simultaneously, which we will call x_{IN} , y_{IN} , define the wing-fuselage intersection.

Beyond t_1 , (250) is no longer valid. The trailing edge abscissa is defined instead:

A simple fuselage-arrow-wing combination

$$x_{TE} = 1 + (At_2 - 1) \frac{2}{\pi} \arcsin \frac{t - t_1}{t_2 - t_1} \quad (256)$$

and g :

$$g = \frac{1}{2} (a - x_{TE}) \sin \left(\frac{t + t_2 - 2t_1}{t_2 - t_1} \right) \quad (257)$$

Here, (244), (245), (247) and (248) are valid; therefore, (244) can be replaced by a relation similar to (249):

$$a - x_{TE} = \frac{4l^2}{1+g} \quad (258)$$

which yields l ; then, k is obtained from

$$k = 1 - g \quad (259)$$

and, from (245),

$$x_o = x_{TE} + 2k \quad (260)$$

A view from the top of a typical geometry is shown in Fig. 41. Some typical cross-sections of the airplane are shown in Fig. 42. They have been obtained with $A=0.5$, $B=0.05$, $E=0.3195$, $g=0.035$, $t_o=\pi$, $t_1=21.3287$, and $t_2=31.9930$. and $g_1=0.6$.

22. Mappings for the arrow-wing airplane

In the first section of the airplane ($t < t_0$), where the cross-section is an ellipse, only one mapping function is needed, and it is defined as for the elliptic cone.

In the second section, we need three successive mappings, one to open up the wing and two more to eliminate the corners at the wing-fuselage intersection. The first mapping is similar to the one used in the first section. The radius of curvature of the leading edge of the wing is

$$\rho = \frac{1[2(g+1)-(a-x_0)]^2}{(a-x_0)(g+1)}$$

The first hinge is defined by

$$h_{11} = [a(a-\rho)]^{1/2} \quad \delta_1 = 1/2$$

The second and third mapping are defined by

$$\begin{aligned} h_{21} &= x_{IN} - i y_{IN}, & \delta_2 &= \delta_{IN} \\ h_{31} &= x_{IN} + i y_{IN}, & \delta_3 &= \delta_{IN} \end{aligned}$$

The intersection points, $x_{IN} \pm i y_{IN}$, are determined using a trial-and-error routine. Eqs. (254) and (255) are used. In the code, the symbols:

$$D_1 = 1^2 - g^2, \quad d = D_1 + k^2 - 2gX, \quad D_2 = 4g\Gamma + d$$

$$\Delta = 2g\Gamma + D_1, \quad E_1 = 1 - k^2/\Delta,$$

$$E_2 = (x_{IN} - a)/(x_{TE} - a), \quad E_3 = 1 \sin\phi, \quad E_4 = \beta(x_{IN} - x_{TE})$$

are used for simplicity. Then the matching of

Mappings for the arrow-wing airplane

$$y_{IN}^{(1)} = E_1 E_3 + E_4 E_2^2$$

(which is the second of (253)) and

$$y_{IN}^{(2)} = (1 + x_{IN}^2) B^2$$

which is (242), defines y_{IN} and x_{IN} . The t -derivatives of x_{IN} and y_{IN} are obtained by differentiating the quantities above:

$$X_t = (x_{IN})_t - E, \quad D_{1t} = 2(l l_t - g g_t)$$

$$d_t = D_{1t} + (k_2)_t - 2(X g_t / g + X_t) g D_{2t} = 4g(\Gamma g_t / g + \Gamma_t) + d_t$$

$$\Gamma_t = [-\Gamma d_t + D_1(X g_t / g + X_t) + X D_{1t}] / D_2 - \Gamma g_t / g$$

$$(\cos \phi)_t = (g_t - \Gamma_t - l_t \cos \phi) / l, \quad (\sin \phi)_t = -\cos \phi (\cos \phi)_t / \sin \phi$$

$$\Delta_t = 2(\Gamma g_t / g + \Gamma_t) g + D_{1t}$$

$$E_{3t} = [-(k^2)_t + (1-E_1)\Delta_t] / \Delta$$

$$E_{2t} = [(x_{IN})_t - A - E_2(x_{TE})_t - A) / (x_{TE} - a)$$

$$E_{3t} = l_t \sin \phi + l (\sin \phi)_t$$

$$E_{4t} = \beta_t (x_{IN} - x_{TE}) + \beta [(x_{IN})_t - (x_{TE})_t]$$

$$(y_{IN})_t = E_1 E_{3t} + E_3 E_{1t} + (4E_{4t} E_2 + 2E_4 E_{2t}) E_2$$

Obviously, $(y_{IN})_t$ and $(x_{IN})_t$ must be obtained by a second trial-and-error procedure, the object of which is to match the value of $(y_{IN})_t$ above with the derivative of (242):

$$(y_{IN})_t = y_{IN} B_t / B + B^2 x_{IN} (x_{IN})_t / y_{IN}$$

Once all these values are found, the value of δ_2 and δ_3 is found as follows:

$$\Gamma_x = \Delta / D_2, \quad (\sin \phi)_x = \Gamma_x \cos \phi / E_3, \quad \Delta_x = 2g \Gamma_x$$

$$E_{1x} = (1-E_1)\Delta_x / \Delta, \quad E_{2x} = 1 / (x_{TE} - a)$$

Mappings for the arrow-wing airplane

$$\begin{aligned}
 E_{3x} &= l(\sin\phi)_x, \quad E_{4x} = \beta \\
 E_5 &= E_{3x}E_1 + E_3E_{1x}, \quad E_6 = E_{4x}E_2 + 2E_4E_{2x}, \quad T_3 = E_5 + E_2E_6 \\
 D_3 &= \arctan T_3, \quad D_4 = \arctan(-B^2x_{IN}/y_{IN}) \\
 \delta_2 = \delta_3 &= 1/[1 + (D_4 - D_3)/\pi] \quad (261)
 \end{aligned}$$

To compute the derivative of δ_2 and δ_3 with respect to t , we use the following expressions:

$$\begin{aligned}
 \Gamma_{xt} &= (\Delta_t - \Gamma_x D_{2t})/D_2 \\
 (\sin\phi)_{xt} &= [\Gamma_{xt}\cos\phi + \Gamma_x(\cos\phi)_t - (\sin\phi)_x E_{3t}]/E_3 \\
 E_{1xt} &= [(1-E_1)\Delta_{xt} - E_{1t}\Delta_x - E_{1x}\Delta_t]/\Delta, \quad E_{2xt} = -E_{2x}^2[(x_{TE})_t - A] \\
 E_{3xt} &= l_t(\sin\phi)_x + l(\sin\phi)_{xt}, \quad E_{4xt} = \beta_t \\
 E_{5t} &= E_{3xt}E_1 + E_{3x}E_{1t} + E_{3t}E_{1x} + E_3E_{1xt} \\
 E_{6t} &= E_{4xt}E_2 + E_{4x}E_{2t} + 2(E_{4t}E_{2x} + E_4E_{2xt}) \\
 D_{3t} &= (E_{5t} + E_{2t}E_6 + E_2E_{6t})/(1 + T_3^2) \\
 D_{4t} &= [(x_{IN}(y_{IN})_t - y_{IN}(x_{IN})_t)B^2 - 2BB_t x_{IN}y_{IN}]/(B^4x_{IN}^2 + y_{IN}^2) \\
 \delta_{2t} = \delta_{3t} &= -\delta_2^2(D_{4t} - D_{3t})/\pi \quad (262)
 \end{aligned}$$

In the vicinity of t_1 , δ_1 and δ_3 become larger than 2 and then tend to 2 as t tends to t_1 ; in addition, their t -derivatives tend to infinity. Therefore, it is convenient to replace (261) and (262) by the following expressions:

$$\delta_i = 2 + \tau(B_2 + B_3\tau), \quad \delta_{it} = B_2 + 2B_3\tau \quad (263)$$

The symbols in (263) are defined as follows. Let δ_{i0} and δ_{ito} be the values of δ_i and δ_{it} at a cross-section where δ_i becomes greater than 1.85; let t^* be the value of t at such a cross-section and

Mappings for the arrow-wing airplane

$$\alpha = t^* - t_1, \quad \tau = t - t_1, \quad B_3 = (2 + \delta_{ito} \alpha - \delta_{io}) / \alpha^2, \quad B_2 = \delta_{ito} - 2B_3 \alpha \quad (264)$$

The above fit merges smoothly with (261) at $t = t^*$ and goes smoothly to $\delta_i = 2$ at $t = t_1$.

The other two points of interest are the lower and upper intersection of the fuselage with the $x=0$ line, viz.

$$h_{41} = -ib, \quad h_{51} = ib$$

23. Additional formulas used beyond t_1

Beyond t_1 , the following formulas are used to get the first and second derivatives of the geometric parameters:

$$\Delta_1 = (t - t_1) / (t_2 - t_1), \quad \Delta_{1t} = 1 / (t_2 - t_1) \quad (265)$$

$$d = \arcsin \Delta_1, \quad d_t = \Delta_{1t} / (1 - \Delta_1^2)^{1/2} \quad (266)$$

$$\Delta_2 = 2(At_2 - 1) / \pi \quad (267)$$

$$\Delta_3 = \pi \Delta_{1t} (t + t_2 - 2t_1) / 2, \quad \Delta_{3t} = \pi \Delta_{1t} / 2 \quad (268)$$

$$x_{TE} = 1 + d\Delta_2, \quad (x_{TE})_t = \Delta_2 d_t \quad (269)$$

$$d_1 = (a - x_{TE}) / 2, \quad d_{1t} = [A - (x_{TE})_t] / 2 \quad (270)$$

$$g = \Gamma d_1 \sin \Delta_3, \quad g_t = d_{1t} g / d_1 + \Gamma d_1 \Delta_{3t} \cos \Delta_3 \quad (271)$$

$$\Delta_4 = (d_1^2 + 8d_1 g)^{1/2}, \quad \Delta_{4t} = [d_1 d_{1t} + 4(g d_{1t} + d_1 g_t)] / \Delta_4 \quad (272)$$

$$l = (d_1 + \Delta_4) / 4, \quad l_t = (d_{1t} + \Delta_{4t}) / 4 \quad (273)$$

$$k = l - g, \quad k_t = l_t - g_t \quad (274)$$

$$x_o = x_{TE} + 2k, \quad x_{ot} = (x_{TE})_t + 2k_t \quad (275)$$

$$\lambda = (1 + g)k, \quad \lambda_t = 2(l l_t - g g_t) \quad (276)$$

For the second and third mappings,

Additional formulas used beyond t_1

$$h_{21} = h_{31} = x_{TE}, \quad \delta_i = 1/[1-(\arctan \beta_1)/\pi], \quad d_{it} = 0 \quad (277)$$

and two more mappings are used, with

$$h_{41} = h_{51} = 1, \quad \delta_i = 2 \quad (278)$$

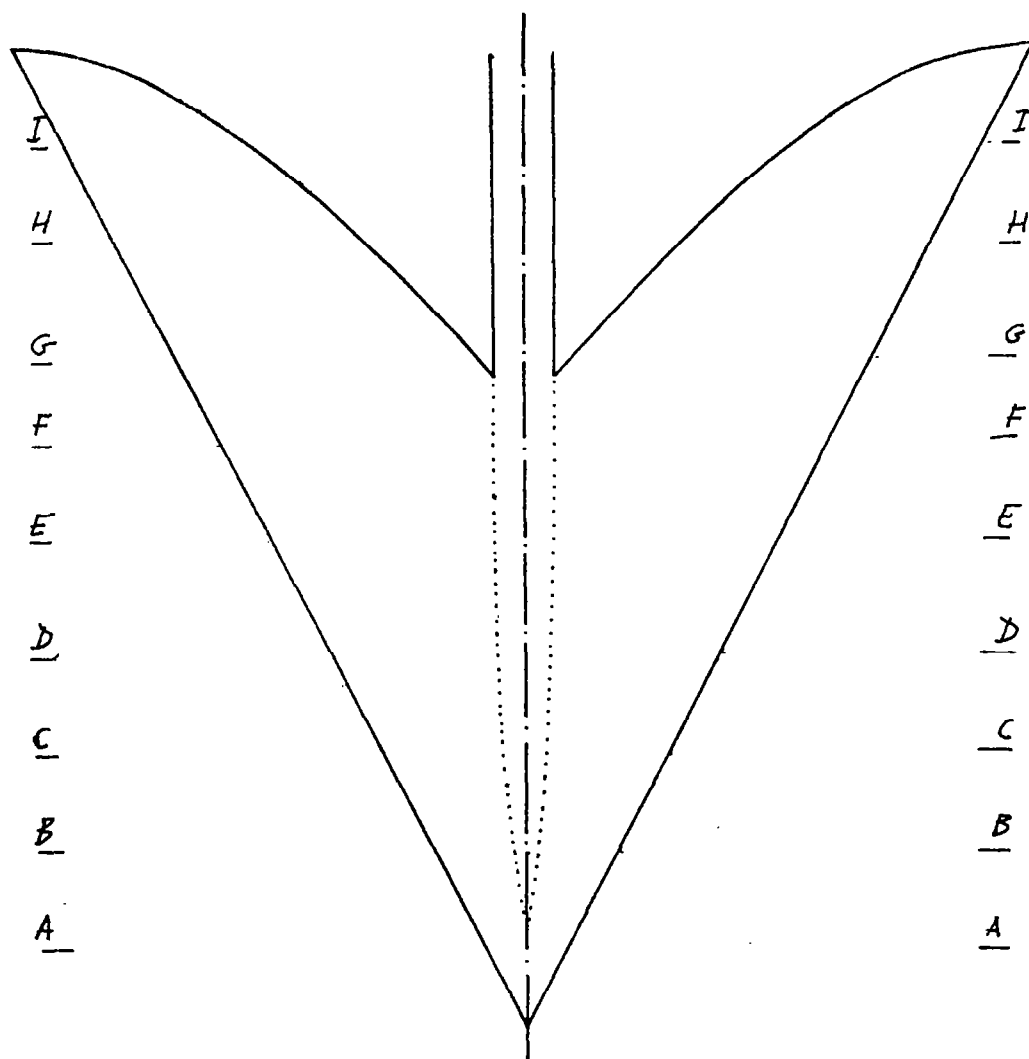


Fig. 41

Some results on fuselage-arrow wing combinations

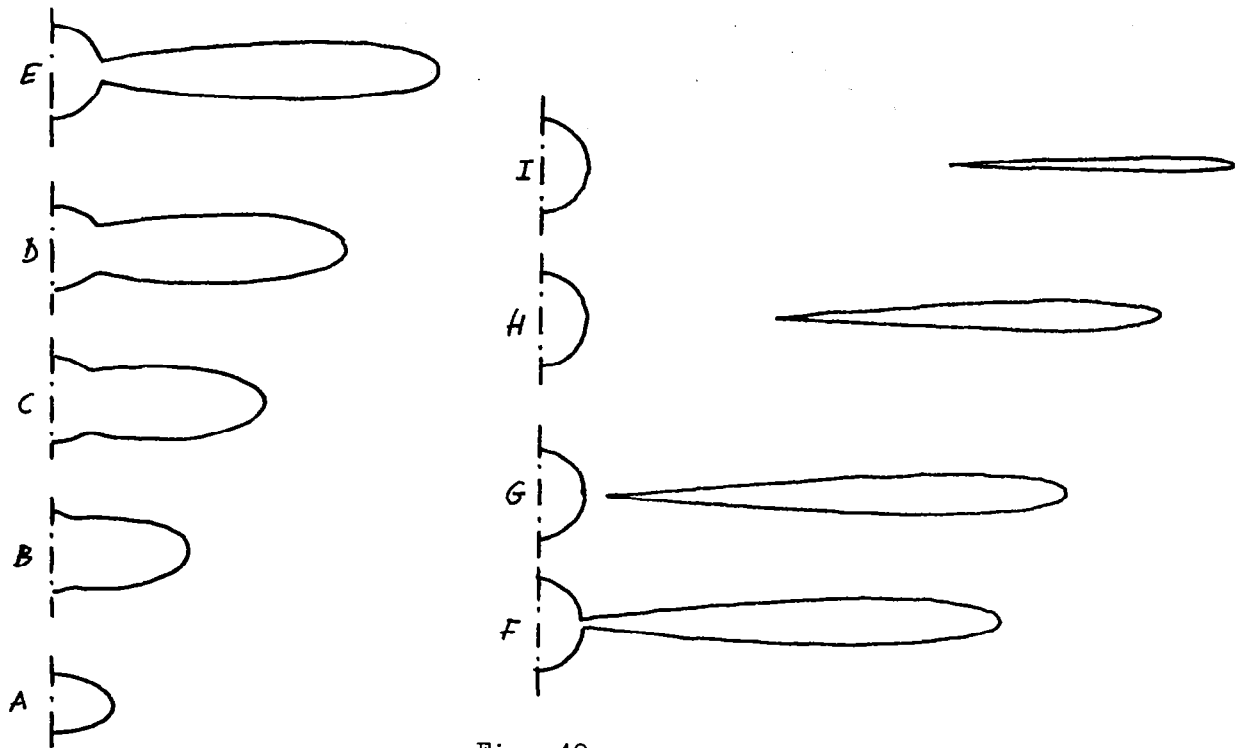


Fig. 42

24. Some results on fuselage-arrow-wing combinations

We will report here the results of seven runs made with the geometry above. Runs 50, 51, 61, 62, 63 and 64 were made with the following values of geometrical parameters: $A=0.5$, $B=0.05$, $E=0.3195$, $g=0.035$, $t_0=\pi$, $t_1=21.3287$, and $t_2=31.9930$. Run 52 was made using the following geometrical parameters: $A=0.25$, $B=0.05$, $E=0.1831$, $g=0.06$, $t_0=2\pi$, $t_1=27.8193$, and $t_2=38.3906$. The angle of attack is equal to zero in Runs 50, 51 and 52, equal to 3 degrees in Runs 61, 63 and 64, and to 6 degrees in Run 62. The Mach number equals 2.36 in Runs 50 and 64, 2.96 in Run 63, and 4.63 in Runs 51, 52, 61, 62.

In the following Figs. 43 through 62, computed values of C_p are compared with measurements made at NASA (Ref. 16). The values of X quoted in the figures are, in the notation of the present Report, values of t/t_2 . Similarly, the values of Y are values of x/t_2 .

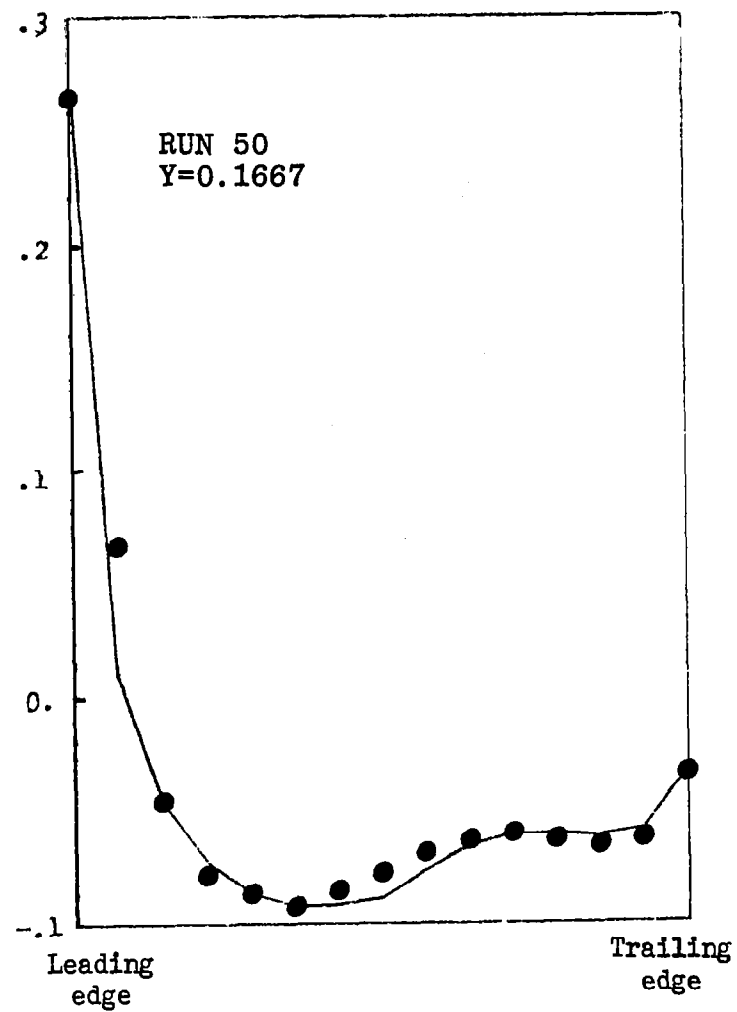
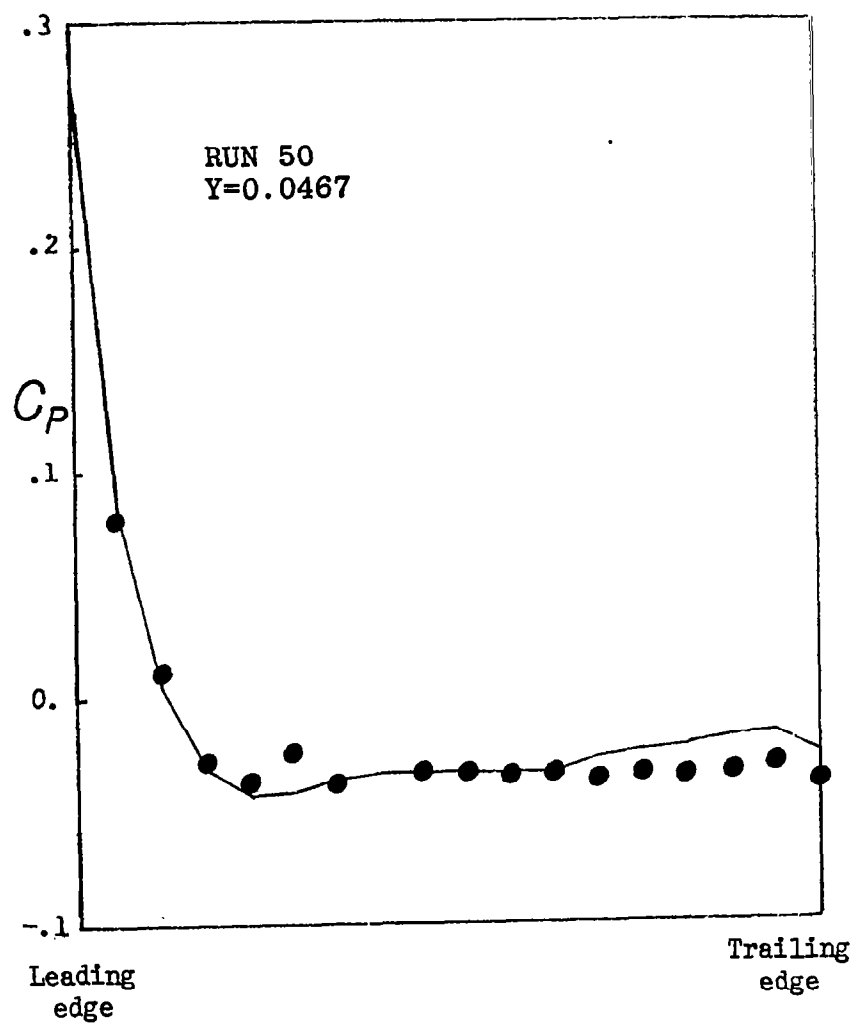


Fig. 43

Some results on fuselage-arrow wing combinations

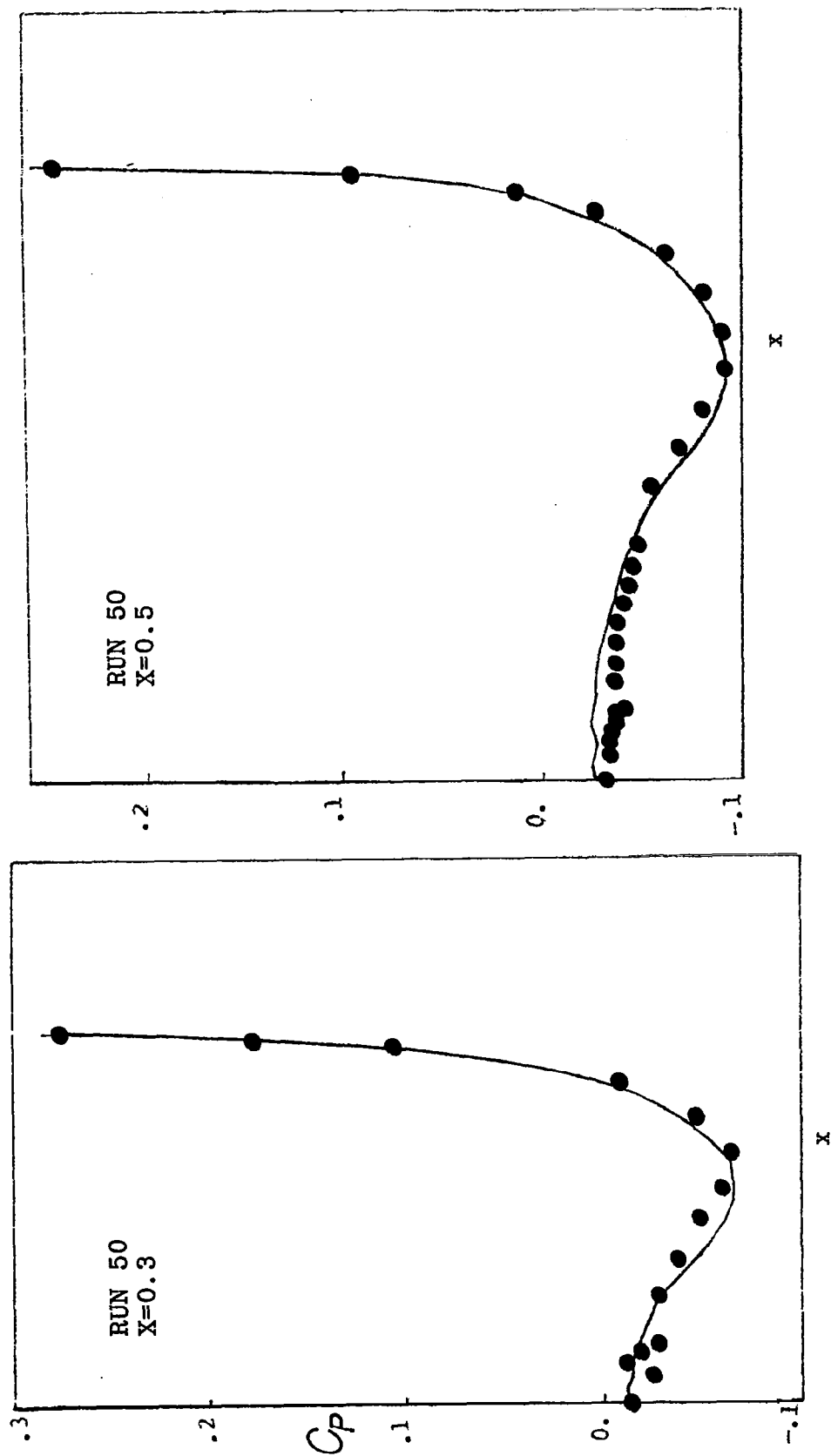


Fig. 44

Some results on fuselage-arrow wing combinations

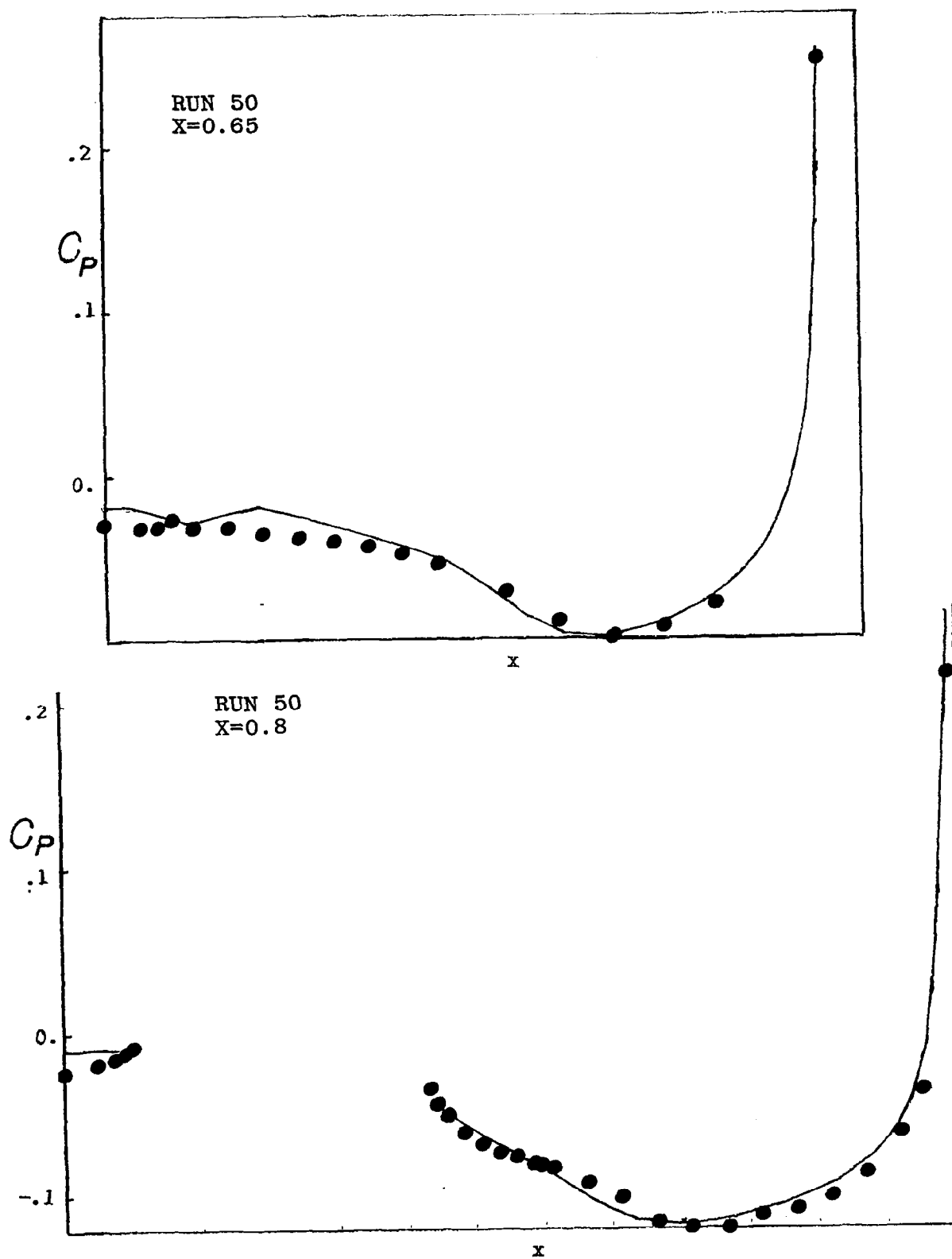


Fig. 45

Some results on fuselage-arrow wing combinations

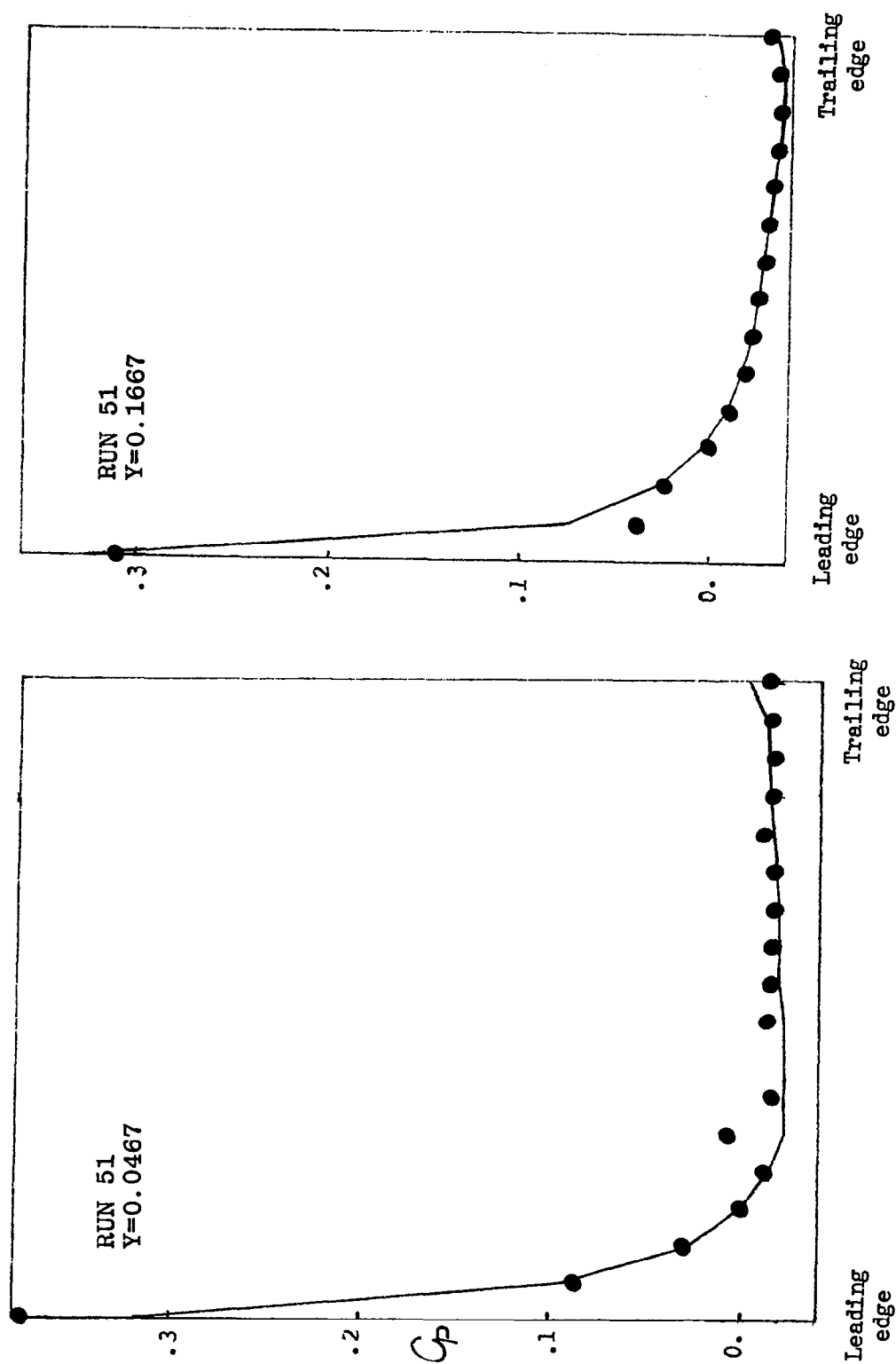


Fig. 46

Some results on fuselage-arrow wing combinations

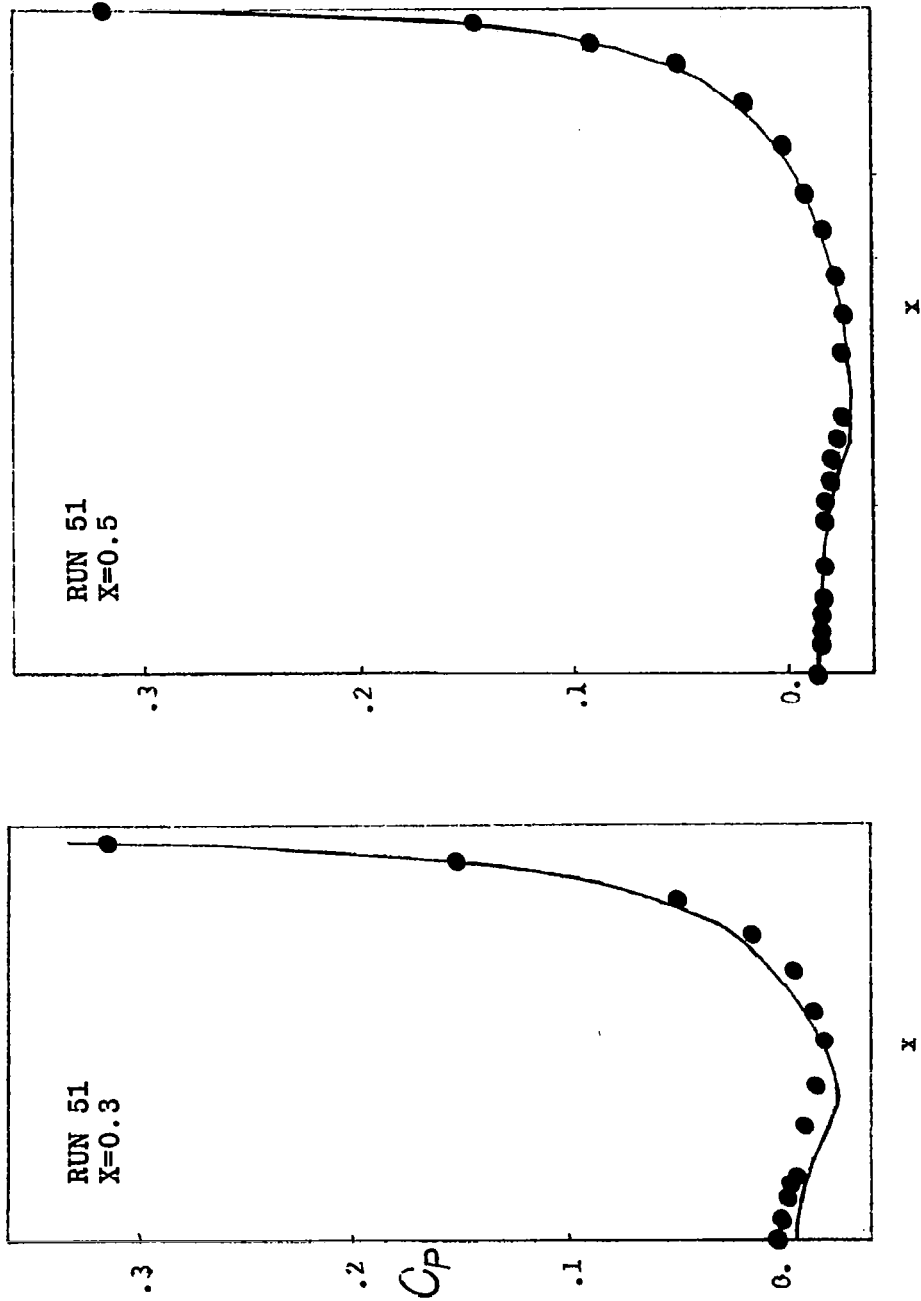


Fig. 47

Some results on fuselage-arrow wing combinations

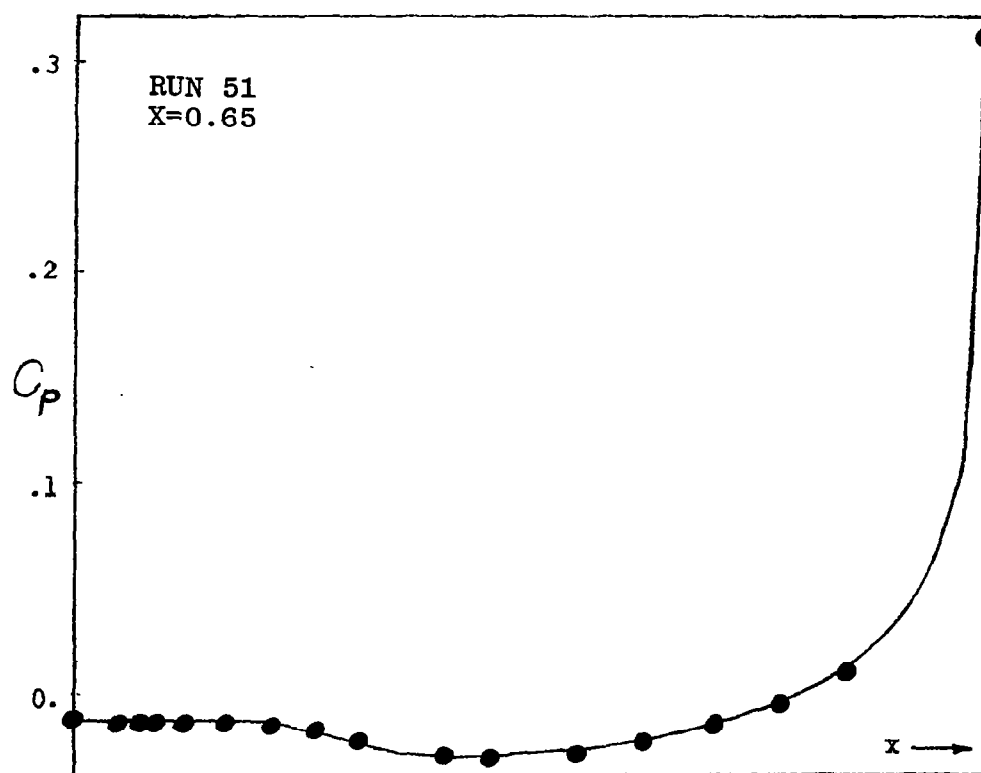
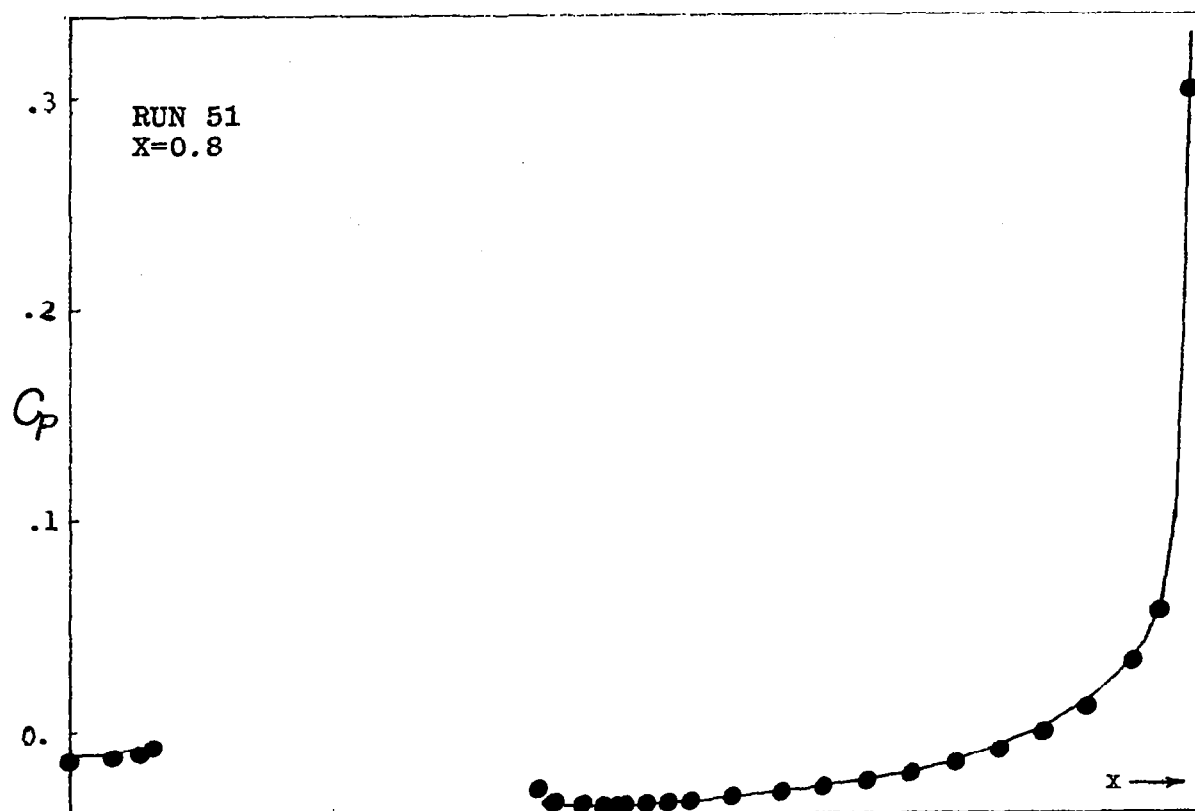


Fig. 48

Some results on fuselage-arrow wing combinations

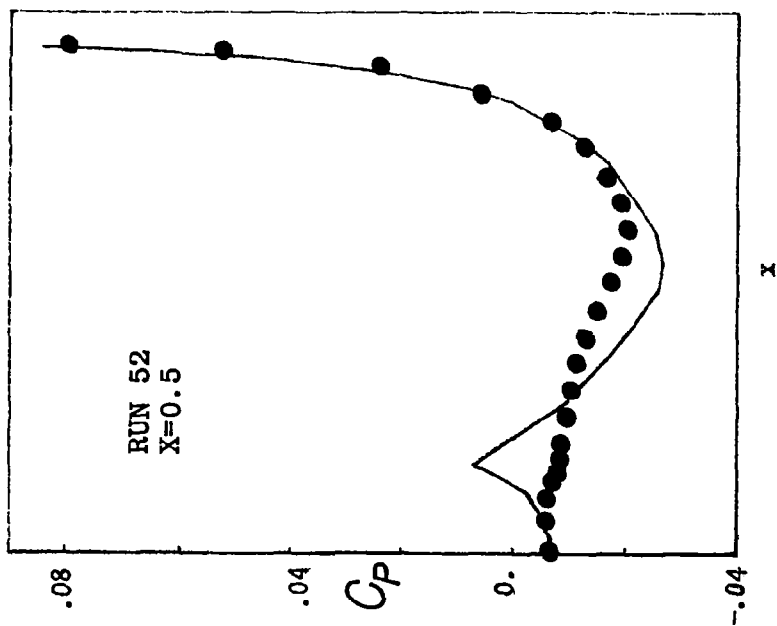
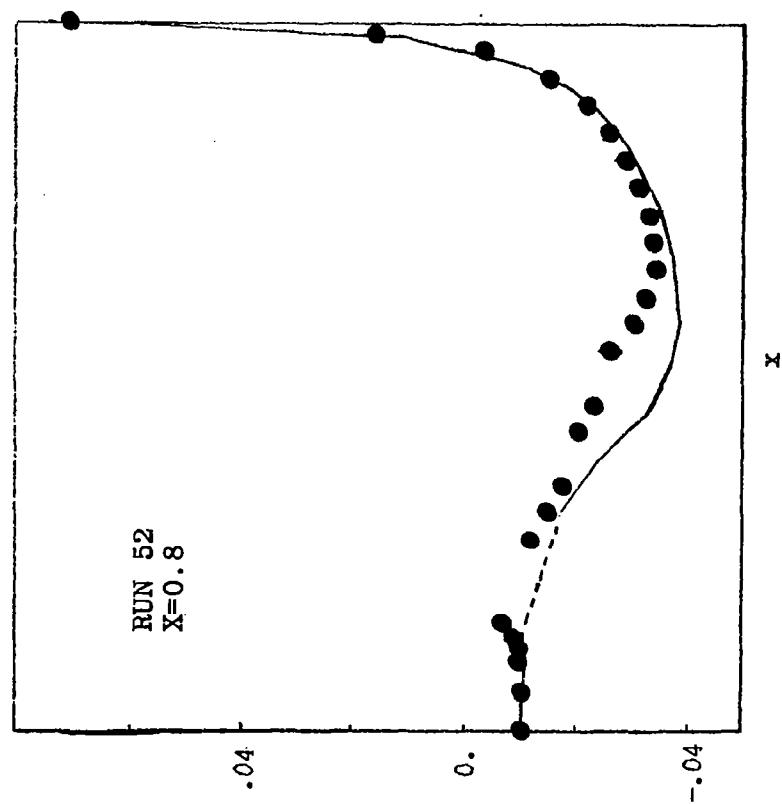
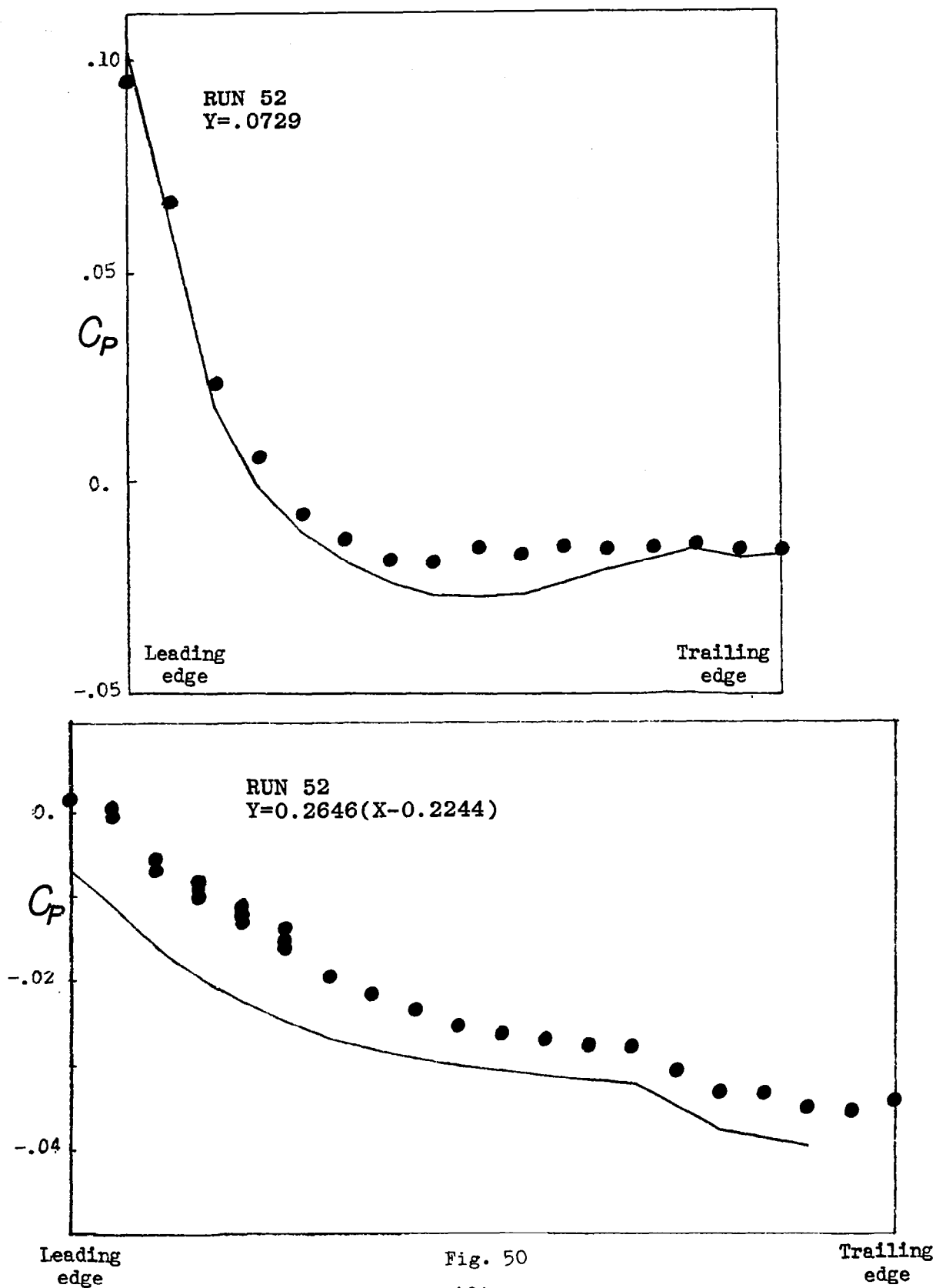


Fig. 49

Some results on fuselage-arrow wing combinations



Some results on fuselage-arrow wing combinations

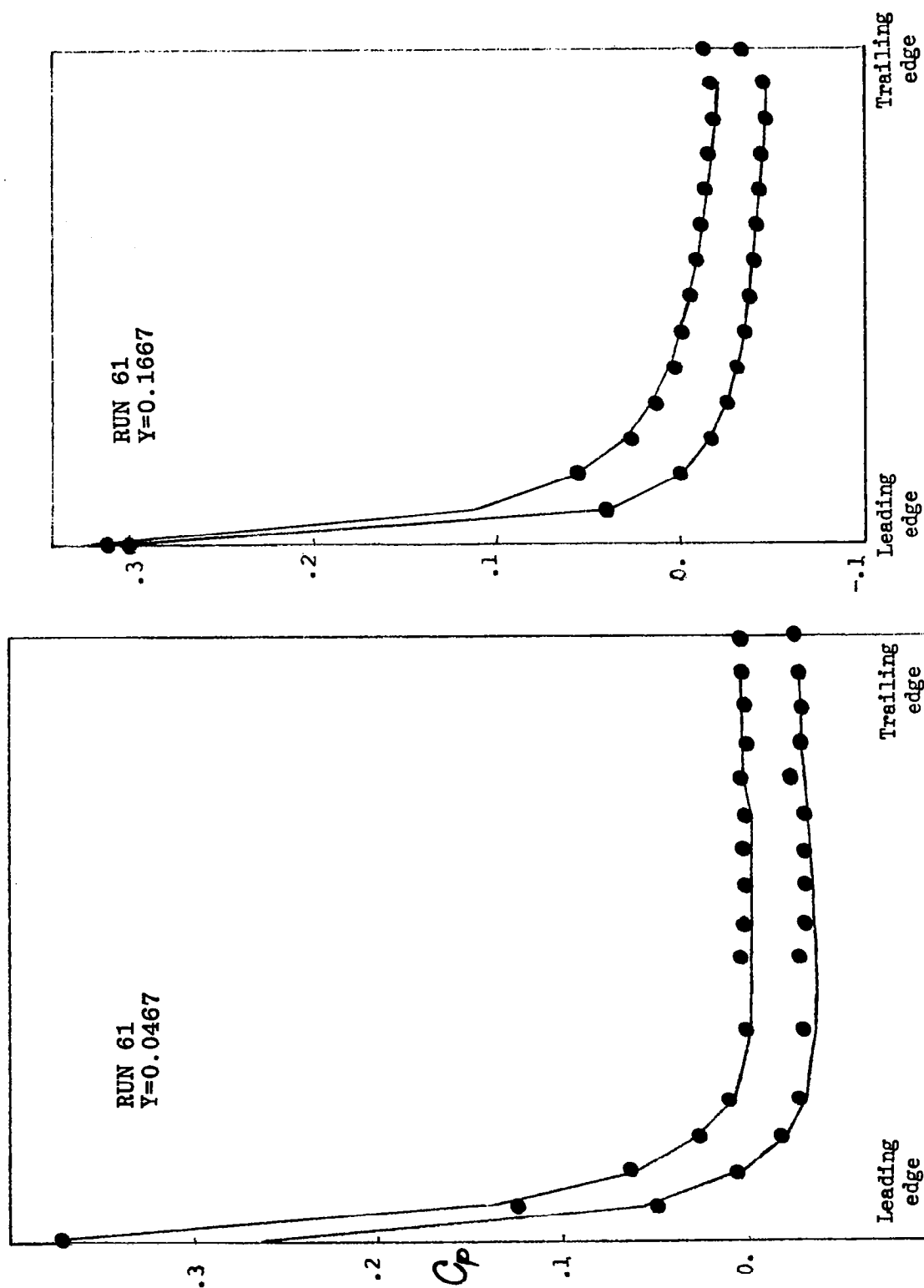


Fig. 51

Some results on fuselage-arrow wing combinations

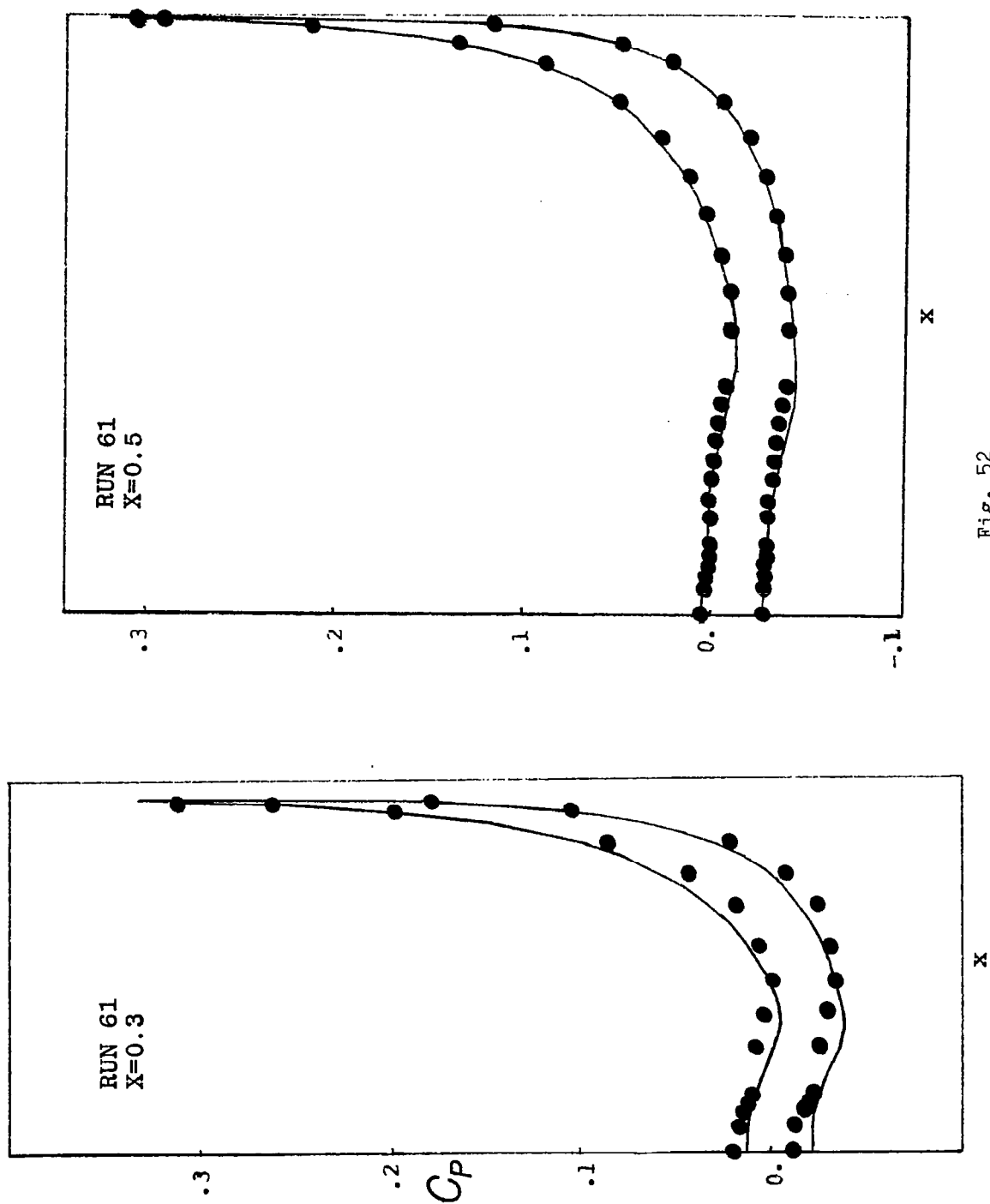


Fig. 52

Some results on fuselage-arrow wing combinations

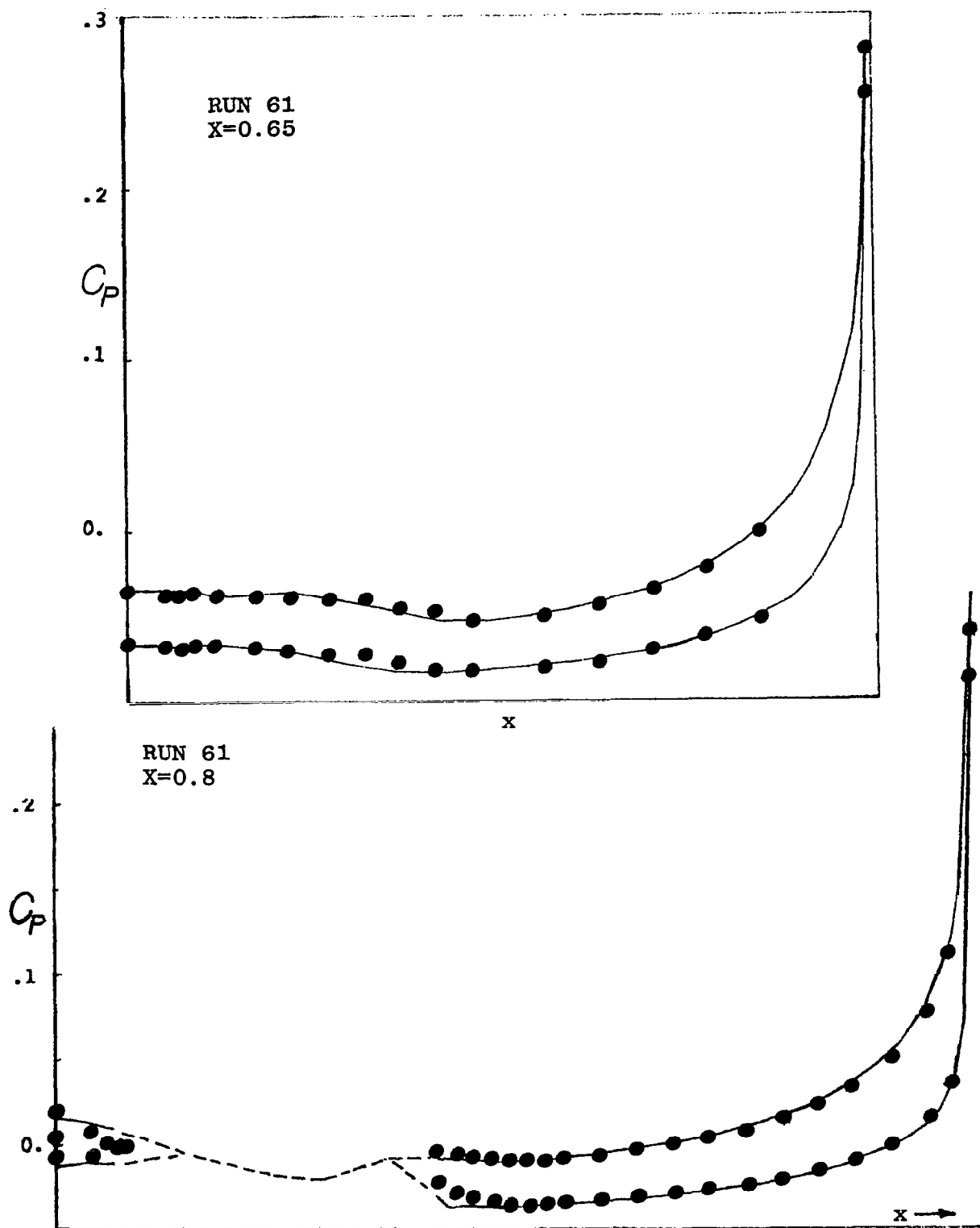


Fig. 53

Some results on fuselage-arrow wing combinations

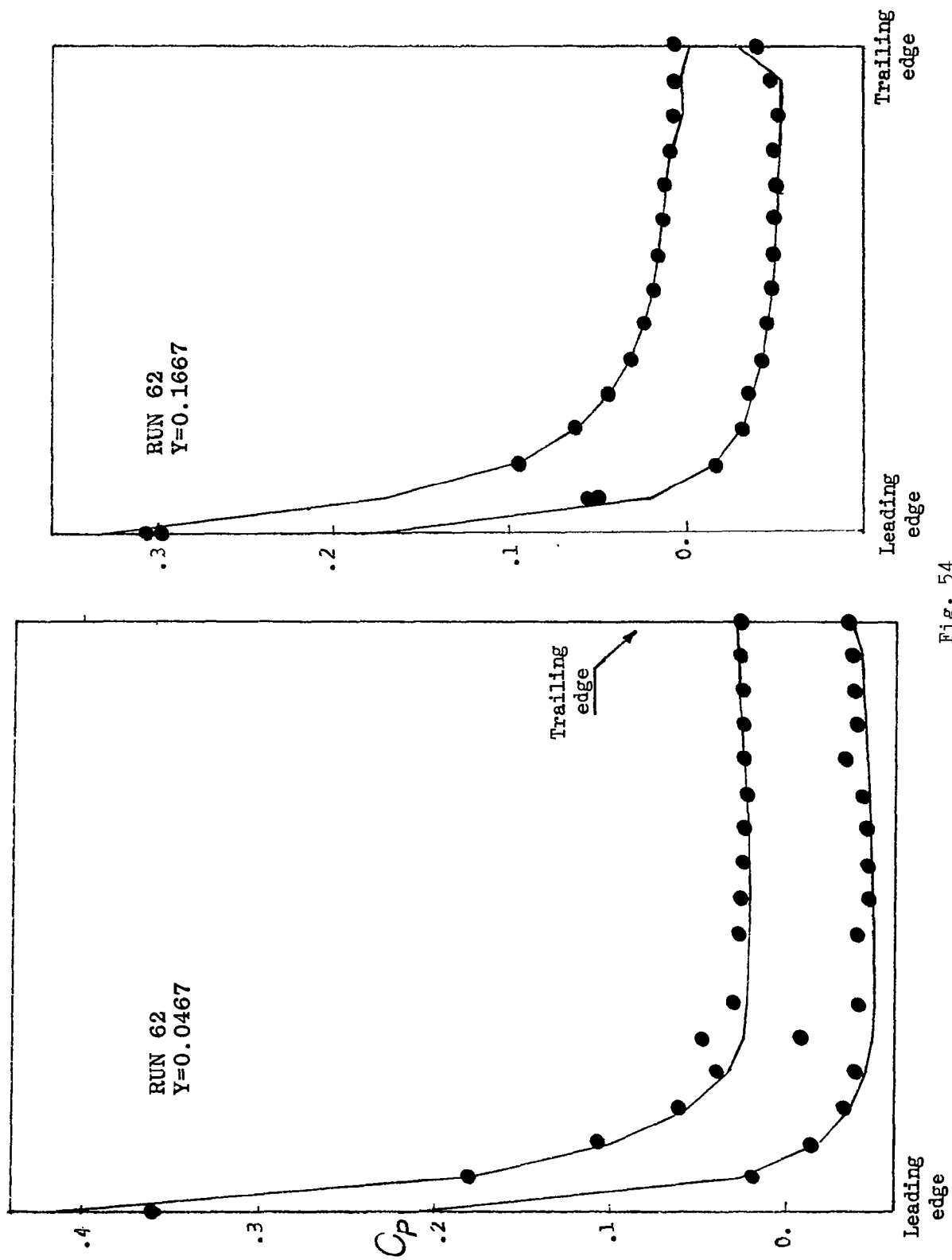


Fig. 54

Some results on fuselage-arrow wing combinations

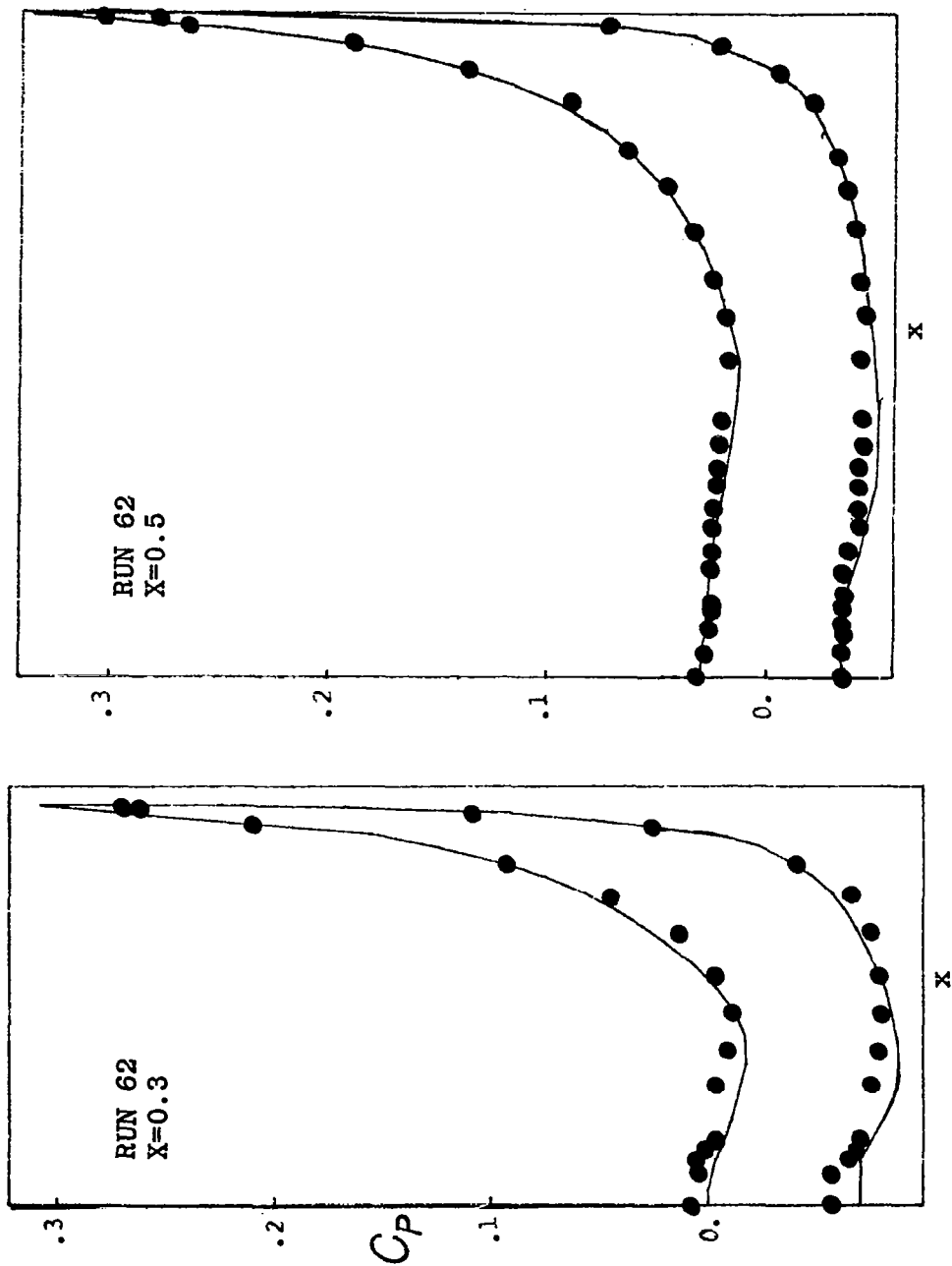


Fig. 55

Some results on fuselage-arrow wing combinations

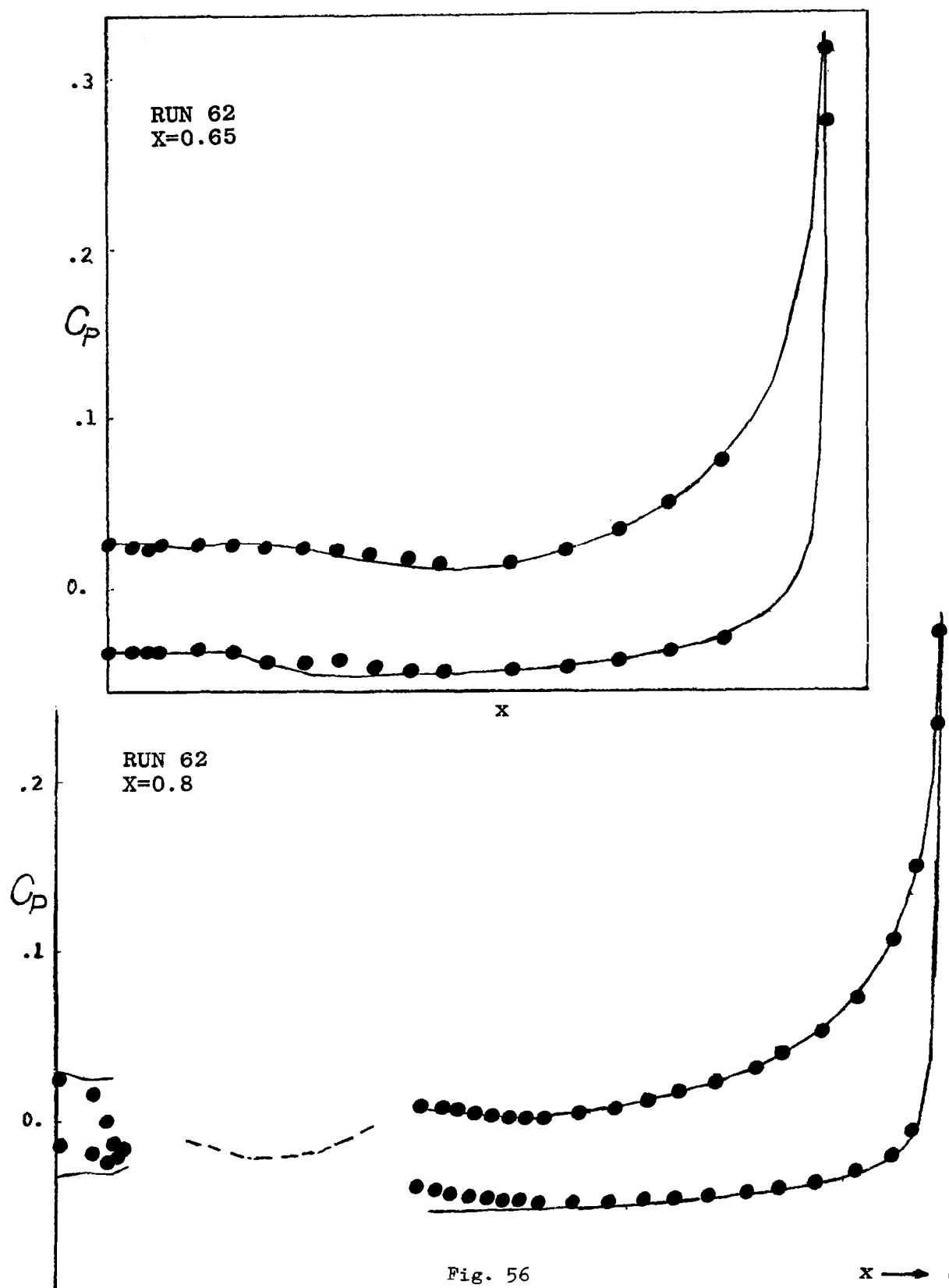


Fig. 56

Some results on fuselage-arrow wing combinations

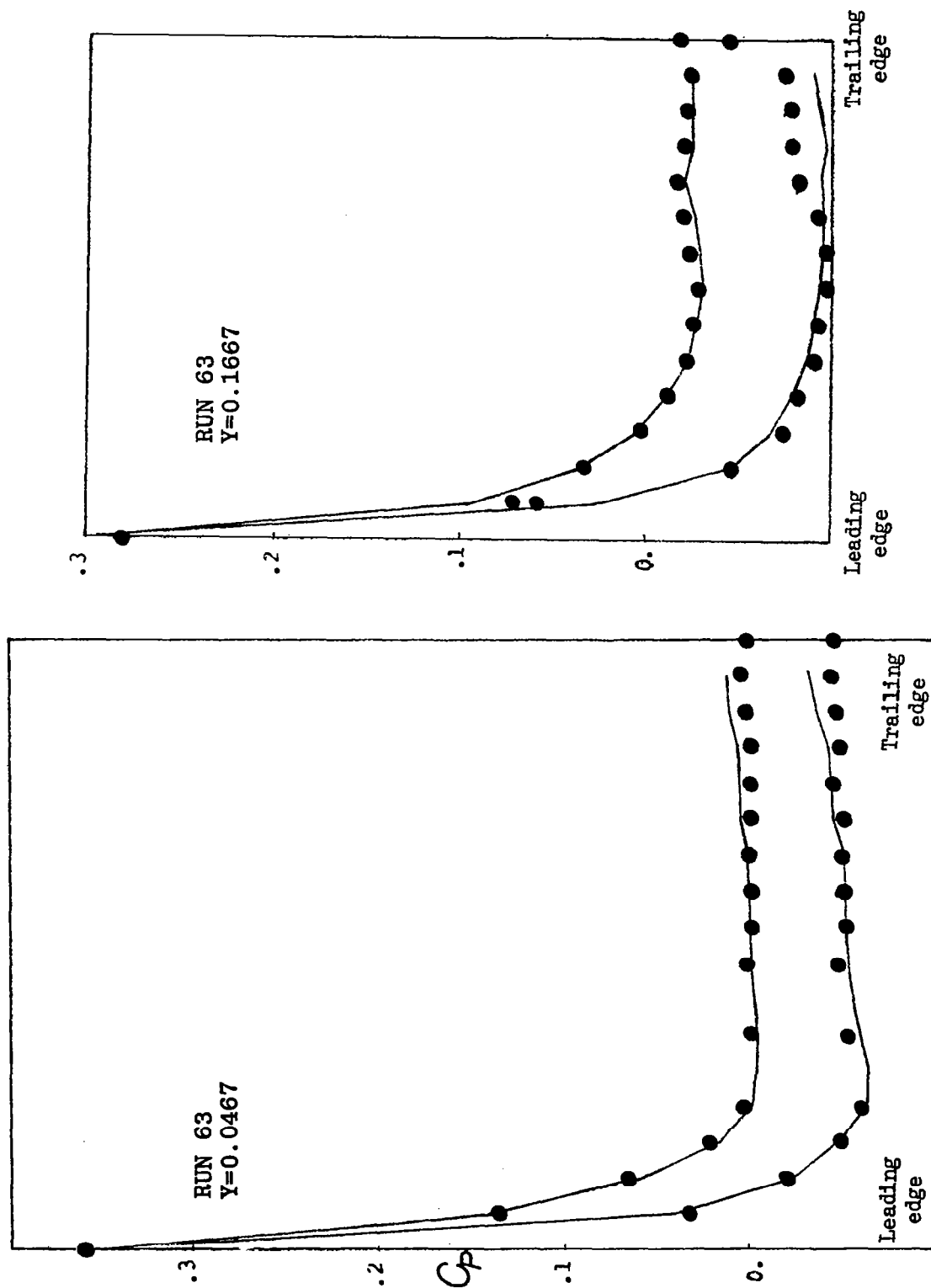


Fig. 57

Some results on fuselage-arrow wing combinations

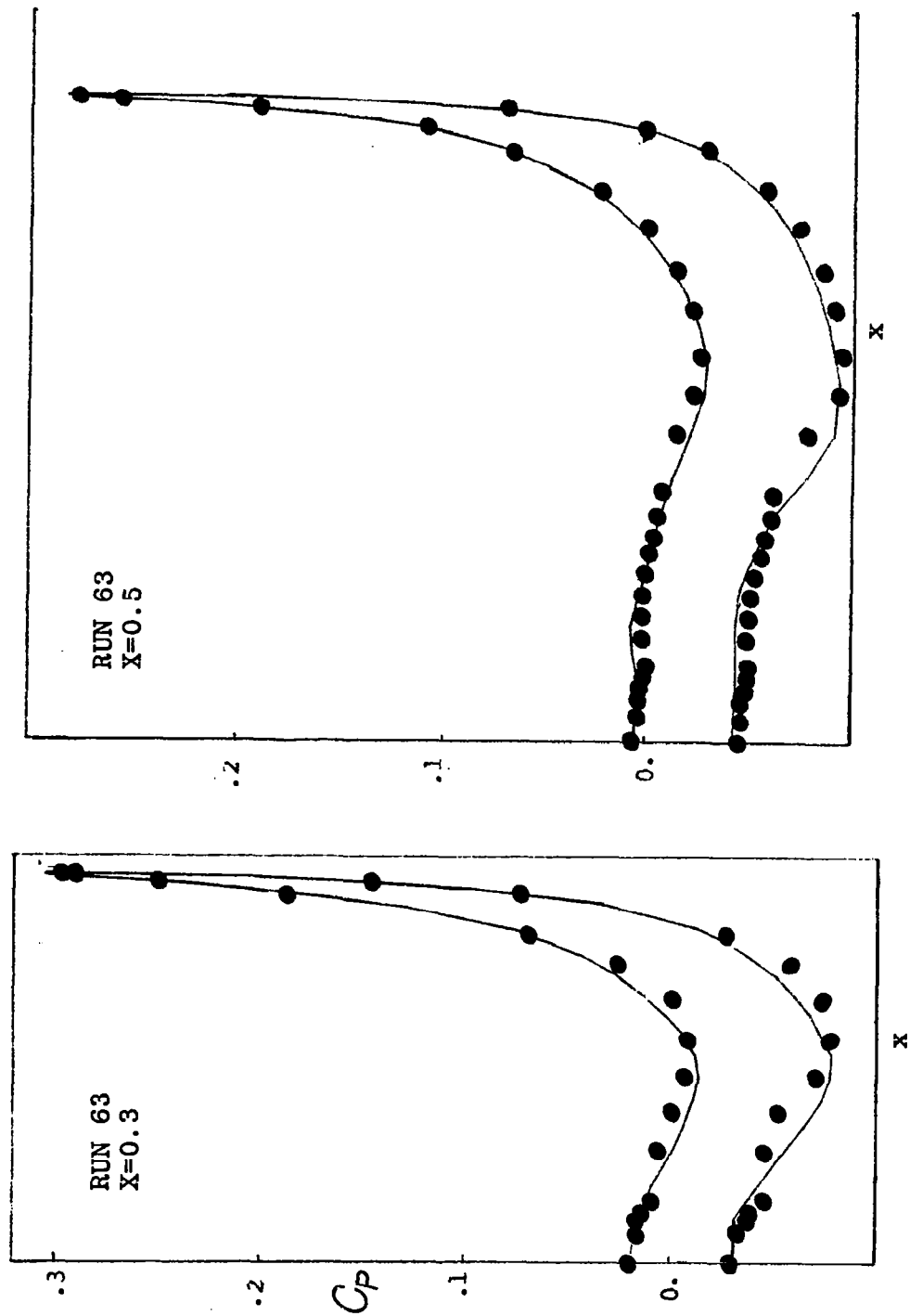


Fig. 58

Some results on fuselage-arrow wing combinations

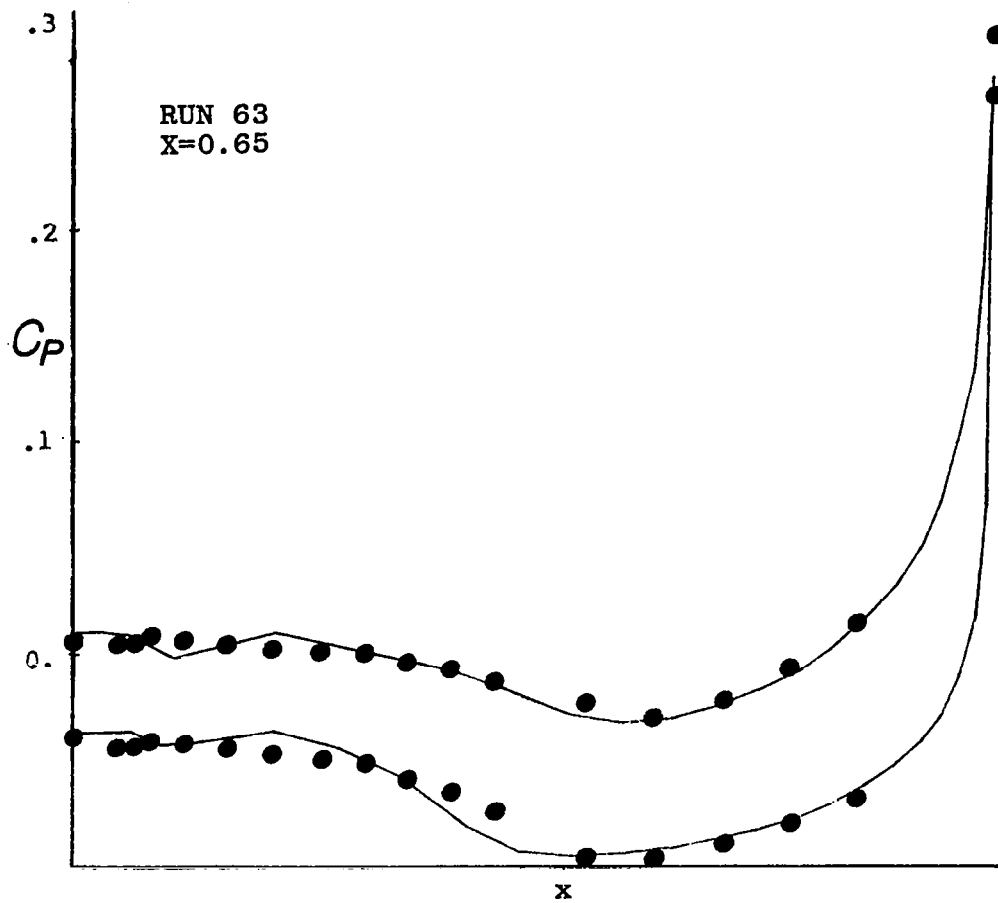


Fig. 59

Some results on fuselage-arrow wing combinations

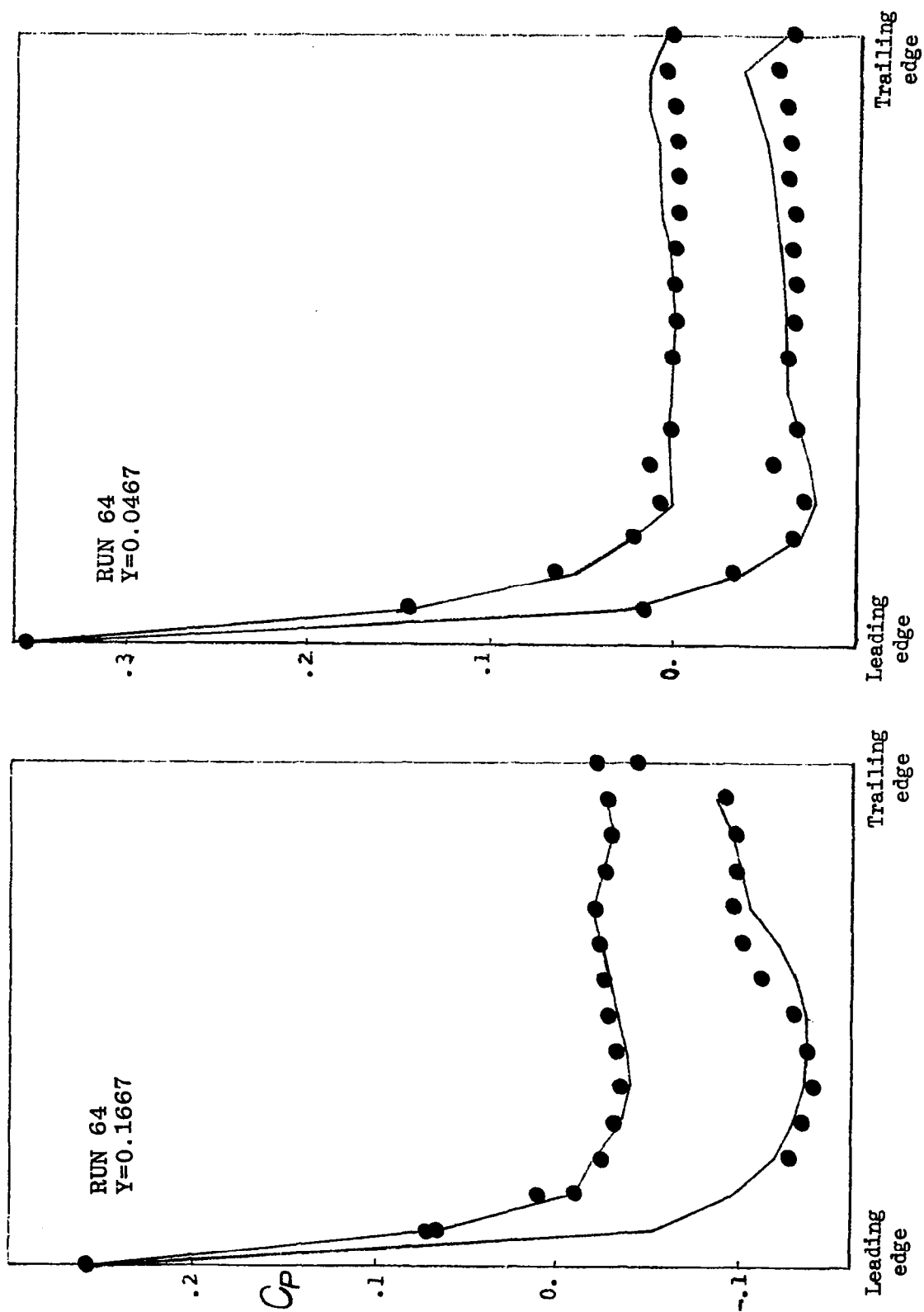


Fig. 60

Some results on fuselage-arrow wing combinations

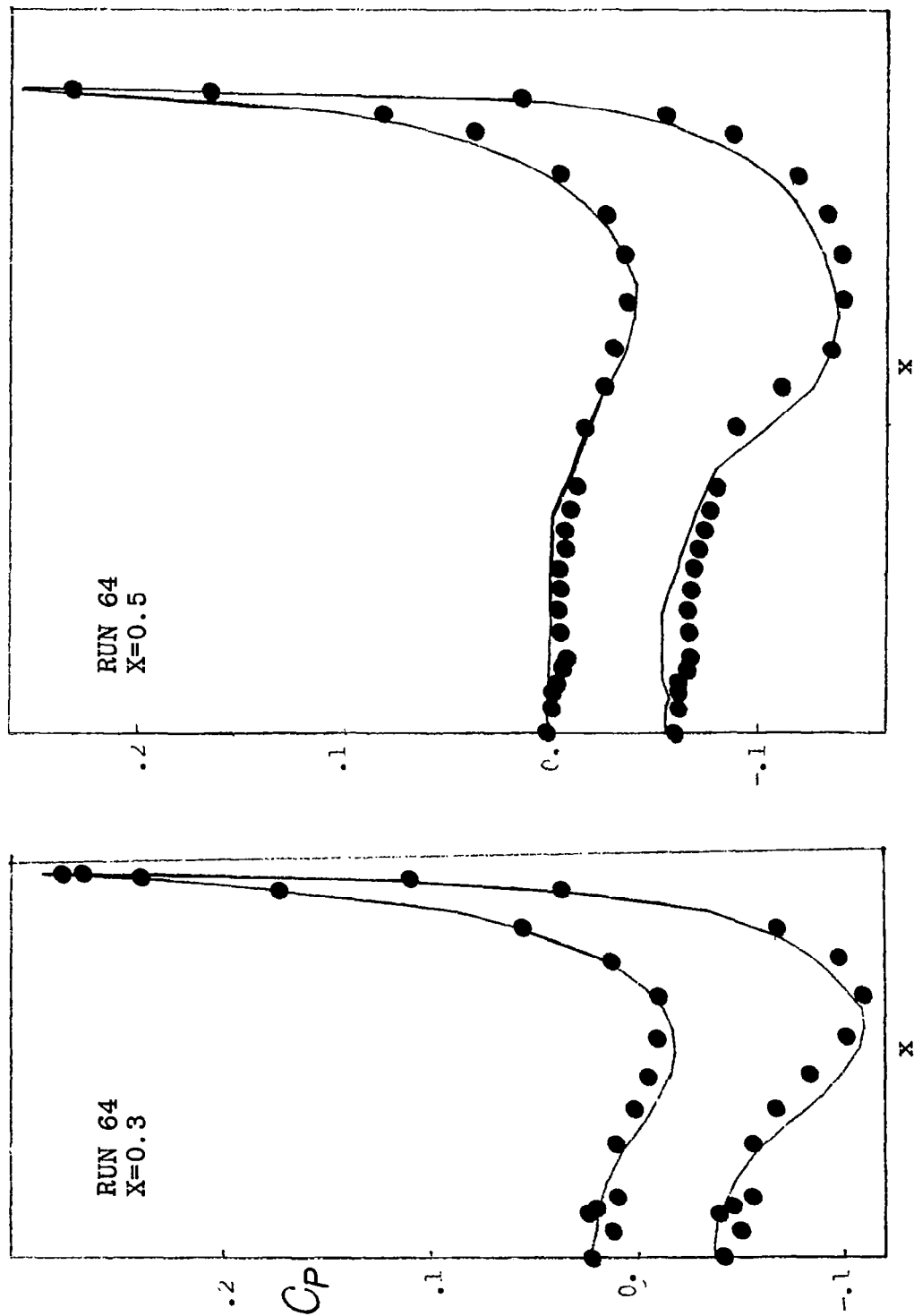


Fig. 61

Some results on fuselage-arrow wing combinations

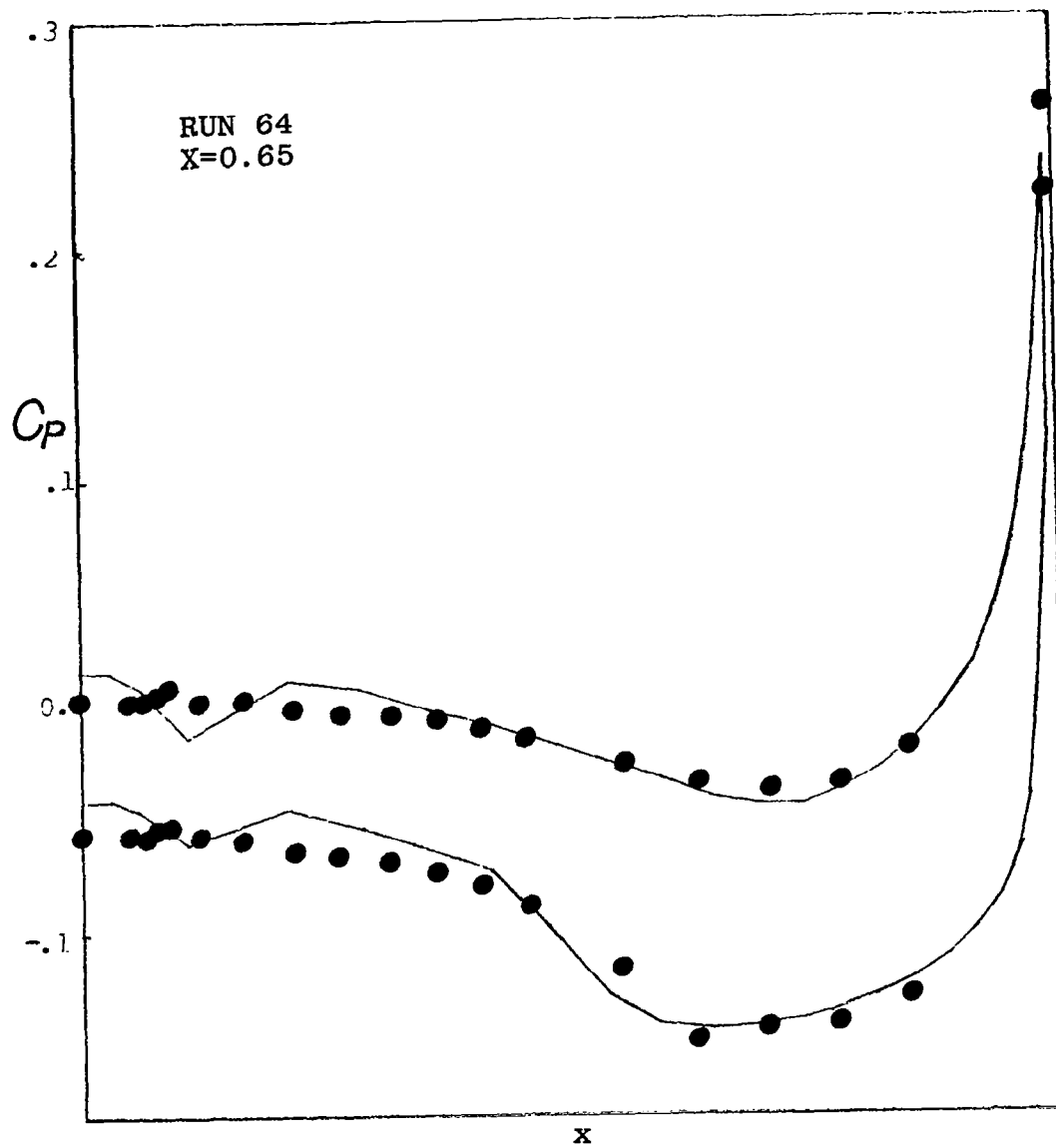


Fig. 62

REFERENCES

1. Moretti, G., Calculation of the three-dimensional, supersonic, inviscid, steady flow past an arrow-winged airframe, Part I, POLY M/AE Report No. 76-8, 1976
2. de Neef, T., Treatment of boundaries in unsteady inviscid flow computations, Delft Univ. of Technology Report No. LR-262, 1978
3. Moretti, G., The λ -scheme, Comp. and Fluids, 7, 191, 1979
4. MacCormack, R.W., The effect of viscosity in hypervelocity impact cratering, AIAA 7th Aerospace Science Meeting, New York, Paper No. 69-354, 1969
5. Moretti, G. and Pandolfi, M., Entropy layers, Comp. and Fluids, 1, 19, 1973
6. Moretti, G. and Pandolfi, M., Analysis of the inviscid flow about a yawed cone. Preliminary studies, PIBAL Report No. 72-18, 1972
7. Moretti, G., Conformal mappings for computations of steady, three-dimensional, supersonic flows, in "Numerical/Laboratory computer methods in fluid mechanics", A.A.Pouring, V.I.Shah, eds., ASME, N.Y, 1976, pp. 13-28
8. Jones, D.J., Tables of inviscid supersonic flow about circular cones at incidence, $\gamma=1.4$, AGARDograph 137, 1969
9. Moretti, G., Inviscid flow field past a pointed cone at an angle of attack, General Applied Science Labs., Report No. 577, 1965
10. NACA Ames Research Staff, Equations, tables and charts for compressible flow, Report 1135, 1953.
11. Siclari, M., Investigation of cross-flow shocks on Delta-wings in supersonic flows, AIAA Paper 79-0345, 1979.
12. Marconi, F. and Siclari, M., A study of the inviscid flow

about conical cambered Delta-wings, AIAA Paper 78-58, 1978.

13. Grossman, B., Numerical procedures for the computation of irrotational conical flows, AIAA J. 17, 1979, 828.

14. Butler, D.S., The numerical solution of hyperbolic systems of partial differential equations in three independent variables, Proc. Roy. Soc. 255, 232, 1960.

15. Squire, L.C., Measured pressure distribution and shock shapes on a 'Butler' wing, Cambridge Univ. Eng. Dept. Report Aero/TR9, 1979.

16. Townsend, J., Pressure data for four analytically defined arrow wings in supersonic flow, NASA TM 81835, 1980.

17. Pandolfi, M., Numerical analysis of the supersonic flow about elliptical cones, Istituto di Macchine e motori per aeromobili, Politecnico di Torino, Report N. 157, 1974.

Acknowledgment.

I am pleased to extend my warmest thanks to Miss Catherine Fahy who has assisted me during the entire course of this project. Without her patient and competent cooperation, I would not have been able to perform such a complex and exacting work.

1. Report No. NASA CR-3573		2. Government Accession No.		3. Recipient's Catalog No.	
4. Title and Subtitle CALCULATION OF THREE-DIMENSIONAL, INVISCID SUPERSONIC, STEADY FLOWS				5. Report Date June 1982	
				6. Performing Organization Code	
7. Author(s) Gino Moretti				8. Performing Organization Report No.	
				10. Work Unit No.	
9. Performing Organization Name and Address Polytechnic Institute of New York Farmingdale, NY 11735				11. Contract or Grant No. NSG-1248	
				13. Type of Report and Period Covered Contractor Report	
12. Sponsoring Agency Name and Address National Aeronautics and Space Administration Washington, DC 20546				14. Sponsoring Agency Code	
15. Supplementary Notes Langley Technical Monitor: Manuel D. Salas Topical Report					
16. Abstract A numerical technique is described for the calculation of three-dimensional, inviscid, supersonic, steady flows over wing-body configurations. A high degree of accuracy without increasing the number of computational nodes is obtained by means of a powerful conformal mapping technique. Results are presented for some simple body configurations and for a more complex arrow-wing airframe. The numerical results show excellent agreement with experimental measurements.					
17. Key Words (Suggested by Author(s)) Supersonic Flows Computational Aerodynamics Conformal Mappings Wing-Fuselage Conical Flows			18. Distribution Statement Unclassified-Unlimited Subject Category 02		
19. Security Classif. (of this report) Unclassified	20. Security Classif. (of this page) Unclassified	21. No. of Pages 124	22. Price* A06		